ESCOLA SUPERIOR DE TECNOLOGIA DA SAÚDE DE COIMBRA

Polytechnique Institute of Coimbra

Coimbra Health School

Assessment of the Performance of an Enhanced Planar Processing Algorithm for Whole-body Bone Scintigraphy

A Phantom Study

Sara Joana Cortesão Serém

Master's Degree in Nuclear Sciences Applied to Health

2014

ESCOLA SUPERIOR DE TECNOLOGIA DA SAÚDE DE COIMBRA

Polytechnique Institute of Coimbra

Coimbra Health School

Master's Degree in Nuclear Sciences Applied to Health

Dissertation

Assessment of the Performance of an Enhanced Planar Processing Algorithm for Whole-body Bone Scintigraphy

A Phantom Study

Sara Joana Cortesão Serém

Advisor:

António Manuel Rodrigues Carvalho dos Santos, Ph.D.

Co-advisor:

Joana Margarida Rodrigues dos Santos, Ph.D.

Coimbra, October, 2014

Learn from yesterday, live for today, hope for tomorrow.

The important thing is not to stop questioning.

Albert Einstein

Acknowledgments

I would like to express my gratitude to all the people involved in the work described in this thesis.

First and foremost, I thank the principal supervisor, Wim van den Broek, for accepting the internship opportunity in the Netherlands with no regrets. I really appreciated his vast knowledge, understanding and constant support. It was a great experience that I will never forget!

I would like to thank the other supervisors, Eddy Mijnheere and Willem Grootjans, for their help and support during all the investigation process. Without their effort, the job would have certainly been more difficult.

Additionally, the various members of the department's staff deserve a great recognition for helping in the internship integration and for assisting in every task during the investigation process. It was a pleasure to work with all the technologists, physicians, hot lab workers and PhD. students during the placement.

I would also like to thank my advisor, Prof. António Carvalho dos Santos, and co-advisor, Prof. Joana Santos, who deserve credit for their support and contribute during the work review.

My gratitude is also extended to Prof. Francisco Alves for his enthusiasm and help. Even when unusual learning methods were applied - at the very end, those were remarkable. Hope we made that dream came true.

I must thank my colleague Monique Gomes for the friendly atmosphere at work. We definitely had a great time together during the internship.

No acknowledgments would be completed without giving thanks my family, for the unconditional support provided during this long journey.

Abstract

Introduction: Whole-body bone scintigraphy represents one of the most frequent diagnostic procedures in nuclear medicine. Among other applications, this procedure can provide the diagnosis of osseous metastasis. It is known that the fraction of bone containing metastatic lesions in oncologic patients is a strong prognostic indicator of survival longevity. Moreover, the presence or absence of bone metastases will influence the treatment planning, requiring an accurate interpretation of the imaging results.

Problem: Since bone metastasis is considered as a severe complication related to increased morbidity and decreased survival, patient care becomes even more imperative. Thus, one must seek the best techniques to attain a proper result from the imaging procedure with minimal discomfort to the patient. One likely method to achieve this goal in the particular case of bone scintigraphy is reducing the acquisition time; however, images would have decreased image quality, disturbing the diagnostic results. At the present, some new techniques have emerged through which is possible to generate low count planar images of similar quality when compared to those acquired using standard protocols. Still, some methods arise with uncertainties, especially as regards the maintenance of diagnostic confidence when modifying routine protocols.

Objectives: The present work is meant to access the performance of the Pixon algorithm for image processing by means of a phantom investigation. The aim is to compare image quality and object detectability provided by raw images with those submitted to the referred processing tool. Furthermore, the reduction of acquisition time will also be under investigation. In order to accomplish the second goal, images acquired using the standard protocol will be compared to others acquired using faster protocols that were subsequently submitted to the mentioned processing software.

Materials and Methods: This investigation was performed at the Department of Radiology and Nuclear Medicine of the Radboud University Nijmegen Medical Centre, in the Netherlands. A cylinder phantom containing a set of six hollow spheres was arranged in a specific configuration, suitable for planar imaging. The phantom was filled with different sphere-to-background activity ratios (4:1, 8:1, 17:1, 22:1, 32:1 and 71:1) and scanned with different scan speeds (8 cm/min, 12 cm/min, 16 cm/min and 20 cm/min). Images were acquired using the gamma camera e.cam Signature Dual Detector System (Siemens Medical Solutions USA, Inc.), through the same acquisition parameters, with the exception of the scan speed. The 24 acquired images were processed afterwards using a software package including a whole-body enhanced planar acquisition tool (Siemens Medical Solutions USA, Inc.), with constant reconstruction parameters. Data analysis was performed by means of an objective (using image quality parameters) and a subjective (with two human observers) assessments. Statistical analysis was performed using the software Statistical Package for Social Sciences (SPSS) version 22 for Windows.

Results: Throughout the subjective assessment of every sphere-to-background activity ratios it was shown that, in general, detectability increased after processing the images. Inter-observer agreement for scores distribution of the spheres was found to be substantial either for raw or processed images. It was also demonstrated that image quality parameters improved after applying the processing algorithm within images acquired using the same scan speed. Besides, when comparing standard images (8 cm/min scan speed) with the ones acquired using faster protocols and subsequently processed, it was noticed that: images acquired with 12 cm/min scan speed can give better results, having increased values of image quality parameters and detectability; images acquired with 16 cm/min scan speed provide comparable results, having approximate values of image quality parameters and detectability; images acquired with 20 cm/min scan speed provide inferior results, having decreased values of image quality parameters and detectability.

Discussion: The attained results were also established by means of a clinical study in a distinct investigation, at the same hospital. Fifty one patients referred for prostate and breast carcinomas were included in order to find the impact of this technique on clinical practice. Patients were submitted to the standard protocol and then to an additional acquisition with 16 cm/min scan speed. After images being blindly assessed by three physicians, it was concluded that image quality and detectability were equivalent, when comparing the standard image with the one processed and acquired with a faster protocol, corroborating the results provided by the present phantom study.

Conclusion: With the intention of reducing acquisition time as much as possible and applying the Pixon processing algorithm, it was observed that the protocol with 16 cm/min might be the limit when increasing scan speed. After processing the data, this protocol gave the more equivalent results when compared to the standard procedure. Since this technique was also well established by means of a clinical trial, one can conclude that, at least for patients referred from breast and prostate carcinomas, scanning time can be reduced by fifty percent through doubling the scan speed from 8 to 16 cm/min without losing diagnostic confidence or lesion detectability.

Resumo

Introdução: A cintigrafia óssea de corpo inteiro representa um dos exames imagiológicos mais frequentes realizados em medicina nuclear. Para além de outras aplicações, este procedimento é capaz de fornecer o diagnóstico de metástases ósseas. Em doentes oncológicos, a presença de metástases ósseas representa um forte indicador prognóstico da longevidade do doente. Para além disso, a presença ou ausência de metástases ósseas irá influenciar o planeamento do tratamento, requerendo para isso uma interpretação precisa dos resultados imagiológicos.

Problema: Tendo em conta que a metastização óssea é considerada uma complicação severa relacionada com aumento da morbilidade e diminuição de sobrevivência dos doentes, o conceito de *patient care* torna-se ainda mais imperativo nestas situações. Assim, devem ser implementadas as melhores práticas imagiológicas de forma a obter o melhor resultado possível do procedimento efetuado, associado ao desconforto mínimo do doente. Uma técnica provável para atingir este objetivo no caso específico da cintigrafia óssea de corpo inteiro é a redução do tempo de aquisição, contudo, as imagens obtidas por si só teriam qualidade de tal forma reduzida que os resultados poderiam ser enviesados. Atualmente, surgiram novas técnicas, nomeadamente relativas a processamento de imagem, através das quais é possível gerar imagens cintigráficas com contagem reduzida de qualidade comparável àquela obtida com o protocolo considerado como *standard*. Ainda assim, alguns desses métodos continuam associados a algumas incertezas, particularmente no que respeita a sustentação da confiança diagnóstica após a modificação dos protocolos de rotina.

Objetivos: O presente trabalho pretende avaliar a performance do algoritmo Pixon para processamento de imagem por meio de um estudo com fantoma. O objetivo será comparar a qualidade de imagem e a detetabilidade fornecidas por imagens não processadas com aquelas submetidas à referida técnica de processamento. Para além disso, pretende-se também avaliar o efeito deste algoritmo na redução do tempo de aquisição. De forma a atingir este objetivo, irá ser feita uma comparação entre as imagens obtidas com o protocolo *standard* e aquelas adquiridas usando protocolos mais rápidos, posteriormente submetidas ao método de processamento referido.

Material e Métodos: Esta investigação for realizada no departamento de Radiologia e Medicina Nuclear do *Radboud University Nijmegen Medical Centre*, situado na Holanda. Foi utilizado um fantoma cilíndrico contendo um conjunto de seis esferas de diferentes tamanhos, adequado à técnica de imagem planar. O fantoma foi preparado com diferentes rácios de atividade entre as esferas e o *background* (4:1, 8:1, 17:1, 22:1, 32:1 e 71:1). Posteriormente, para cada teste experimental, o fantoma foi submetido a vários protocolos de aquisição de imagem, nomeadamente com diferentes velocidades de aquisição: 8 cm/min, 12 cm/min, 16 cm/min e 20 cm/min. Todas as imagens foram adquiridas na

mesma câmara gama - *e.cam Signature Dual Detector System* (*Siemens Medical Solutions USA*, Inc.) - utilizando os mesmos parâmetros técnicos de aquisição, à exceção da velocidade. Foram adquiridas 24 imagens, todas elas submetidas a pós-processamento com recurso a um *software* da Siemens (Siemens Medical Solutions USA, Inc.) que inclui a ferramenta necessária ao processamento de imagens cintigráficas de corpo inteiro. Os parâmetros de reconstrução utilizados foram os mesmos para cada série de imagens, estando estabelecidos em modo automático. A análise da informação recolhida foi realizada com recurso a uma avaliação objetiva (utilizando parâmetros físicos de qualidade de imagem) e outra subjetiva (através de dois observadores). A análise estatística foi efetuada recorrendo ao *software* SPSS versão 22 para Windows.

Resultados: Através da análise subjetiva de cada rácio de atividade foi demonstrado que, no geral, a detetabilidade das esferas aumentou após as imagens serem processadas. A concordância entre observadores para a distribuição desta análise foi substancial, tanto para imagens não processadas como imagens processadas. Foi igualmente demonstrado que os parâmetros físicos de qualidade de imagem progrediram depois de o algoritmo de processamento ter sido aplicado. Para além disso, observou-se ao comparar as imagens *standard* (adquiridas com 8 cm/min) e aquelas processadas e adquiridas com protocolos mais rápidos que: imagens adquiridas com uma velocidade de aquisição de 12 cm/min podem fornecer resultados melhorados, com parâmetros de qualidade de imagem e detetabilidade superiores; imagens adquiridas com uma velocidade de 16 cm/min fornecem resultados comparáveis aos *standard*, com valores aproximados de qualidade de imagem e detetabilidade; e imagens adquiridas com uma velocidade de 20 cm/min resultam em valores diminuídos de qualidade de imagem, bem como redução a nível da detetabilidade.

Discussão: Os resultados obtidos foram igualmente estabelecidos por meio de um estudo clínico numa investigação independente, no mesmo departamento. Foram incluídos cinquenta e um doentes referidos com carcinomas da mama e da próstata, com o objetivo de estudar o impacto desta técnica na prática clínica. Os doentes foram, assim, submetidos ao protocolo *standard* e posteriormente a uma aquisição adicional com uma velocidade de aquisição de 16 cm/min. Depois de as imagens terem sido cegamente avaliadas por três médicos especialistas, concluiu-se que a qualidade de imagem bem como a detetabilidade entre imagens era comparável, corroborando os resultados desta investigação.

Conclusão: Com o objetivo de reduzir o tempo de aquisição aplicando um algoritmo de processamento de imagem, foi demonstrado que o protocolo com 16 cm/min de velocidade de aquisição será o limite para o aumento dessa mesma velocidade. Após processar a informação, este protocolo fornece os resultados mais equivalentes àqueles obtidos com o protocolo *standard*. Tendo em conta que esta técnica foi estabelecida com sucesso na prática clínica, pode-se concluir que, pelo menos em doentes referidos com carcinomas da mama e da próstata, o tempo de aquisição pode ser reduzido para metade, duplicando a velocidade de aquisição de 8 para 16 cm/min.

Contents

Index of Figures

Index of Tables

List of Abbreviations

ACR	American College of Radiology
ALARA	As Low as Reasonably Achievable
BV	Background Variability
Bq	Bequerel
CNR	Contrast-to-noise Ratio
CRC	Contrast Recovery Coefficient
COV	Coefficient of Variation
cps	Counts per second
CT	Computed Tomography
DICOM	Digital Imaging and Communications in Medicine
EANM	European Association of Nuclear Medicine
ECT	Emission Computed Tomography
EPP	Enhanced Planar Processing
FPB	Fractal Pixon Basis
FWHM	Full Width at Half Maximum
HDP	Hydroxymethylene Diphosphonate
IAEA	International Atomic Energy Agency
ICRU	International Commission on Radiation Units and Measurements
IEC	International Electrotechnical Commission
keV	Kiloelectronvolt
LEHR	Low Energy High Resolution
Matlab	Matrix Laboratory
MBq	Megabequerel
MRI	Magnetic Resonance Imaging
mSv	Milisievert
NaI(Tl)	Thallium activated Sodium Iodide
NEMA	National Electrical Manufacturers Association
PMT	Photomultiplier Tube

PET	Positron Emission Tomography
PSF	Point Spread Function
ROI	Region of Interest
SNR	Signal-to-Noise Ratio
SPECT	Single-photon Emission Computed Tomography
SPSS	Statistical Package for Social Sciences
Sv	Sievert
UPB	Uniform Pixon Basis
^{18}F-FDG	18F-fluorodeoxyglucose
^{99m}Tc	99m-Technetium

Introduction

The skeleton it the most common organ to be affected by metastatic lesions. Although metastatic bone disease may arise from any primary malignant tumour, tumours arising from breast, prostate, thyroid, lung and kidneys have a special propensity to spread to bone (1).

It was estimated that bone metastases arise in 14-70 % of all tumour patients. Additionally, evidences of metastatic bone disease are reported in 70-85 % of patients at post-mortem examination. This particular site of disease produces the greatest morbidity by frequently causing pain. For that reason, the biggest concern for patients with metastatic bone disease is the general loss in their quality of life (2).

Metastatic bone disease is a chronic condition in which the survival from the time of diagnosis varies among different tumour types. Therefore, there is an increasing range of developed treatments that intend to slow the progression of the disease. Bone involvement often results in some important clinical features: pain, pathological fracture, hypercalcaemia and spinal instability with cord compression. These complications are referred as skeletal complication events arising from the considerable morbidity and occur, on average, every 3 to 6 months. In practice, however, these events are not so regular, depending on the progression and the extension of the disease (3).

Patients with a known primary tumour, in particular those mentioned before, must be monitored for bone metastases. Radiography and radionuclide bone scintigraphy are the most common options for diagnostic imaging, though, more advanced techniques are becoming more popular with the increase of their accessibility (4).

Each imaging technique depicts different aspects of tissues, influencing the appearance of the different malignant bone lesions. Still, whole-body planar bone scintigraphy has been considered as the standard technique for bone metastases screening, by providing the essential information concerning location, prognosis and evaluation of response to therapy (5, 6).

To generate an adequate diagnostic image in nuclear medicine, an appropriate balance between image quality and radiation dose is required. According to this, it is desirable to keep radiation dose as low as reasonably achievable, according to the ALARA (As Low as Reasonably Achievable) principle, together with an appropriate scan duration (7).

In the particular case of bone metastases imaging, considering that pain is the most prevalent symptom, efforts could be made in order to reduce the scanning time. Given that the positioning required for the procedure possibly will induce discomfort for the patient, it would be valuable to obtain an accurate clinical diagnosis with reduced acquisition time. Still, any approach should by carefully explored before being set into clinical practice.

With this purpose, the present study investigated the Pixon method, an algorithm for image processing that will possibly allow the conception of an innovative imaging protocol for whole-body planar bone scintigraphy. With the final goal of reducing the acquisition time of the procedure, a phantom investigation was carried out so that the performance of the referred algorithm could be entirely accessed.

CHAPTER 1

Metastatic Bone Disease

Metastatic bone disease

In advanced oncologic disease, the development of metastatic bone disease can be a common and severe complication. Bone is the most common site for metastasis in cancer and is of particular interest in breast and prostate cancers because of the prevalence of these diseases (**Table 1**). Up to 70 % of patients with this type of cancer develop this condition. Carcinomas of lung, kidney, thyroid and melanomas are other common tumours that metastasize to bone (2, 3, 8).

Bone lesions put oncological patients at high risk of skeletal complications. It is a condition associated with increased morbidity and reduced survival. The major complications related to bone involvement are severe and debilitating pain, spinal cord compression and pathological fracture, which contribute to the decreased quality of life of the patient (2, 8, 9).

Table 1 – Incidence of bone metastases in different types of cancer.
(9)

Type of Cancer	Five-year world prevalence	Incidence of bone metastases	Median survival (months)
Myeloma	144.000	70-95 %	6-54
Renal	480.000	20-25 %	6
Melanoma	533.000	14–45 %	6
Thyroid	475.000	60 %	48
Lung	1394.000	30–40 %	6
Brest	3860.000	65-75 %	19-25
Prostate	1555.000	65-75 %	12-53

I. Pathophysiology of Bone Metastases

Normal bone undergoes continuous remodelling. It is a lifelong process essential to maintain mechanical function wherein old bone is removed from the skeleton through resorption and new bone is added by ossification. Bone remodelling involves continuous removal of discrete packets of old bone, replacement of these packets with newly synthesized proteinaceous matrix and subsequent mineralization of the matrix to form new bone. Thus, bone is added where needed and removed where it is not required. This process is necessary to maintain the structural integrity of the skeleton as well as to support its metabolic functions as a storehouse of calcium and phosphorus (2, 10).

The mechanisms of bone formation and bone removal represent two tightly coordinated events of the normal remodelling cycle. They require synchronized activities of multiple cellular participants to ensure their sequentially occurrence at the same anatomical location in order to preserve bone mass. Consequently, this process depends on the orderly development and activation of osteoclasts and osteoblasts, involving series of highly regulated stages that depend on the interactions of these two cell lineages (10).

In many advanced cancers, the skeleton, after the lungs and liver, is the third most common site of metastatic disease. The metastasis of tumour cells to the bone matrix involves a complex cascade of events (**Figure 1**) (9, 11).

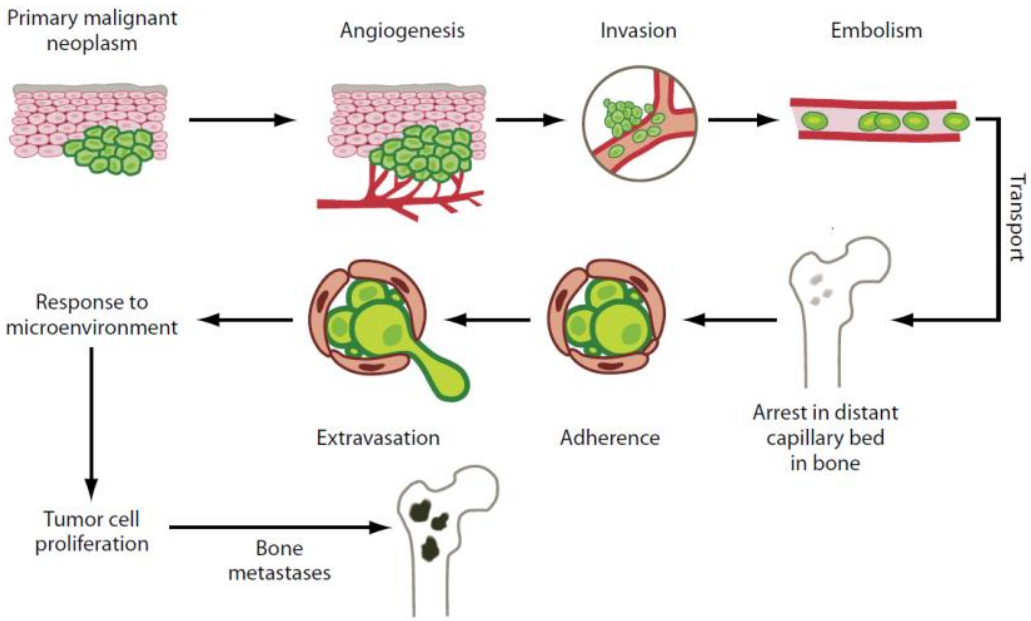

(9)

Figure 1 – Mechanism of tumour metastasis to bone.

This multistep mechanism involves a bidirectional interaction of the tumour cells with cellular elements in three different microenvironments: the site of primary malignant neoplasm, the transport and the bone microenvironment (8).

Bone metastasis begins when primary tumour cells detach from their place of origin (primary tumour) by forming new blood vessels (angiogenesis), invading the vasculature. Thus, they will reach the skeletal sites by adhering the vascular endothelial cells of distant capillaries of the bone. When the cells escape the circulation they can establish themselves, proliferate and then induce metastatic lesions. Once tumour cells have colonized the bone matrix, they secrete a large number of soluble growth factors that stimulate the activity of osteoclasts and/or osteoblasts, disrupting normal bone remodelling (8, 9).

II. Clinical Presentation

Metastatic bone disease is the cause of considerable morbidity in advanced cancer situations. The clinical presentation of this condition includes pain, pathological fracture, hypercalcaemia and spinal instability with medullar compression (2, 3).

1. Pain

The clinical presentation of metastatic bone disease is variable, but pain is the most common presenting symptom with either osteolytic or osteoblastic lesions. This condition is shown in 75 % of patients during this type of clinical evaluation. Painless lesions are usually diagnosed during staging follow-up examinations to patients with a known history of carcinoma. Pain incompletely relieved by rest and night pain are not specific indications of metastasis, however they are typical symptoms. Furthermore, weight-bearing bones may become symptomatic early in the course of disease, whereas bones such as the flat bones of ribs or sternum may remain asymptomatic until late in the disease, often until pathologic fracture occurs (11).

Different sites of bone metastases are related with distinct pain syndromes. Common sites of metastatic involvement associated with pain are the base of skull, vertebrae, pelvis and femur (3).

Lytic lesions with bone loss are usually associated with mechanical pain, whilst blastic lesions can cause functional pain through the loss of bone's structural integrity. The tumour type, location, number or size of metastases and the patient's characteristics are not correlated with the presence of and the severity of pain. In general, this complaint develops gradually becoming progressively more severe. It can be divided into two types of pain according to the presented symptoms: continuous or incident pain; and the mechanism of the disease: primary or secondary. Primary pain involves bone resorption with disruption of skeletal architecture and micro-fracture. In contrast, secondary pain is characterized by nerve root infiltration or compression and reactive muscle spasm. For this reason, effective treatments are needed in order to improve the patient's quality of life (2).

2. Pathological Fracture

The term pathological fracture refers to the fracture that occurs in the area of a neoplasm. It can be caused by any type of bone tumour, but the majority are secondary to metastatic carcinomas. In some conditions, it might be the first sign of bone metastasis. Despite the fact that the incidence is uncertain, breast cancer is the most common primary site. The destruction of cortical bone by the tumour cells will result in trabecular disruption and microfractures with consequent total loss of bone integrity. This type of fracture can occur spontaneously or after a minor injury, but it probability increases with the duration of the metastatic involvement (2, 12).

3. Hypercalcaemia

Hypercalcaemia is defined as an elevation of plasmatic ionized calcium. In most cases, hypercalcaemia is a result of bone destruction, and osteolytic metastases are observed in 80 % of cases. This clinical feature occurs particularly in patients with breast malignancies, reflecting an association with the presence of liver metastases. The signs and symptoms of hypercalcaemia are nonspecific, but normally include pain, fatigue, anorexia and constipation. If untreated, the result will be the deterioration of renal function and mental status (2, 3).

4. Spinal instability with cord compression

Spine is the most common site of bone metastasis, making neurologic symptoms and spinal instability very frequent. Spinal instability will lead to mechanical pain with consequent impact on quality of life. Besides, spinal cord compression is referred as a medical emergency, which requires urgent evaluation and treatment. Local pain usually precedes radicular pain and may predate the appearance of other neurologic signs by weeks or months (2, 3).

III. Imaging Diagnosis

There are several imaging modalities available for the study of bone metastases. To increase the probability of detecting bone metastases in a timely and cost-effective manner, the most effective imaging procedures must be requested (**Figure 2**) (13).

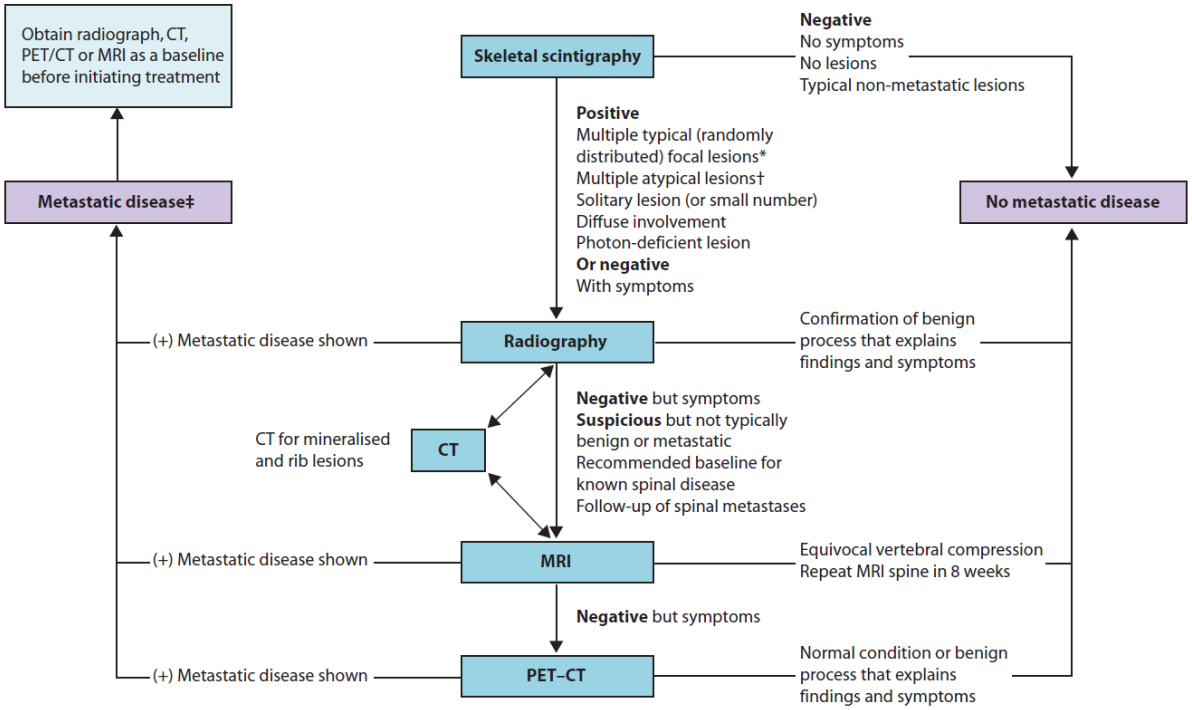

(13)

Figure 2 – Suggested algorithm of imaging studies for the osseous metastases.

Each imaging modality depicts different aspects of tissues. Hence, the appearance of the various types of bone lesions can considerably differ depending on the imaging technique (**Figure 3**) (5).

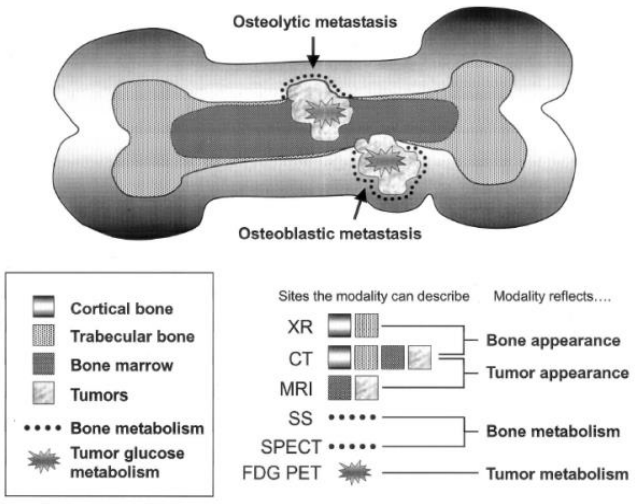

(5)

Figure 3 – Illustration of metastatic lesions depicted by different imaging modalities. Plain Radiograph (XR); Computed Tomography (CT); Magnetic Resonance Imaging (MRI); Skeletal Scintigraphy (SS); Single Photon Emission Computed Tomography (SPECT); Positron Emission Tomography (PET) with ^{18}F-fluorodeoxyglucose (^{18}F-FDG).

1. Radiography

For some types of tumour, skeletal metastases are readily detected by radiological studies, forming an important aspect of clinical disease management. Thus, the radiological evaluation of focal symptoms is the first step in the assessment of suspected bone metastases, to visualize the painful area and access the structural integrity of the bone. However, it is not generally recommended as a screening method due to its poor sensitivity, which depends partly on lesion location (11, 13, 14).

Apart from the limited contrast for differentiation of the various soft tissues, the main disadvantage of this method is that anatomical structures are projected in one plan, leading to superimposition of a metastatic nodule with normal anatomic structures. Still, radiography may help to distinguish metastases from other conditions along with accessing the risk of pathological fracture (15).

Bone metastases are classified regarding the radiological classification of the observed changes in bone architecture, being usually described as: osteolytic, when bone destruction arises by the action of osteoclasts, as observed in breast cancer patients; osteoblastic, which are characterized by sclerosis, being predominant in prostate cancer conditions; or mixed, where both processes of resorption and formation occur at the same time. Although, it is important to remember that any cancer can appear in any pattern (2, 8, 11).

Radiographs are important for the interpretation of abnormal findings in the Technetium-99m (^{99m}Tc) bone scintigraphy, which should be correlated prior to confirming the diagnosis of metastatic bone disease (11).

2. Technetium-99m Bone Scan

Since the introduction of ^{99m}Tc-based scan agents, the radioisotope bone scintigraphy has been the standard method for detection of skeletal metastases. This imaging method is more sensitive than radiography for detection of other skeletal sites of tumour involvement. Despite its low specificity and higher false-positive rates, it can detect these lesions earlier than plain films. False-negative findings can appear when pure osteolytic metastases are growing fast, when bone turnover is slow or when the site is avascular (5, 12, 14).

Bone scintigraphy is generally considered sensitive for detecting osteolytic or osteoblastic bone metastases on whole-body images. Moreover, the advantage of this kind of examination is not for diagnosis but rather for screening, as it is widely available and can produce quick images at reasonable cost (5).

Due to its particular interest for this study, this topic will be further discussed on the next chapter.

3. Computed Tomography and Magnetic Resonance Imaging

Computed Tomography (CT) and Magnetic Resonance Imaging (MRI) can depict anatomic changes in more detail than bone scintigraphy (13).

CT is the study of choice when looking for bone detail and cortical damage since delineates cortex and can help the description of abnormal calcifications. Due to its technical advantages, CT is the most frequently used imaging diagnostic method for diagnosis, staging and detection of nodal and distant metastases, monitoring and follow-up in oncology (12, 13, 15).

For accessing bone metastases, MRI is preferable to CT due to its excellent soft-tissue contrast resolution, which allows better depiction of the marrow cavity and adjacent soft-tissues. MRI is often performed at the site of metastatic disease, being useful in cases in which the bone scintigraphy is negative but localized symptoms are present. This imaging technique is very sensitive to early marrow replacement and can locate metastases prior to their appearance on radiographs and CT scans, even with low resolution for bony anatomy. Through this study is also possible to distinguish between osteoporotic and malignant fractures (11, 12, 13).

If MRI and CT are not capable of detecting the disease and clinical suspicion of bone metastasis remains, the use of more advanced techniques is recommended (13).

4. PET-CT

Positron Emission Tomography (PET) is a tomographic technique that produces high-resolution images with three-dimensional distribution of radioactivity through the detection of high-energy photon pairs, emitted by the positron emitter labelled radioisotope. The glucose analogue 18F-Fluorodeoxyglucose (^{18}F-FDG) is the most commonly used tracer since the accumulation in tissue is proportional to the amount of glucose utilization. This radiopharmaceutical is wide used in oncology because of the high glucose uptake by many tumours (13, 16).

In opposition to PET, CT generates tomographic images using an x-ray source, producing morphological and anatomic views with high resolution. Therefore, the information derived from CT can be used to increase the precision of localization, extent and characterization of lesions detected by ^{18}F-FDG PET (16).

The combination of PET and CT has recently revealed various implications for evaluating bone metastases. Due to its high sensitivity, fluorine ^{18}F-FDG PET is the modality of choice for standard oncologic staging, restaging and treatment monitoring evaluations. Besides, CT data of the PET-CT studies allows the reduction of false-positive rate by determining the

morphology of the scintigraphic lesions through fusion of functional images with the anatomic dataset (13, 17, 18).

PET-CT allows soft-tissue contrast resolution that is absent with bone scintigraphy. Thus, it can help better differentiate whether FDG-avid lesions are truly located within bone versus adjacent soft tissue (17).

CHAPTER 2

Planar Nuclear Imaging

Planar Nuclear Imaging

Nuclear medicine is a diagnostic imaging modality in which information is obtained from the way the tissues and organs process radiolabeled compounds. The main purpose is the quantitative measurement of physiologic and biochemical characteristics of the body. This involves administrating a radioactive agent, which will be carried throughout the body by circulation and then taken up by organs where radioactive decay within the patient begins. This means that the unstable nuclei will decay to a more stable state by emitting energy in the form of radiation such gamma rays. Radioactive decay has applications in medicine for both diagnostic and therapeutic purposes (19, 20, 21).

The emitted radiation has high energy and can be detected and measured by suitable detection devices. The majority of those radiotracers used in diagnostic imaging are gamma emitters. That type of radiation can be detected by using imaging devices such gamma scintillation cameras, Single-Photon Emission Computed Tomography (SPECT) and PET scanners. In the particular case of planar scintigraphy, a simple gamma scintillation camera should be used (19, 22).

I. Gamma Camera

There are two types of nuclear imaging methods: single-photon imaging and PET. These two methods are distinguished by the physical properties of the administrated radioisotopes, which can radioactively decay by single or double-photon emission (21).

A gamma camera is a single-photon imaging technique, also referred as scintillation camera or Anger camera, being the primary imaging instrument used in nuclear medicine. The basic components of a gamma camera system are the collimator, the scintillation (or semiconductor) detector and readout electronics (**Figure 4**) (20, 21, 22).

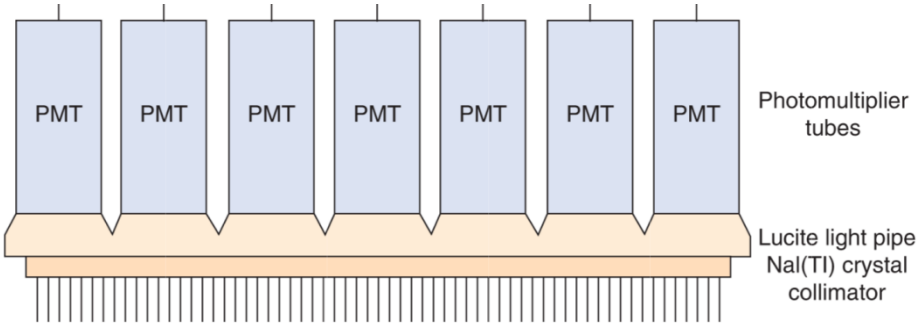

(23)

Figure 4 – Diagram representing the components inside a gamma camera.

Gamma cameras are used in both planar imaging and SPECT. Planar imaging produces a two-dimensional image of a three-dimensional object. Those images contain no depth information and some structures can be superimposed. To overcome this drawback, at least two views of the patient should be taken, depending on the procedure. For transaxial tomography with SPECT, the camera is rotated around the patient, acquiring multiple views from different angles. These projections are used to calculate the transverse activity distribution, applying suitable reconstruction methods. This procedure is performed with either rotating Anger cameras (with two or three camera heads) or specific ring or partial ring detector systems (24, 25, 26).

1. Physics and Instrumentation

The principle of gamma cameras relays on the conversion of the photons emitted by the radionuclide in the patient into a light pulse and subsequently into a voltage signal (**Figure 5**). This signal is used to create an image which reflects the distribution of the radionuclide. Thus, scintigraphic instrumentation consists of scintillation crystals to convert gamma ray energy (photons) into visible light, specific light sensors, readout electronics and image processing units (22, 25).

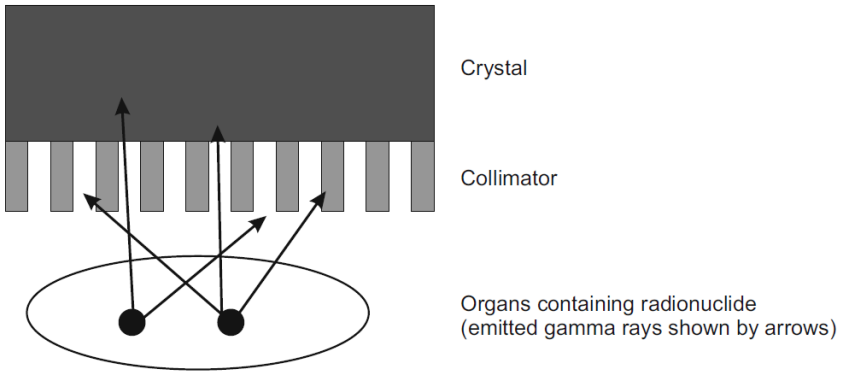

(27)

Figure 5 – Ilustration of a gamma camera.

1.1. Collimator

The collimator is a device placed between the crystal and the object of study. The main function of this device is to limit the photons that interact with the crystal to only those that have a specific path relative to the detector surface. Despite the fact that collimators make the systems less efficient by reducing the counting rate, they are essential for the formation of the image since the emission of gamma rays from the patient is isotropic (25, 28).

Lead is usually the material of choice for collimators due to the combination of high density with high atomic number. High density materials are required due to the correlation between the attenuation coefficients, which must be high to ensure gamma photon absorption (28).

There are two basic types of collimators, defined as multihole and pinhole:

- A **multihole collimator** consists of a gamma radiation absorbing material with great abundance of holes distributed in a network. This configuration makes possible to select certain incident photons and to filter scattered rays that disturb the image formation. The barriers that confine those holes are named collimator septa. The septa must be thick enough to absorb most of the photons incident upon them. Therefore, collimators must have thicker septa for higher energy photons. Modifying a collimator should involve a compromise between spatial resolution and efficiency, since the thickness of the collimator, the diameter of the holes and the septa thickness are directly related to the image quality obtained (23, 28).
  Multihole collimators differ mainly in their geometry. The holes may be hexagonal, square or triangular; however, most state-of-the-art collimators have hexagonal holes and are usually made of lead foil. These collimators can also be distinguished by the alignment of the holes: in a parallel (**Figure 6**), converging and diverging manner (**Figure 7**) (22, 23).
  The parallel-hole is the most widely used multihole collimator, which consists of an array of parallel holes essentially perpendicular to the plane of the scintillation crystal, presenting a real-size image to the detector (orthogonal geometry). The type of parallel-hole collimator should be chosen according to the energy of the isotope being imaged: low energy (up to 150 kiloelectronvolt (keV)), medium energy (up to 280 keV) and high energy (up to 364 keV) (22, 26).

- **Pinhole collimators** are thick conical collimators with a single hole in the bottom centre, based on the obscure camera principle in which light rays pass through the pinhole aperture and are projected to form an inverted image on the scintillation crystal (**Figure 6**). Since the radiation pass through a small aperture, only a small percentage of the emitted photons can reach the crystal, resulting in reduced sensitivity. Another disadvantage of the pinhole is the distortion that occurs due to the finite size of the hole (26, 28).
  The pinhole collimators are routinely used for images requiring high resolution such small organs like the thyroid and certain skeletal regions (hips or wrists) as a result of the possibility of magnifying and improving spatial resolution (22, 28).

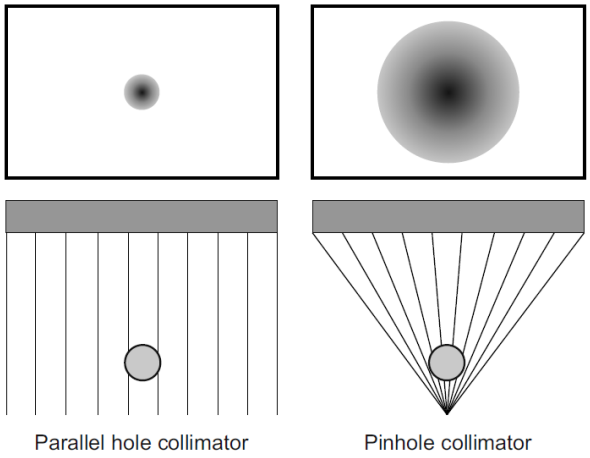

(27)

Figure 6 – Main collimator configurations and their effect on the acquired image.

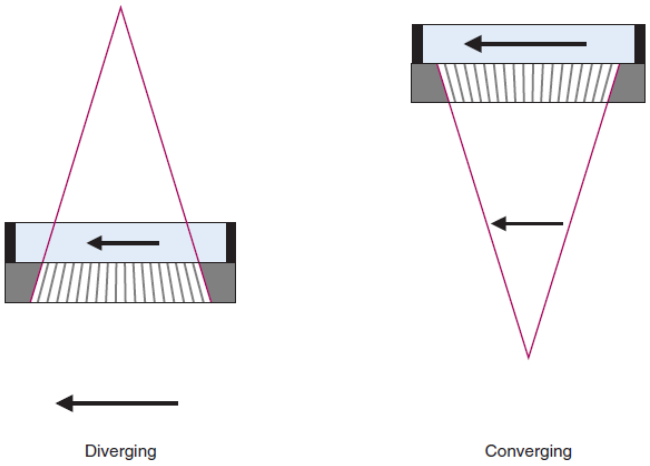

(29)

Figure 7 – Diverging and converging gamma camera collimators.

1.2. Scintillation Crystal

The scintillation crystal is another component of a gamma camera, consisting mainly of a crystal of thallium activated sodium iodide, NaI(Tl). It is surrounded by a highly reflective material that is intended to maximize the light output, having also a thin aluminium casing for hermetical sealing. Despite the numerous available options, NaI(Tl) remains the crystal of choice for single photon detection with energies of 70-360 keV. Originally, the crystals had a circular cross section, but currently most cameras use a rectangular crystal 30-50 cm wide and 0.9-1.2 cm thick (**Figure 8**) (20, 21, 25).

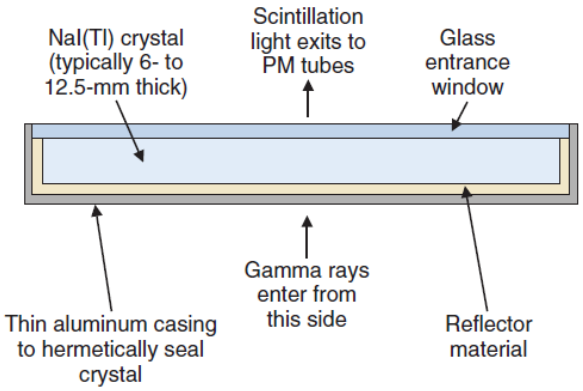

(29)

Figure 8 – Schematic cross-section of a NaI(Tl) crystal for a gamma camera.

The purpose of a scintillator is to convert the gamma ray energy emerged from the patient into visible light after passing through the collimator. When ionizing radiation interacts with a scintillator, electrons are raised to an excited energy level. These electrons will then fall back to a lower energy state, producing a pulse of fluorescent light. The amount of light generated is directly proportional to the intensity of the absorbed energy, depending on the characteristics of the material (22, 23).

Scintillation materials must have specific proprieties such (23):

- High fraction of deposited energy that is converted into light - **conversion efficiency**;
- Short **decay time**, so the light can be emitted promptly after an interaction;
- Transparency to its own emissions to avoid reabsorption of the emitted light;
- Large attenuation coefficient to improve **detection efficiency** (materials with higher densities and atomic numbers).

Clinical nuclear medicine cameras are built with organic scintillators because of their high detection efficiency for gamma rays. The advantages of NaI(Tl) are: a very high conversion efficiency (around 13 %), reasonable decay time (230 nsec) and inexpensive production in great quantities (large crystals can be manufactured). However, it is a fragile and hygroscopic material which needs to be hermetically sealed in airtight containers, making this its main disadvantage (23, 25).

Although the energy resolution of a gamma camera is determined by the whole system, the light yield of the scintillation crystal is very significant, because it can improve the image contrast. The energy resolution expresses the ability of the detector to differentiate gamma rays of closely spaced energies. NaI(Tl) has a moderate energy resolution, which is an important propriety that provides the means to discriminate against scattered radiation (20, 25, 28).

1.3. Photomultiplier Tubes

Having scintillation photons is not enough for the image formation. Thus, scintillation detectors incorporate a means of signal amplification that converts those photons into an electronic signal. This is accomplished by electronic devices referred as photomultiplier tubes (PMTs) (23, 30).

Gamma cameras have an array of these devices located behind the scintillation crystal. They collect the light generated in the crystal, giving rise to electrical signals that contain information to determine the energy and position of interactions taking place in the crystal. Those interactions are processed individually, which requires the use of fast electronics and low dead time in the detector to allow high counting rates (28, 30).

The number of PMTs is very important for the accurate localization of scintillation events, because the source can only be precisely tracked when considering the signals from other surrounding PMTs. Therefore, the greater the number of PMTs, the greater the resolution. The thickness of the crystal must also be suited, because if the source is located far from the PMT (thicker crystals) the signal will be weak and the location not certain, degrading the spatial resolution (20, 22, 28).

The main components of a PMT are: the photocathode, focusing grid, several dynodes with high voltage supply and the anode (**Figure 9**).

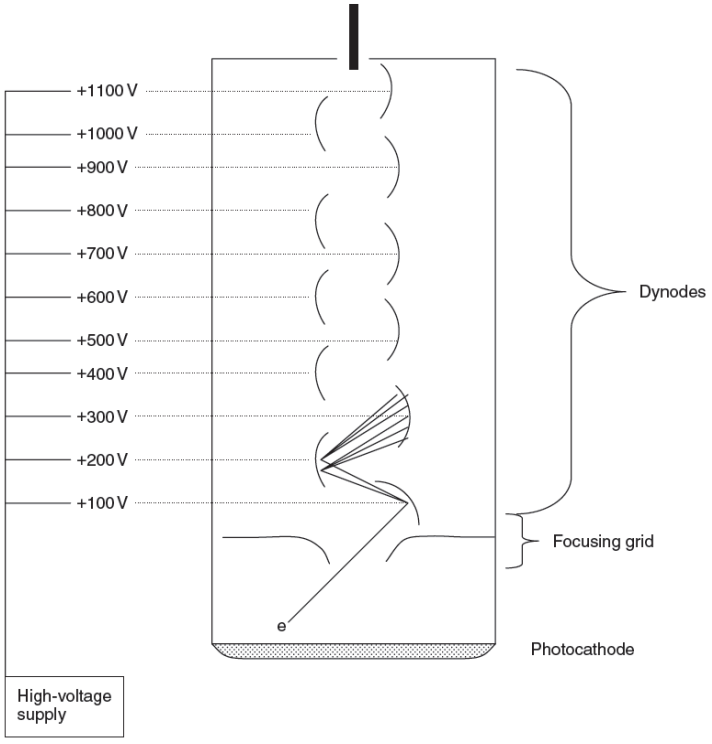

(30)

Figure 9 – Illustration of the fundamental structure of a PMT.

- The **photocathode** is near the window of the PMT and converts scintillation photons into electrons. It is made of a photoemissive material, usually metal alloys, that has extra electrons that will be released into the vacuum space of the PTM when interacting with scintillation photons;
- The **focusing grid** accelerates the electrons towards the first dynode;
- A **series of dynodes** multiply the electrons generated at the photocathode into a measurable electronic signal. They are also made of metal alloys, each one with higher potential than the last, emitting electrons toward each other;
- At last, the **anode** collects the produced electrons from the final dynode and gives off a voltage signal (28, 30).

1.4. Associated Electronics

When a gamma ray interacts in the scintillation crystal, scintillation photons are emitted. Those, in turn, cause the emission of a few electrons at the photocathode of the PMT that will be converted to a measurable electronic signal at the anode of the PMT. Although the signal given off by the PMT anode is measurable, it is considered small. Thus, a preamplifier and an amplifier are used to increase the output signal by a variable amount. Besides, they are also useful to shape and shorten the pulse in order to provide a series of discrete pulses easier to analyze (30).

The PMT signals are converted into a numeric magnitude by analog-to-digital converters, so that the energy and positions can be calculated by computer algorithms that can accurately model those signals with the source position (**Figure 10**) (20).

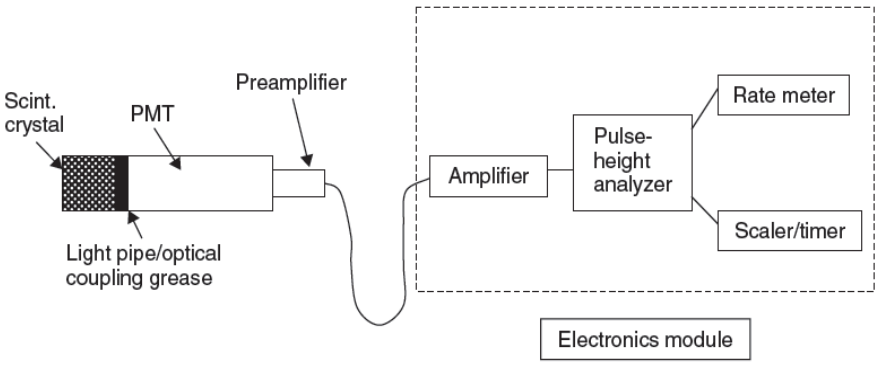

(30)

Figure 10 – Diagram of a scintillation detector with the basic structure of the signal acquisition module.

2. Measures of Performance

A scintillation camera has two types of measures of performance: extrinsic and intrinsic. Extrinsic measurements are performed with the collimator attached to the detection system. In contrast, if the collimator is not present, the measurements are called intrinsic. Extrinsic measurements give the best indication of clinical performance while intrinsic measurements are more useful to compare the performance of different cameras (23).

2.1. Resolution

Resolution is one of the common performance parameters for gamma cameras. It can be referred as spatial or energy resolution:

- **Spatial resolution** is the measure of ability of an imaging device to separate objects close together in space. It reveals the accuracy of the system to depict spatial variations in activity concentration and to distinguish as separate radioactive objects in close proximity;
- **Energy resolution** is the ability to discriminate light pulses induced by gamma photons of differing energies. It evaluates how well a detector distinguishes between gamma rays of closely spaced energies (22, 23, 30).

Resolution can be increased by using more, smaller holes or by making the collimator longer. This, however, reduces the fraction of photons detected by the system due to the increased amount of lead in the collimator (26).

2.2. Sensitivity

This parameter is defined as the overall ability of the system to detect radioactive emissions from a source. Thus, sensitivity increases with the fraction of missions that are detected. Sensitivity can be increased for multihole collimators by increasing the size or shortening the length of each hole. However, this will occur at the expense of resolution. As a result, a balance between these two parameters needs to be done (26).

2.3. Uniformity

Uniformity is the quantity that measures the response of the camera to uniform irradiation of the detector surface, according to the consistency of the obtained image. Field uniformity is tested intrinsically and extrinsically. The intrinsic measurement is performed using a point radionuclide source in front of the camera without collimators, whilst system uniformity is

assessed by placing a uniform planar radionuclide source in front of the collimated camera. The acquired images are then quantitatively analysed by a computer in order to obtain the results (22, 23).

2.4. Dead Time

If scintillation events occur too close together in time, the electronic system can be unable to count all the events that reach the crystal. The time after an event during which the system is unable to respond to another event is referred as the dead time, being strongly related to the count rate of the detector (22).

II. Bone Scintigraphy

Bone scintigraphy or skeletal scintigraphy is one of the most common procedures in routine nuclear medicine. It is a diagnostic study that aims the evaluation of the distribution of active bone formation within the body (31, 32).

With this technique is possible to obtain whole-body or limited bone scintigraphic images, according to the indications for the examination. In whole-body procedures, planar images of the entire skeleton are acquired, including anterior and posterior views (32).

The radionuclide bone scintigraphy is an extremely sensitive method for demonstrating a variety of skeletal disorders, allowing earlier diagnosis or demonstrating more lesions than conventional radiological techniques. The main indications for referral are: detection and follow-up of metastatic disease, trauma difficult to access on radiographs, sport injuries, evaluation of prosthetic joints and rheumatologic disorders (22).

1. Radiopharmaceutical – ^{99m}Tc

Technetium is a transition metal that, in the form of one of its isotopes ^{99m}Tc, is the most widely used radioisotope in nuclear medicine. It has a half-time period of 6 hours, where 87 % of the decays produce 140 keV gamma photons (**Figure 11**). This property makes ^{99m}Tc suitable for imaging with gamma cameras, being also safe regarding the patient's radiation dose (28).

At the present, phosphate analogues labelled with ^{99m}Tc are the radiopharmaceuticals of choice for bone scintigraphy. They are widely used on account of the good localization in the skeleton as well as the rapid clearance from soft tissues. These radiopharmaceuticals can, therefore, provide a better image of bones due to the lower blood and tissue concentrations, giving a higher ratio of bone to tissue (31, 33).

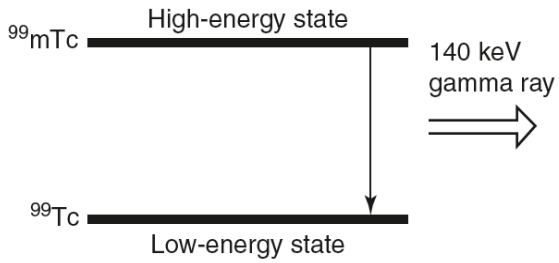

(34)

Figure 11 – Scheme of gamma ray production with ^{99m}Tc.
The atom passes from a high-energy state to a low-energy state, releasing a gamma photon with a peak energy of 140 keV.

1.1. Mechanism of Accumulation

Two major factors control the accumulation of the radiotracer in the bone: blood flow and extracting efficiency. The average administrated activity for a single injection should be around 500 megabequerel (MBq), corresponding to an effective radiation dose of approximately 3 milisieverts (mSv). The uptake of any agent in the body depends on the blood supply, the capillary to bone transfer and the degree of osteoblastic and osteoclastic activity. After the radiopharmaceutical injection, about 50 % of the activity accumulates in the skeleton according to the following steps (22, 31, 33, 35):

- Generally, the clearance of ^{99m}Tc-labeled radiopharmaceuticals from the vascular compartment is fast, with half-times of 2-4 minutes;
- The peak uptake in the bones is variable, but is normally reached at 1 hour after injection;
- The bone to background ratio varies with the different clearance and uptake rates of other tissues, having its maximum later at 4-6 hours;
- The combination of contrast, rapid renal excretion, peak uptake, radionuclide decay and practical issues, results in optimal imaging 2-4 hours after tracer injection. At this time, about one third of the administrated dose is bound to bone.

2. Patient Preparation

There is no special patient preparation concerning the bone scintigraphy. At the beginning, patients need to have a complete understanding of the procedure, including the reason of the delay between radiopharmaceutical administration and scanning, which is approximately 3 hours to achieve good bone accumulation and a low soft-tissue level of the radiopharmaceutical (33).

Unless contraindicated, patients should be well hydrated, being instructed to drink water between the time of injection and the time of delayed imaging. It will aid the clearance of the radiopharmaceutical from the body. Furthermore, voiding frequently is also important to reduce the radiation dose to the bladder and the activity on the bladder during the exam. Thus, the patient should also be requested to urinate immediately before the scan. During this phase, contamination with urine must be avoided, because it can lead to false-positive findings on the study (22).

It is also essential to remember that before considering submit a patient to a scintigraphic procedure, some precautions need to be taken: in case of pregnancy, a clinical decision is necessary to weigh the benefits against the possible harm; breast-feeding should be discontinued at least for 4 hours and for 24 hours post injection when possible (33).

3. Imaging Metastatic Disease

The ability to image the entire skeleton makes planar bone scan unique when compared with other diagnostic techniques, resulting in a fast, cost-effective survey of the skeletal system. For this reason, the standard technique of bone scintigraphy in oncology is considered to be the whole-body scintigraphy. The overall sensitivity for detecting bony metastases is 95 %, with a false-negative rate of 2 % to 5 % (33, 36).

In the evaluation of oncological patients, whole-body bone scintigraphy provides the essential information related to the sites of osseous metastases, their prognosis and evaluation of osseous tumour response to chemotherapy and radiation therapy (6).

Many patients with known neoplasms and bone pain have metastases documented by the bone scintigraphy. Regardless, is also very important to scan patients with asymptomatic tumours that have a propensity to metastasize to bone, such as breast, lung and prostate carcinomas. For this reason, most patients are submitted to a whole-body bone scintigraphy within 6 months to 1 year, so that the extent of bone anomalies can be identified and compared in successive examinations. However, some variations may occur, modifying the conditions of the procedure throughout the series of scintigraphic scans (6, 22).

Most metastases are multiple and relatively obvious but the interpretation may sometimes be difficult because of the single lesions, which have high false-positive rate. In general, bone metastases are observed as an increased uptake. The inherent osteoblastic response induces the deposition of radiotracer, generating a positive finding on the image. The usual pattern of metastatic bone disease is multiple focal lesions all over the skeleton, with the greatest involvement usually in the axial skeleton. Despite the high sensitivity of this technique, tracer uptake in bone scintigraphy is not specific for most metastatic bone disease (5, 11, 12, 22, 26, 35).

Since metastases are usually located in the bone marrow, it is not the metastasis itself that shows up on the bone scintigraphy, but the reaction of the bone to the expanding malignant bone marrow. The lesions have cold signal when they are highly aggressive with fast expanding, since there is not enough time for the bone to respond and the regional blood flow may be damaged to such extent that the tracer cannot be delivered (31).

If a diffuse involvement of the skeleton by metastases is noticed, it may initially appear as though there has been remarkably good, relatively uniform uptake in all bones. This occurrence is commonly known as a *superscan*. If this finding is induced by metastases, a significantly decrease in renal activity with diffusely increased activity throughout the axial skeleton will be noted. This condition is commonly a result of prostatic cancer, but other tumours such breast cancer and lymphoma may also be the source of this appearance (22).

Follow-up scans of advanced breast and prostate cancer should be interpreted with caution. When imaging bone tumour response on a planar bone scintigraphy, findings usually emerge as a decreased intensity of radionuclide uptake by the metastatic foci. However, in the first 3 months of chemotherapy, a favourable clinical response by focal bone metastases may result in healing and increased uptake, which is a good prognostic sign. Disease progression is usually suggested by bone lesions that appear 6 months or later after treatment (22).

3.1. Imaging Technique

According to the procedure guidelines of the European Association of Nuclear Medicine (EANM), image acquisition for bone scintigraphy should be performed using a single or a double-head gamma camera, equipped with a low-energy, high resolution collimator, suitable for the 140 keV photopeak of ^{99m}Tc (33).

In adults, whole-body bone scintigraphy is performed with continuous imaging, obtained in both anterior and posterior views. Routine images of the skeletal phase are usually acquired between 2 and 5 hours post-injection, where the scanning speed might be adjusted with the purpose of obtaining more than 1.5 million counts in each routine image view. For a routine study, the average procedure imaging time is about 30 minutes. The suggested scan speed for a whole body delayed image is 8 to 15 cm per minute (32, 33, 37).

3.2. Pitfalls and Artefacts

There are several sources of error in bone scintigraphy. They can be artefact related to the patient or to the technique itself.

Technical artefacts include equipment, radiopharmaceutical and image processing problems due to (33, 38):

- Poor quality control and calibration;
- Inadequate preparation of the radiopharmaceutical that modifies biodistribution and compromises the diagnostic quality of the images;
- Extravasation at the site of injection, which is the most common artefact on bone scintigraphy;
- Source-to-detector distance greater than necessary;
- Imaging at wrong timing.

The main patient-related artefacts can be described as (33, 38):

- Patient movement;
- Urine contamination;
- Prosthetic implants or other attenuating artefacts that may obscure normal structures, inducing photon-deficient areas;
- Homogeneously increased bony activity;
- Restraint artefacts caused by soft-tissue compression;
- Pubic lesions obscured by underlying bladder activity;
- Renal failure.

There are also several pitfalls that can originate misinterpretations of the image findings (38):

- Some aggressive or purely lytic metastases may not produce a visible osteoblastic response. Thus, they will appear as purely cold lesions, making more difficult their identification on a routine whole-body bone scintigraphy;
- If the bone scintigraphy is used for the assessment of treatment response but performed very soon after the treatment, it may be difficult to differentiate a flare response from tumour progression;
- When patients have undergone recent surgery such knee or hip replacements, bone scintigraphy may give false-positive results if performed too early. Thus, a later date for the examination can be considered. Otherwise, caution in the interpretation is required.

CHAPTER 3

Image Quality in Planar Scintigraphic Images

Image Quality in Planar Scintigraphic Images

Image quality can be defined by the capability of the system to detect relevant information, being related to the accuracy with which an image represents the imaged object. The quality of medical images depends on its information content and how accessible the information is, defined as its usefulness in determining an accurate diagnosis. As mentioned in the previous chapter of this document, there are several concepts used to describe imaging systems in terms of their quality of response, being referred as spatial resolution, contrast and noise. Those parameters are also recognized as the essential elements of image quality in nuclear medicine, being related to the diagnostic utility of the image (23, 28).

I. Image Quality Parameters

The correlation between image quality parameters and diagnostic performance has been discussed. However, it is known that extremely low physical parameters are not able to provide enough information for diagnosis by affecting diagnostic accuracy. In contrast, when image quality improves, diagnostic performance will also increase. Nevertheless, according to the International Commission on Radiation Units and Measurements (ICRU) report in 1986, beyond a certain level of image quality, the performance will saturate because no additional information is necessary anymore (**Figure 12**) (39).

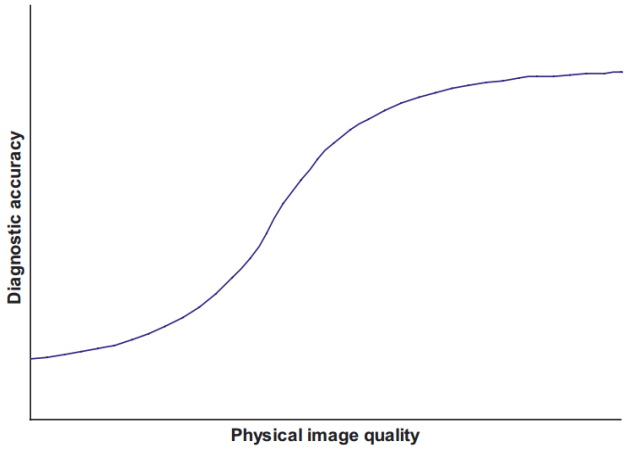

(39)

Figure 12 - Simplified quantitative correlation between physical image quality and diagnostic performance.

Despite the fact that image quality parameters describe singular aspects of an image, they cannot be treated as completely independent factors, because improving one of them may induce deterioration of one or more of the others (29).

1. Spatial Resolution

Spatial resolution is a property that describes the ability of an image system to accurately depict objects in the two or three spatial dimensions of an image. When comparing two imaging systems or techniques, determining the best spatial resolution means to find which modality is able to detect the smallest object. Nuclear medicine images have somewhat limited spatial resolution, at least when compared with radiological images. As mentioned in the previous chapter, a number of factors contribute to the lack of sharpness in these images (29, 40).

Technically, the spatial resolution of a digital image is regulated by two factors: the resolution of the imaging device itself and the size of the pixels used to represent the image in its digital format. Consequently, despite the higher amounts of noise, a smaller pixel size can exhibit more image detail. However, beyond a certain point there are resolution limitations related to the imaging device, allowing no further improvements on the acquired image (23).

The evaluation of spatial resolution can be performed either by subjective or objective means. A subjective evaluation involves visual inspection of the images. However, different observers may provide different interpretations, making the estimation of image quality difficult and subjected to inter-observer variability. One conceptual way of understanding and measuring the spatial resolution of a detector system in the spatial domain is to stimulate the detector with a single point source and then observe the way it responds (23, 29).

1.1. Point Spread Function

One method for describing the spatial resolution of a scintillation camera is the point spread function (PSF). The image produced by a detector system from a point source of activity is referred as the PSF. It contains complete information regarding spatial resolution, since it expresses the blurring properties of the imaging system by describing the imaging system response to a point input. Due to the imperfections of the imaging system, PSF is often modelled as a Gaussian function with a particular full width at half maximum (FWHM) (**Figure 13**) (29, 40).

The FWHM of the generated profile is used to characterize the collimator resolution and, consequently, a measure of spatial resolution. Because PSF's of different shapes can have the same FWHM, it only provides a partial specification of the spatial resolution characterization. However, the FWHM is considered as a useful parameter for general comparisons of imaging devices and techniques (23, 25).

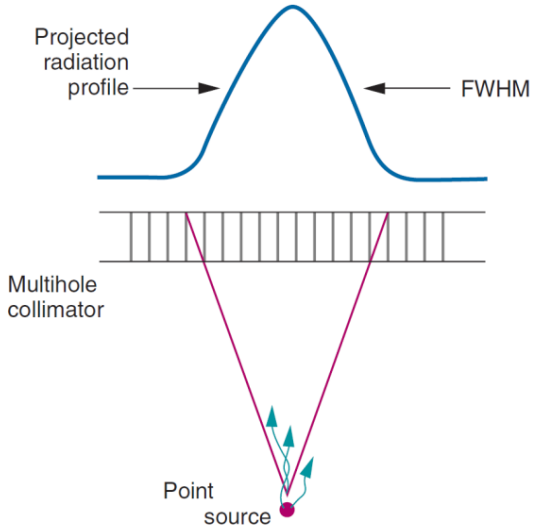

(29)

Figure 13 – Radiation profile (PSF) and relative FWHM for parallel-hole collimator.

The PSF expresses the performance of medical imaging devices in terms of sensitivity and spatial resolution by means of a function that describes the image when the object is a point. It describes how a photon originating at position y in the image plane ends up at position x in the focal plane. In general, the PSF varies independently with respect to both x and y, because the blur of a point source can depend on its location in the image (28, 41).

2. Signal-to-Noise Ratio

In order to visualize an object in a specific image, the object must have different brightness that its surroundings. Thus, the contrast of the object (signal) must overcome the image noise. The signal-to-noise ratio (SNR) is an expression used to describe the power ratio between the signal (significant information) and the background noise. In one imaging application view, these quantities would be a fixed known activity concentration and the standard deviation of its inherently fluctuating measured values attributable to the imaging protocol (**Figure 14**) (40, 42).

Considering that the mean describes what is being measured (x) and the standard deviation represents the amount of noise and other interferences, $\sigma(N)$, one can define the SNR as demonstrated on **Equation 1** (43).

$$\mathrm{SNR} = \frac{x}{\sigma(N)}$$

Eq. 1

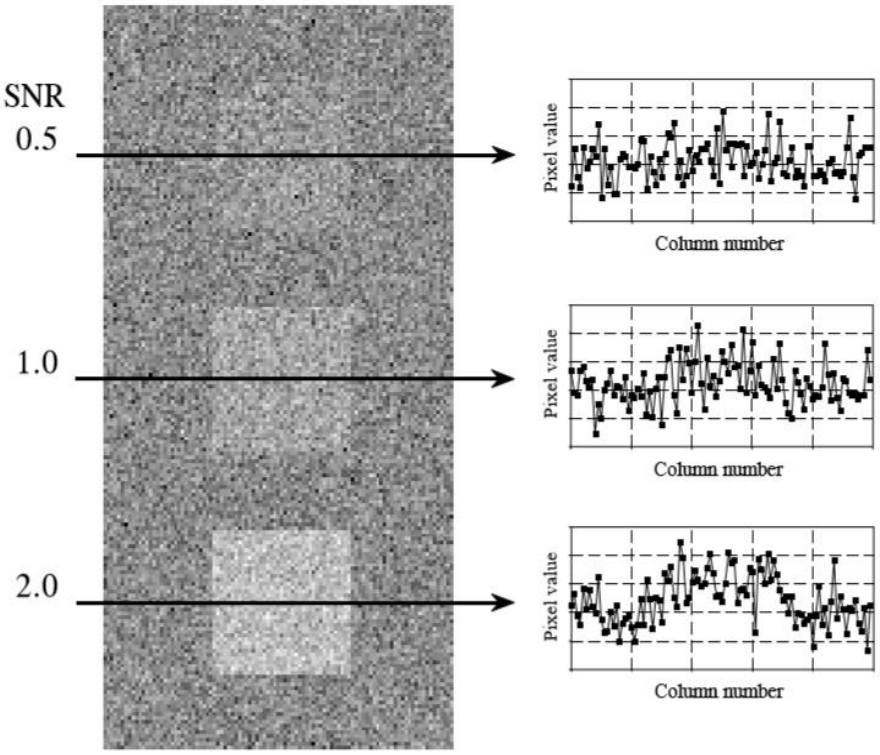

(40)

Figure 14 - Illustration of the minimum detectable SNR.
The object on the image will only turn visible when its contrast is large enough to overcome the random image noise. When SNR becomes lower than 1.0, the object depiction becomes more difficult.

3. Contrast-to-Noise Ratio

Image contrast can be described as the ratio of signal change of an object of interest, relative to the signal level in surrounding parts of the image. It is related to the intensity differences in areas of the image corresponding to different levels of radioactive uptake in the patient. In an absolute perspective, contrast (C) can be defined by the value of the difference between two grey values, as demonstrated on **Equation 2** (44).

$$\mathrm{C}(x_s, x_N) = |x_s - x_N| \qquad \textbf{Eq. 2}$$

Where x_s is the average gray scale on the object of interest and x_N that in the background, in which the noise can also be calculated (23).

In nuclear medicine, a major component of image contrast is determined by the properties of the radiopharmaceutical. Image contrast is also affected by the physical factors involved in image generation for being related to the statistical noise levels in the image, affecting the contrast-to-noise ratio (CNR) (29).

The CNR is an object size-dependent measure of the signal level in the presence of noise. It is a good method for describing the signal amplitude relative to the ambient noise in an image. CNR can be defined as shown in **Equation 3**. Since CNR is computed using the difference in mean values between two regions, is the most applicable metric to find where the mean grey scale in the signal region of interest (ROI) is representative of an object (23).

$$\mathrm{CNR} = \frac{x_S - x_N}{\sigma(N)}$$

Eq. 3

Where x_S is the average gray scale on the object of interest; x_N the average gray scale in the background; and $\sigma(N)$ the standard deviation in the background.

4. Other relevant quantitative parameters

4.1. Counts and Activity Concentration

In planar single photon imaging, the number of photons detected in a certain period of time is related to the established energy window for each pixel position. That number can be referred as the total counts or counts per second (cps). Moreover, this parameter can be calculated for a specific area in the image, or ROI. Count ratios for several ROIs can also be performed to access the differences in activity uptakes.

Activity is a measure related to the number of nuclear changes that occur per unit of time. It is referred through the unit Bequerel (Bq), which corresponds to one nuclear transformation per second. Alternatively, the activity in a source can be determined by using the activity concentration: MBq/mL (45).

4.2. Precision

Precision expresses the dispersion of a series of measurements around the mean. It is normally defined by the standard deviation (σ) and the coefficient of variation (COV). The COV measures the variability of a series of numbers independently of their unit of measurement, by dividing standard deviation by the mean. It is a useful measure when comparing the distribution of different series of numbers. COV can be expressed as a ratio, as demonstrated on **Equation 4**, or as a percentage whilst the result multiplied by a factor of 100 % (46).

$$\mathrm{COV} = \frac{\sigma}{mean}$$

Eq. 4

Given that the variance is proportional to the mean number of counts, COV will also be related to the sensitivity of the imaging system, the activity in the source and the acquisition duration (45).

At the same time, one can correlate this term with the SNR. For instance, a signal corresponding to a COV of 2 % has a SNR of 50. Thus, better data represent a higher value of SNR and, consequently, lower value for the COV (40)**.**

II. Factors Affecting Image Quality

1. Radioactive decay and natural background

For quantitative measurements it is important to be aware of the radioactive decay of the radionuclide. Given that the activity decreases as a function of time, one needs to decay correct the activity present at imaging time and the activity in the syringe measured in the dose calibrator for a certain calibration time. Background radiation is another factor that can influence the performance of quantitative measurements. It can arise from many different sources, including residual radioactivity, other patients in the neighbouring areas as well as natural radioactivity. If necessary, some corrective actions might be taken, such cleaning and using additional shielding (45).

2. Noise

Noise is related to the fluctuation that occurs in each pixel when receiving a certain number of photons from a particular source. It can be defined as the random change of the ideal pixel value during image acquisition. That is, pixel values are distorted from the ideal results by means of a random component. Any imaging system is considered a target of this type of occurrence (43, 44).

In nuclear medicine, noise is a consequence of the random nature of the radioactive decay process. This means that the atoms have the same probability of decay, independently of time. However, the probability of each atom to decay is independent of other atoms, being associated to the Poisson statistics. In practice, this will result in significant undesirable random fluctuations in pixel values that are superimposed on the ideal true values associated with objects being viewed (42).

The noise phenomenon is also related to the random nature of the detection process. Since detectors are characterized by random and independent probabilities, nuclear medicine imaging is ruled by counting statistics (or Poisson statistics) as well (45).

Images are subjected to noise and interference from several sources. It can be caused by the randomness in the radioactive process as well as by some features of image reconstruction. Consequently, it creates problems for the subsequent process of reading and interpreting such images. Noise effects can also be reduced by statistical filtering techniques or by a different approach, the application of noise cleaning techniques. Still, image noise reduction has remained a main problem in the image processing field. Noise can also be reduced by increasing the number of counts. Though, it would result in administration of higher activities or even use of longer counting times (**Figure 15**) (47, 48, 49).

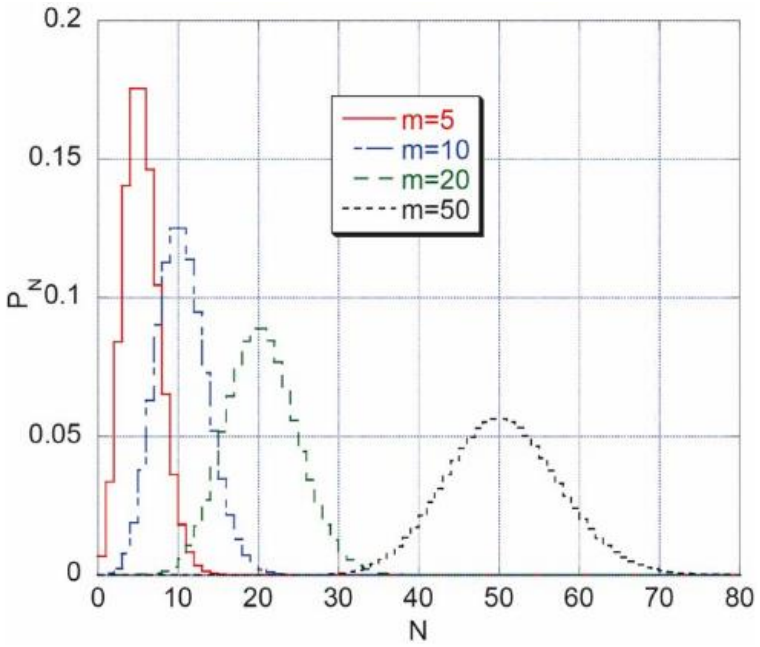

(45)

Figure 15 – Graph representing the Poisson probability (P_N) for different mean counts (m).

On a first approximation, one can write the acquired image in the form of **Equation 5** (43).

$$D(i) = U(i) + N(i) \qquad \textbf{Eq. 5}$$

Where $D(i)$ is the observed image, $U(i)$ would be the "true" value of pixel i, representing the unknown ideal (undistorted) image, and $N(i)$ the noise perturbation. The last parameter corresponds to small random pixel variations in the value superimposed on a true mean value from uptake signal (42, 43).

Due to its inherent random nature during the imaging process, it is impossible to reconstruct the ideal pixel values from the observed results. However, it is normally possible to predict the global effects of noise if some information regarding its statistical behaviour is available (44).

The main challenge during image reconstruction is the sensitivity to noise measurement in the input data, which can be strongly magnified, resulting in large artefacts in the reconstructed image. The answer to this difficulty is to restrict the permitted images. Progressively most sophisticated restrictions have been developed, imposing a variable degree of restriction across the image. However, the most consistent reconstruction method is considered the most conservative one, which restricts the permissible image modules (47).

Modern image reconstruction methods differ only in what they restrict and how they implement the restriction. The more restrictive the image reconstruction, the greater the stability, however, more likely will be to eliminate correct solutions. Thus, imposing the maximum, spatially adaptive smoothing allowed by the data results can be the best image reconstruction technique, in which the aim is to be as close as possible to the true underlying image. Accordingly, the goal is to describe the allowed solutions in a sufficient general way that includes all the possibilities, confining the results to the preferred images (47).

3. Partial volume effect

Partial volume effect occurs when a pixel includes different signals coming from different sources at the same time. This phenomenon is commonly due to the limited spatial resolution. This means that the signal emitted from a point source is not detected just on a single pixel, but also on the surroundings, resulting in large bias when estimating the regional radioactivity concentration through the imaging system (**Figure 16**) (45).

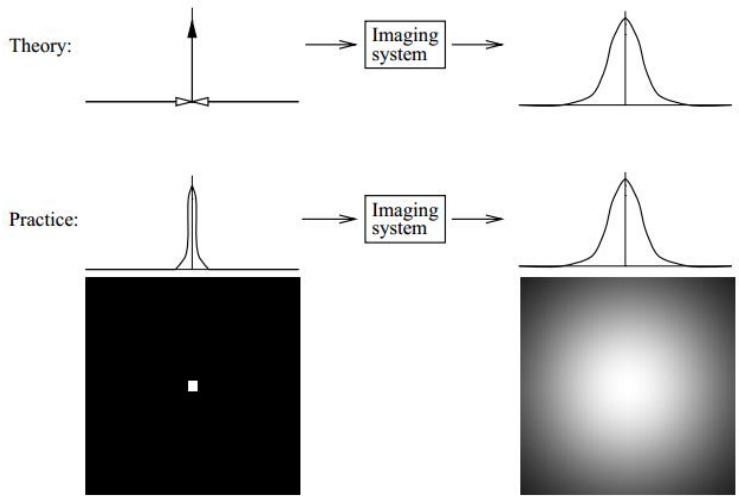

(44)

Figure 16 - Representation of the PSF on an imaging system. On the left it is demonstrated the function of this physical parameter, with the resultant PSF on the right.

In practice, this leads into undesirable effects through the signal profile regarding the estimation of true tracer concentration in the image. Such incidents can be referred as spill-out or spill-in, in which activities from structures close to the structure of interest induce an under- or overestimation, respectively, of the measured activity (**Figure 17**) (50).

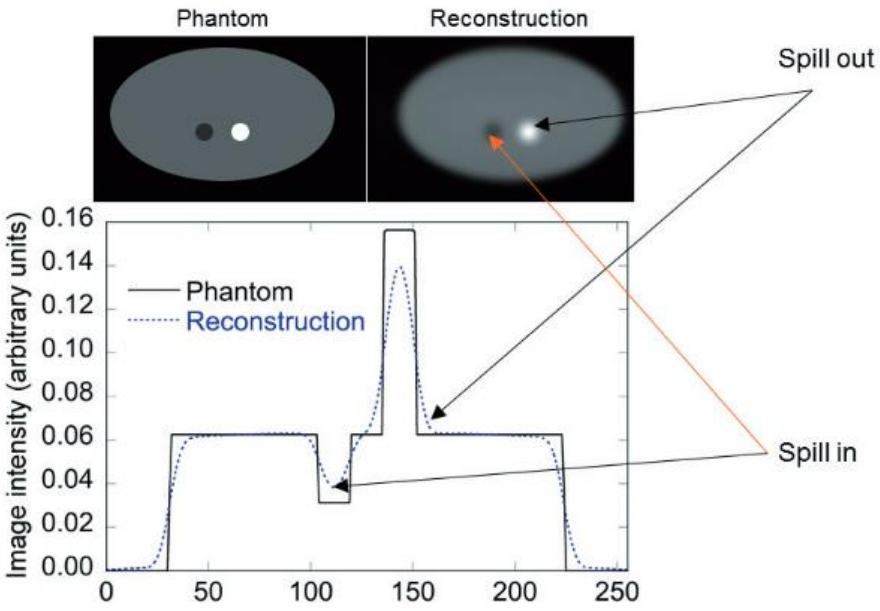

(45)

Figure 17 – Illustration of two partial volume effects: the spill out and spill in.
The first is an underestimation and the second an overestimation of the measured activity.

III. Image Reconstruction

The massive production of digital images has widely increased the need for efficient image reconstruction methods. Since images are often generated in poor conditions, an image improvement is always desirable. At the present, several advanced image processing techniques have been developed seeking the enhancement of digital images through reconstruction methods (43, 51).

Image reconstruction for data acquired with linear detectors often becomes a matter of inverting an integral relation on the form shown by **Equation 6**.

$$D(x) = \int dy\, H(x,y)\, I(y) + N(x) \qquad \textbf{Eq. 6}$$

Where:

$D(x)$ – Array of data points;

H – PSF;

I – Required underlying image model;

N – Noise.

In general, the imaging problem may be defined in a space with an arbitrary number of dimensions (x, y). If $H(x,y)$ is the PSF for a 2D imaging system and is symmetric about a central axis, the response of the system can be totally described by the curve $H(x)$ in an axial plane that intersects $H(x,y)$. The system sensitivity will be proportional to the volume under the surface $H(x,y)$. A perfect imaging system presents a point for each object point, meaning that the response is ideal (28).

There are two major problems when reconstructing images: noise fluctuation and overinterpretation of data. Image reconstruction differs from standard solutions of integral equations due to the noise term, N, whose nature is only statistically known. Moreover, noise fluctuations may be mistaken with real signal. Thus, specific methods for the reduction of random noise in planar images subject to noise statistics must be implemented (41, 52, 53).

IV. Assessment of Image Quality

Nuclear medicine images can be used either for detection tasks or quantitative tasks. Quantitative tasks normally require additional efforts compared with those applied in visual

interpretation. Nevertheless, quantitatively more accurate images will definitely result in improved performance on detection tasks. Some quantitative values that can be obtained from nuclear medicine images were described in the previous section (45).

In another perspective, image quality can be evaluated by two main different approaches, even when assessing image reconstruction algorithms. These methods are referred as subjective and objective assessments. They both aim to measure the performance of an algorithm in terms of image quality, for instance, depending on a specific diagnostic task (50).

1. Phantoms in Nuclear Medicine

According to the International Atomic Energy Agency (IAEA), phantoms have an essential role for evaluation of clinical medical imaging systems, given that it is possible to simulate with a considerable approximation the actual conditions under which these systems operate. However, it is important to be aware that a specific evaluation needs a suitable type of phantom (54).

1.1. Jaszczak SPECT Phantom

Information regarding this phantom is a courtesy of Data Spectrum Corporation website, the company responsible for the phantom design (55).

The Jaszczak SPECT phantom was designed by Data Spectrum Corporation (Hillsburough, N.C.) and approved by the American College of Radiology (ACR). It provides information regarding the performance of SPECT and PET imaging devices. It consists of a cylindrical container in which a set of different inserts can be planted (**Figure 18**).

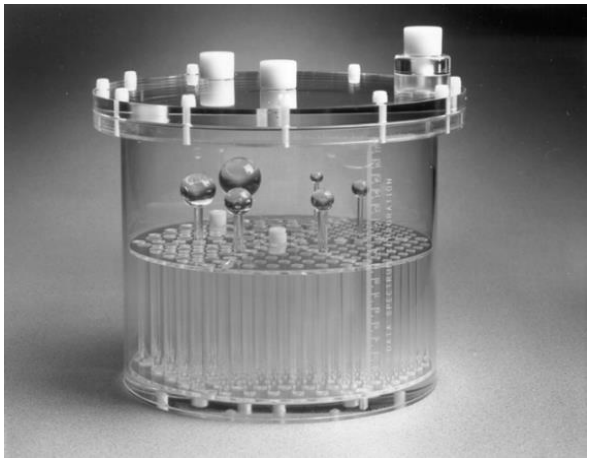

(55)

Figure 18 – Jaszczak SPECT phantom.

SPECT phantoms are available in four models, illustrated above, which are used for different system resolutions (**Figure 19** to **Figure 22**).

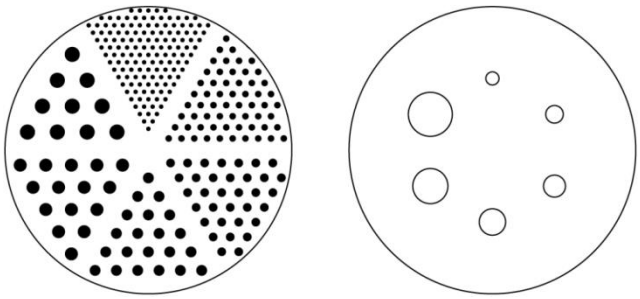

(55)

Figure 19 - Ultra Deluxe Jaszczak Phantom.
For use with ultra-high spatial resolution SPECT and PET systems.

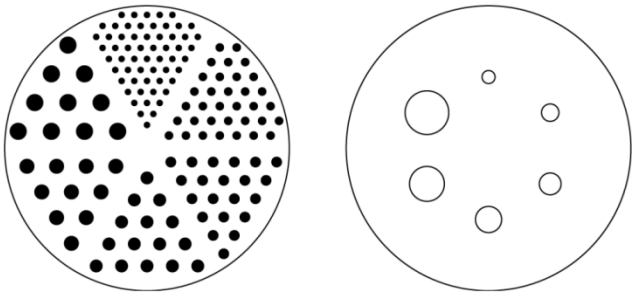

(55)

Figure 20 - Deluxe Jaszczak Phantom.
For use with high to very high spatial resolution SPECT and PET systems.

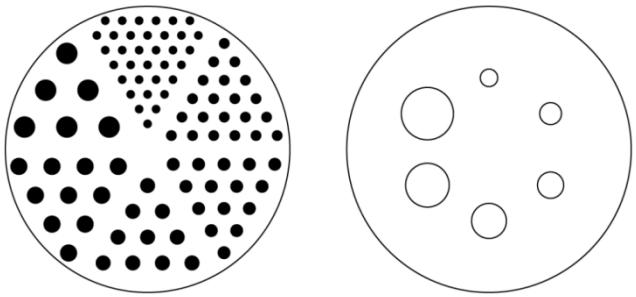

(55)

Figure 21 - Standard Jaszczak Phantom.
For use with medium to high spatial resolution SPECT and PET systems.

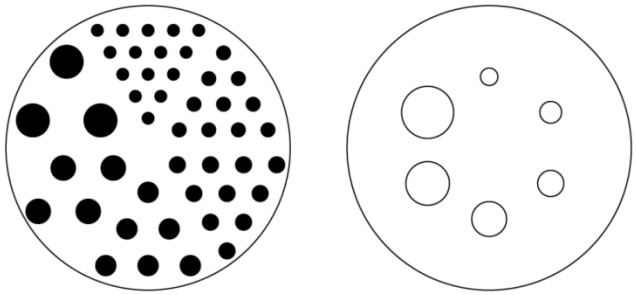

(55)

Figure 22 - Benchmark Jaszczak Phantom.
For use with poorer spatial resolution emission computed tomography (ECT) systems.

Main Applications:

- System performance evaluation of collimator, artefacts, calibration and reconstruction parameters;
- Acceptance testing;
- Routine quality control assurance;
- Evaluation of centre-of-rotation error and reconstruction filters on spatial resolution;
- Assessment of non-uniformity artefact, attenuation and scatter compensation;
- Single slice and total system volume sensitivity;
- Lesion detectability;
- Research.

Specifications:

Cylindrical container designed from clear acrylic (Polymethyl-Methacrylate) with 6.9 L volume (6.1 L with inserts) and a protruding flanged top. Precise specifications are provided in **Table 2**.

Table 2 - Cylinder specifications of the Jaszczak SPECT phantom.

Components	Dimension (mm)
Wall thickness	3.2
Inside diameter	180
Inside height	18.6
Length	300

The height of the centre of spheres from the base plate is 12.7 cm. However, the rod and cold sphere diameters vary with insert, dedicated for each model.

Accessory sets:

There are various accessory inserts available for Jaszczak SPECT phantom that can be very valuable, especially for research purposes. One important element in this category is the hollow sphere set (**Figure 23**).

(55)

Figure 23 - Hollow spheres set for circular and elliptical ECT phantoms.

Hollow sphere sets intend to simulate hot or cold spherical "lesions" for quantitative evaluation of spatial resolution or object size, attenuation and scatter effects. Specifications of this component are described in **Table 3**.

Table 3 - Hollow spheres outer and inner diameters (mm) with corresponding volume (mL).

Outer diameter (mm)	Inner diameter (mm)	Measured volume (mL)
11.89	9.89	0.5
14.43	12.43	1.0
17.69	15.43	2.0
21.79	19.79	4.0
26.82	24.82	8.0
33.27	31.27	16.0

1.2. NEMA IEC Body Phantom

Information regarding this phantom is a courtesy of Data Spectrum Corporation website, the company responsible for the phantom design (55); and the National Electrical Manufacturers Association (NEMA) Standards Publication No. NU 2 - NEMA, Washington, DC, 2001 (56).

The NEMA body phantom consists of a body phantom, a lung insert and an insert of hollow spheres with six different sizes (**Figure 24**). It was designed in accordance with the recommendations of the International Electrotechnical Commission (IEC) - 61676-1, Geneva, Switzerland, 1998; and modified by the NEMA.

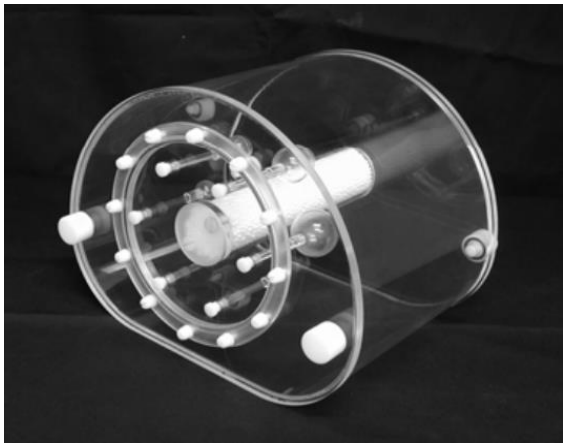

(55)

Figure 24 - NEMA IEC body phantom set.

Main Applications:

- Replication of whole-body imaging using PET and camera-based coincidence imaging techniques;
- Assessment of reconstructed image quality;
- Determination of the coincidence count rate performance for brain and cardiac imaging;
- Estimation of the correlation between true coincidence count rate and radioactivity;
- Evaluation of the count loss correction scheme;
- Research.

Specifications:

- Torso shaped container with 180 mm length;
- Volume of the empty cylinder: 9.7 L;
- Fillable spheres comprise the following inner diameters: 10 mm, 13 mm, 17 mm, 22 mm, 28 mm and 37 mm.

Image quality measurement:

The NEMA Standards Publication No. NU 2 provides fundamental guidelines for measuring the performance of PET imaging systems.

In order to quantify image quality using specific measures, several ROIs must be drawn on each sphere, with dimensions as close as possible to the physical inner diameters of the spheres. ROIs are also drawn through the background, at a distance of 15 mm from the edge of the phantom, but no closer than 15 mm to any sphere. Concentric to these 37 mm background ROIs, ROIs of smaller sizes shall be drawn (10, 13, 17, 22 and 28 mm). The locations of the ROIs must be fixed between successive measurements (**Figure 25**).

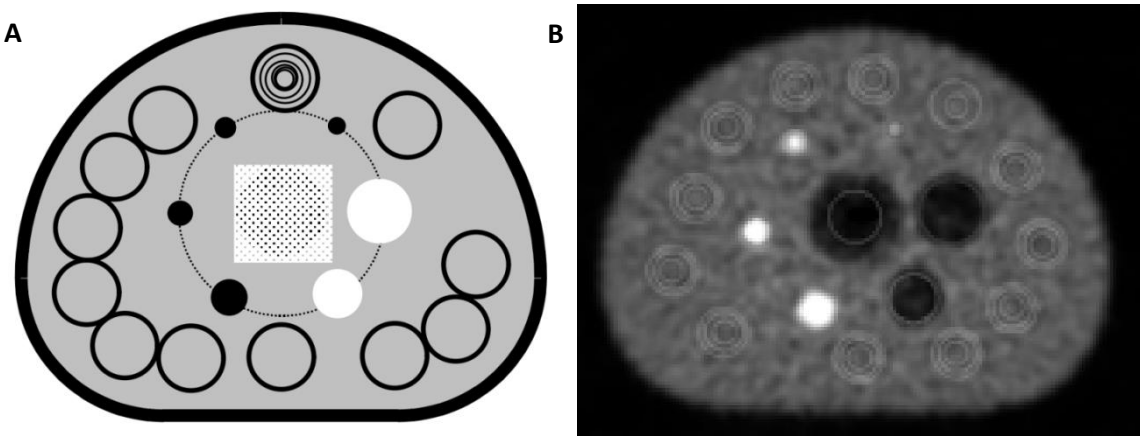

(56) (57)

Figure 25 - ROI mask for image quality analysis using the NEMA IEC body phantom.
A - Illustration according to the guidelines; B - Position of the mask on a true PET image.

Through this method, two significant image quality parameters are able to be calculated for each sphere:

- Percent contrast and
- Percent background variability.

The percent contrast or contrast recovery coefficient (CRC, %) is calculated as demonstrated on **Equation 7**.

$$\mathrm{CRC} = \frac{C_{sphere} \Big/ C_{bkgd} - 1}{A_{sphere} \Big/ A_{bkgd} - 1} \times 100\%$$

Eq. 7

Where:

$\mathrm{C_{sphere}}$ - Average counts in the ROI for the sphere;

$\mathrm{C_{bkgd}}$ - Average of the background ROI counts;

$\mathrm{A_{sphere}/A_{bkgd}}$ - Activity ratio between sphere and background.

The percent background variability (BV, %) translates the coefficient of variation of the means in the background ROIs for each sphere size (**Equation 8**). Thus, it is considered a measure of the variability in the background.

$$\mathrm{BV} = \frac{SD_{bkgd}}{C_{bkgd}} \times 100\%$$

Eq. 8

Where:

$\mathrm{SD_{bkgd}}$ - Standard deviation of the background ROI;

$\mathrm{C_{bkgd}}$ - Average of the background ROI counts.

CHAPTER 4

Reducing Scan Time in Whole-body Bone Scintigraphy

Reducing Scan Time in Whole-body Bone Scintigraphy

To generate an adequate diagnostic image in nuclear medicine, an appropriate balance between image quality and radiation dose is required. According to this, it is desirable to reduce radiation dose as well as the scanning time. For clinical practice it is important to obtain an accurate clinical diagnosis with collection of a minimum number of counts (7).

Since nuclear medicine images suffer from relatively high levels of noise and low SNR, noise reductions can be achieved by increasing radiation dose or image acquisition times or even by filtering the image with processing and post-processing techniques. Thus, some practical steps can be considered to improve diagnostic values in nuclear medicine diagnostic imaging (29, 52, 58, 59):

- Radiopharmaceutical dose: As mentioned above, an accurate diagnosis suggests using the minimum radiopharmaceutical dose, suitable for each procedure (particularly in the case of repetitive imaging). This means that reducing the administered radiopharmaceutical will generate images with decreased SNR. On the contrary, despite the fact that increasing the administered radioactivity increases the number of counts in the image, it could lead to higher radiation dose to patients;

- Pixel size: A digital image is one in which events are localized (or "binned") within a grid comprising a finite number of discrete picture elements referred as pixels. For a gamma camera, the detector area is divided into the desired number of pixels, where each pixel corresponds to a range of possible physical locations within the image (**Figure 26**). Digital images can be characterized by their matrix size, which is the number of pixels presented by the image matrix. This parameter affects the degree of spatial detail that can be presented, with larger matrices (smaller pixel size) providing more image detail. On the contrary, increasing pixel size could lead to noise reduction with increased SNR, but it would also induce reduced resolution due to the smaller amount of collected signal;

- Acquisition time: Extending the duration of the procedures increases the number of collected counts. However, this is not tolerated by many patients and this could also result in the appearance of motion artefacts since patients have tendency to move when experiencing discomfort, due to pain for example. In this field, there is always a compromise between image quality, workflow economics, patient safety and patient comfort;

- Reconstruction methods: An alternative option is to apply reconstruction techniques that allow increases in spatial resolution, enhancing the signal. However, this process is highly influenced by noise due to random measurement errors, which cannot be predicted. Thus, one needs to assume that they are random realizations of some parental statistical distribution in order to find a solution for the image model. Moreover, noise effects can be reduced by using appropriated techniques for statistical filtering.

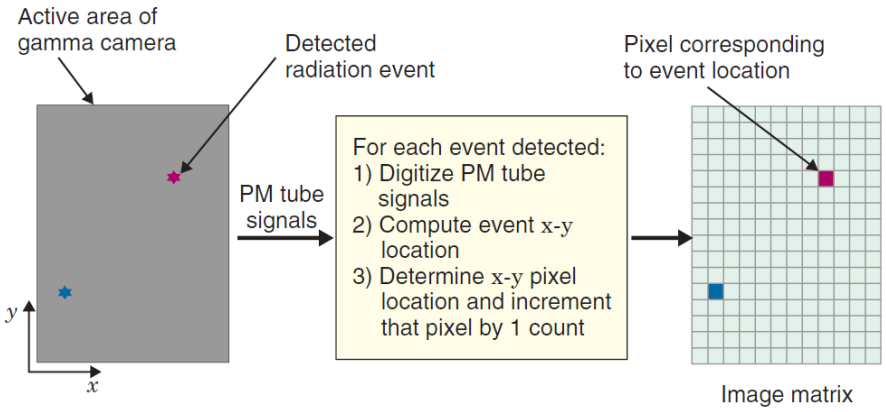

(29)

Figure 26 – Subdivision of the gamma camera detector area for generating a digital image.

I. Processing Scintigraphic Images

Digital image processing makes possible to reconstruct images acquired from non-ideal conditions, obtained from real-world instruments. As a result, information present but hidden in the data can be revealed with less blur and noise. This means that noisy images can have their quality improved, allowing images with a lower number of counts to be acquired (7, 41).

Presently, the pressure to reduce injected activities has reached new levels, making more rapid scanning desirable as well. Besides, due to their debilitating condition, patients submitted to whole-body bone scintigraphy can experience pain and anxiety during the examination. Because of the long scanning times in use for standard procedures (about 30 minutes) it is even more difficult to acquire images with sufficient image quality (7).

The reduction of acquisition time together with suitable image processing methods may be an appropriate method for noise reduction. Hence, the best technique must be found in order to increase confidence in the diagnosis of features observed in the image originally acquired with modified parameters (52).

Digital image processing is a robust means by which the underlying images hidden in blurry and noisy data can be revealed. It has been widely developed, providing high-quality reconstructions of unclear data collected by an extensive variety of sensors. Thus, it is mathematically possible to reconstruct the underlying image from non-ideal data collected from real-world mechanisms, so that the hidden information can be revealed with less blur and noise (41, 47).

The use of digital processing techniques can be used for image improvement, having many applications in space imagery and medical research. It involves operations that improve the quality of an image as perceived by a human or a machine, applying a broad set of algorithms and tools to repair, analyse, develop and visualize images. The need for implementation of image processing techniques will depend on the physical properties of the systems that describe their quality of response (28, 47).

II. Pixon Method

The Pixon method represents an innovative way of modelling an image in terms of its information content, allowing new competences in the fields of image reconstruction and data compression. As it offers versatile commercial software for a wide range of applications together with strong benefits to all kinds of imaging systems, the areas of medical imaging are not an exception (60).

Since image reconstruction is an important application in a number of fields, the Pixon method promotes medical images enhancement by (51):

- Improving sensitivity, reducing false negatives;
- Eliminating image artefacts, reducing false positives;
- The reduction of patients risks from ionizing radiation;
- Reducing effects due to patient motion by decreasing of image acquisition time;
- Reducing total cost of medical care.

The Pixon method is a high-performance image reconstruction technique that searches for the smoothest image statistically consistent with the raw counts. This concept was developed by Pina and Puetter in 1993 to restore astronomy images, with the purpose of eliminate problems with existing image reconstruction techniques, particularly signal-correlated residuals (**Figure 27**). The goal of this technique is to construct the simplest model for the image that is consistent with the data. As it is the simplest model, the derived image would be artefact free with no spurious sources. Consequently, Pixon method seeks for minimum complexity for the plausible model of the image, which enables an efficient

representation of the image as well as the best way to separate signal from noise. It has been applied to many fields, including medical image reconstruction (53, 61, 62, 63, 64).

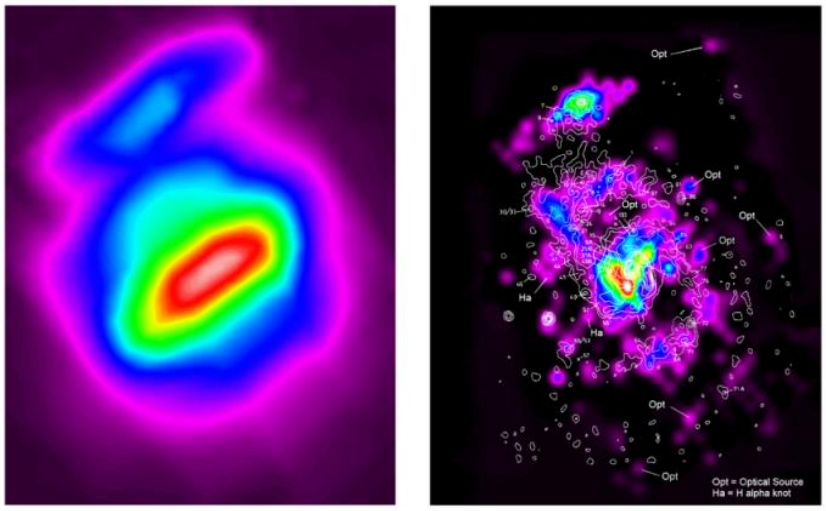

(60)

Figure 27 – Pixon reconstruction of a satellite survey scan.
The resolution of the reconstructed image (on the left) is 20 times finer than the raw scan (on the right). The sensitivity was improved by a factor of 100.

The Pixon concept is based on a nonlinear image reconstruction algorithm that increases linear spatial resolution by a factor of a few and sensitivity by an order of magnitude or more. Linear processing techniques are applied on images with continuous noise, however, they tend to provide too much smoothing. Despite the fact that they are more compact and less computationally demanding, they have poor noise propagation properties. In contrast, nonlinear techniques have been considered as the most successful modern methods of image reconstruction. This method is more complex, however, it often provides a better trade-off between noise smoothing and retention of fine image detail due to better control over the propagation of noise (47, 53, 65).

Pixon noise-reduction method provides statistically unbiased photometry, since it performs a robust rejection of spurious sources by using local information content, preserving statistically justifiable image features without generating artefacts. It can be applied on planar nuclear medicine images with known Poisson noise characteristics with the following goals: increase sensitivity for detection of lesions of decreased activity ratio; reduce acquisition time; or reduce patient dose (**Figure 28**) (52).

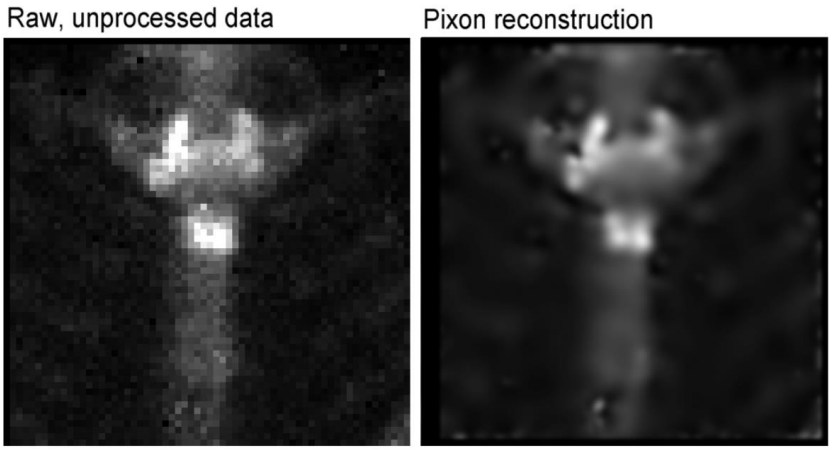

(60)

Figure 28 – Pixon reconstruction of a digital nuclear medicine planar image.
The raw image is significantly blurred with noise artefacts from photon counting statistics. On the contrary, the reconstructed image has improved resolution and reduced noise, enhancing the diagnostic capabilities.

Image processing with Pixon can be defined as a method based on a process of spatially adaptive, minimal complexity image reconstruction. It aims to strip away the inherent noise observed in low-count images, seeking the simplest underlying true image that can fit the collected data. The model is necessarily the most tightly constrained by the data, and consequently has the most accurately determined parameters. Since this method has minimum complexity, spurious sources are unlikely to occur (**Figure 29**) (7, 64).

(60)

Figure 29 – Performance of the Pixon method for the “Lena” image.

Instead of representing the images with pixels of a constant size, Pina and Puetter introduced an image model where the size of the pixels varies locally according to the

information density in the image, generally referred as pixons or degrees-of-freedom. Each pixon represents a degree of freedom that is determined using a larger fraction of the data and so is determined more accurately. A map of the pixon sizes is called an image model (**Figure 30**). With this, the Pixon method aims to find the best match between the image and its image model that is consistent with the data and can represent the structure in the image by the smallest number of pixons. This generally results in superior photometric and positional accuracy and, since the minimum number of parameters is used, the data cannot be over-fitted (64, 66).

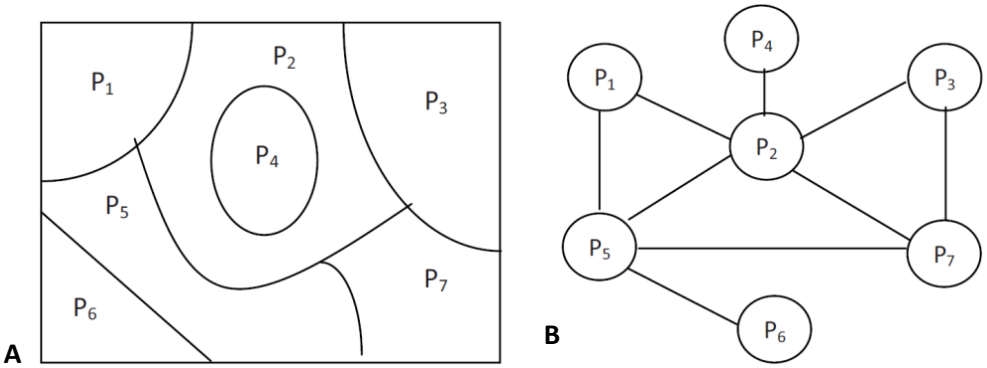

(61)

Figure 30 – Pictorial example of a Pixon map.
A - Image model of the Pixon map; B - Correspondent graph structure.

According to the basis of Pixon-based method, images can be briefly described using a reduced amount of degrees-of-freedom where the image characteristics are smooth, and using more degrees-of-freedom where greater detail is present. Clearly, if the signal in the image can be adequately represented by a minimum number of parameters, adding another parameter will only introduce artefacts by fitting the noise. On the other hand, removing parameters results in an inaccurate representation of the image. Since the Pixon definition scheme should yield an optimum scale description of the observed image, the ability to control the number of degrees of freedom used to model the images is the key aspect (53, 61, 62).

The procedure to determine the set of pixon elements, specifically their shape and size, includes obtaining a pseudo image. The pseudo image is a basic representation derived from the observed image that has at least the same resolution as the original image. With this, the image model is made up contiguous and nonoverlapping cells, regarded as pixons, having constant intensity within each pixon (**Figure 31**) (61, 67).

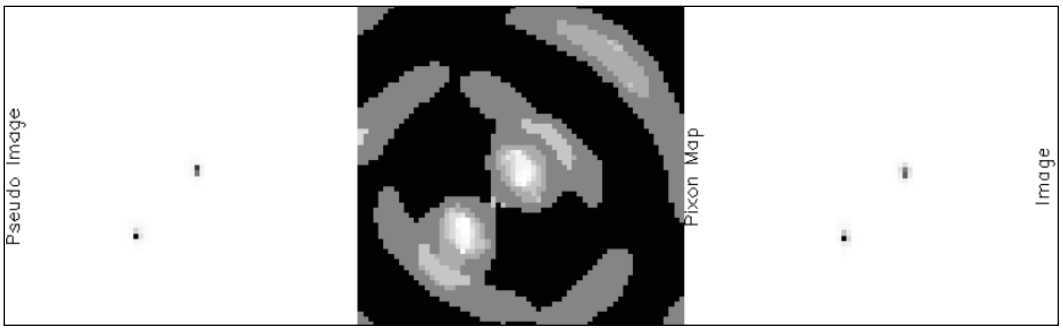

(68)

Figure 31 – Pseudo image and its correspondent Pixon map with the resulting reconstructed image. The Pixon map shows the spatial scale applied at each pixel, which represents where the information is concentrated.

In order to minimize complexity, the Pixon method smoothes the image model locally as much as possible, reducing the number of independent patches, the Pixon elements. The dimensions of the pixons define locally the scale of underlying image information. In fact, those elements describe directly the "natural graininess" of the information in a data set due to the statistical uncertainties in the measurements (53, 62, 69).

The description of an image's set of pixons is highly idealistic. As a consequence, Pina and Puetter introduced two practical Pixon bases. The first scheme proposed was named Uniform Pixon Basis (UPB) in which the algorithm complexity for each pixon is equal. The second scheme was called the Fractal Pixon Basis (FPB) and analyses the algorithm complexity of the image in terms of a single spatial scale, being referred as "fuzzy-pixon", which is a correlation approach where adjacent pixons share some of each other's signal instead of having hard boundaries. In this approach, the independence of the different parts of the image is reduced through explicit spatial correlation, assuming an intrinsic correlation length that can vary across the image. Reconstructions using the FPB approach can be mentioned as the standard Pixon method. The reconstructed images have no signal-correlated residuals and are effectively artefact (false-source) free (**Figure 32**) (66, 70, 71).

Formally, the image is written as an integral over a pseudo image as demonstrated on **Equation 9** (70).

$$D(x) = \left(H * \left(K \otimes I_{pseudo}\right)\right)(x) + N(x)$$

Eq. 9

Where:

$D(x)$ – Array of data points;

H – PSF;

K – Blurring function;

I_{pseudo} – Pseudo image;

N – Noise in the data;

$*$ – Normal convolution operator;

$\otimes$ – Local convolution or smoothing operator.

And I_{pseudo} is defined such that the normal image can be: $I(x) = \left(K \otimes I_{pseudo}\right)(x)$.

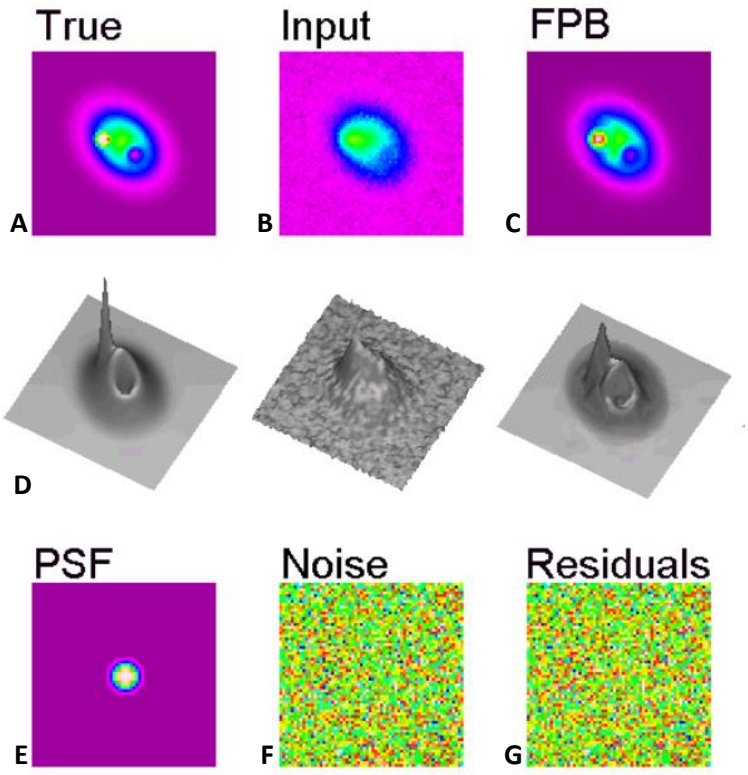

(60)

Figure 32 – Pixon image reconstruction (FPB) for a synthetic data set for which the true (unblurred) image, the blurring function (PSF) and the input noise are known a priori.
A - True image; B - Blurred and noised input data; C - Pixon reconstruction; D - Surface plots of the top row images; E – PSF; F - Input noise; G - Residuals for the Pixon reconstruction.

The operator K transforms the underlying field to data space. The PSF is the factor that typically blurs the image due to instrumental and possibly atmospheric blurring. To solve **Equation 9**, it is assumed that the functional form of the PSF is known, although it may have unknown parameters which need to be determined from the data. Moreover, the noise is taken to be sufficiently well understood since its nature is only statistically known (53, 67).

The goal of Pixon image reconstruction is to find the smoothest possible image by selecting the broadest possible nonnegative, spatially variable kernel K, for which a nonnegative pseudo image I_{pseudo} can be found. As a result, the Pixon method starts with a finely sampled positive pseudo image and smoothes it with a positive kernel function to obtain the image. Thus, the method proceeds alternatively between determining I_{pseudo} and K, starting with the determination of I_{pseudo} with some initial K. Furthermore, the normal image is replaced by a pseudo image smoothed locally by a function with position dependent scale. The $\left(K \otimes I_{pseudo}\right)$ operator can then be referred as the sought underlying image model (41, 67, 70).

Thus, the Pixon reconstruction combines the search for the broadest possible kernel functions together with their pseudo image values that provide an adequate fit to the data, depending on the essence of the Pixon method applied (**Figure 33**) (67).

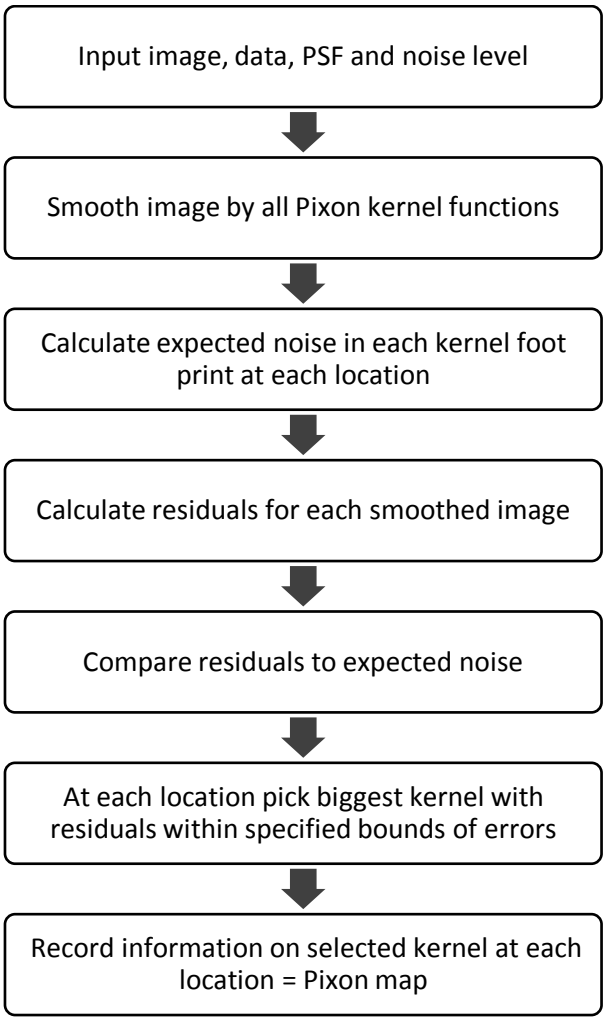

(72)

Figure 33 – Block diagram of the steps of image reconstruction with Pixon map calculation.

Alternatively, the pseudo image can be solved with a given Pixon map of kernel functions and then attempt to increase the scale sizes of the kernel functions given the current image values. The required number of iterations depends on the complexity of the image, but for most problems a couple iterations is sufficient (**Figure 34**) (67).

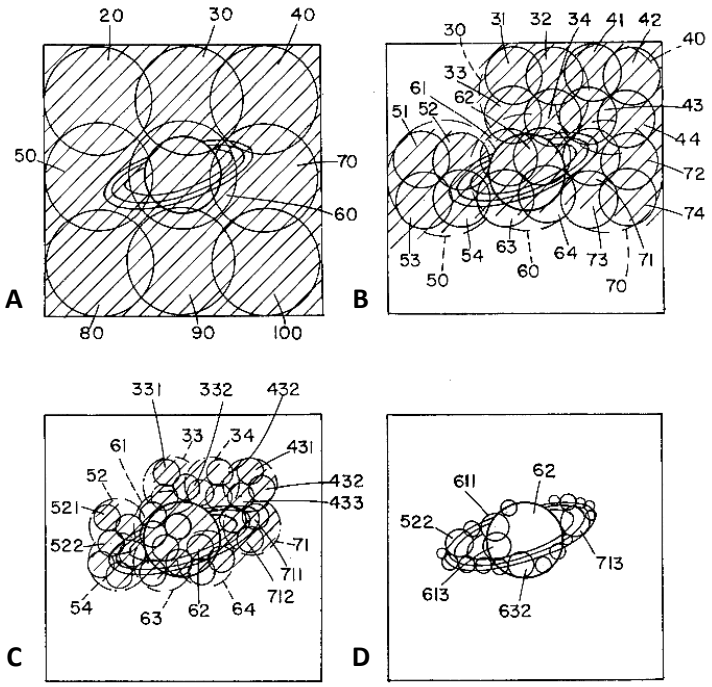

(72)

Figure 34 – Simulated image reconstruction sequence using a multi-resolution decomposition of the image model.
A - Noisy input data with a first iteration Pixon map; B - Second iteration with new smaller scales kernels; C- Third iteration Pixon map; D - Final Pixon map.

When the SNR is not too low, a Pixon reconstruction proceeds reasonably well, however, for lower SNR more elaborated methods are needed. In the case of gamma rays experimental tests with lower SNR, the derivation of the Pixon map requires mean field annealing which is a deterministic approximation for solving optimization problems, at higher computational cost. Efforts have been made to develop faster and more general techniques. This progress has already been achieved with the creation of a “black box” software which does not require fine adjustments by the user. Nowadays, this technology has been integrated in medical imaging systems and is available commercially for post-acquisition processing, but there are remaining uncertainties regarding diagnostic agreement that make its employment not widely accepted (7, 67).

CHAPTER 5

Enhanced Planar Processing Algorithm: A Phantom Study

I. Purpose of the Study

Images obtained in nuclear medicine procedures can have high levels of noise, resulting in interpretation difficulties. Improvements in image quality can be achieved by increasing the collected counts (by lengthening image acquisition time or increasing the amount of radiotracer administered to the patient) or by filtering the image. Image filtering through the application of image processing tools is often employed, increasing the confidence in the diagnosis.

The purpose of this work is to access the performance of an Enhanced Planar Processing (EPP) algorithm based on the Pixon method, by means of a phantom study. This application was developed for planar nuclear images with known Poisson noise characteristics, being included in a software package developed by Siemens (Siemens Medical Solutions, USA).

Recently, such software package became available at the department of Radiology and Nuclear Medicine of the Radboud University Medical Centre, in the Netherlands. According to Siemens, this technology enables reconstruction of low count planar images with comparable quality when compared to images acquired using standard protocols. However, there are remaining uncertainties whether EPP affects patient diagnosis on planar images and eventually management of patients.

Since pain can be a major drawback for patients with metastatic bone disease when performing bone scintigraphy procedures, it would be desirable to take advantage of the referred processing tool in order to reduce the scan duration, while maintaining the same diagnostic quality of the examinations.

Thus, the aim of this study is to assess the performance of the EPP algorithm, when compared to the standard protocol. Lesion detection and image quality are the parameters on focus. Before being applied to clinical practice, it is important to characterize this software using standardized experiments, including phantom research. The ultimate goal will be to warrant the safe employment of the software in the referred department, aiming the improvement of patient care and workflow.

II. Materials and Methods

The present study was performed at the Department of Radiology and Nuclear Medicine in the Radboud University Nijmegen Medical Centre in the Netherlands, a leading institution for medical research and education. This department provides advanced radionuclide imaging and therapy with radiolabeled tracers, being equipped with four gamma cameras and one PET-CT scanner.

The study was developed from April to October 2014. The timeline of the investigation is presented in **Table 4**.

Table 4 - Timeline of the investigation.

Task \ *Month*	2014						
	April	**May**	**June**	**July**	**Aug.**	**Sep.**	**Oct.**
Literature Review							
Development of the investigation project							
Data collection							
Data analysis							
Presentation of the results							
Elaboration of the thesis							

The development of the investigation process is explained in **Figure 35**. Through the presented diagram one can perceive the details of the main stages of the investigation until the accomplishment of the results and conclusions. The main stages include methodology of the study, data collection and data analysis.

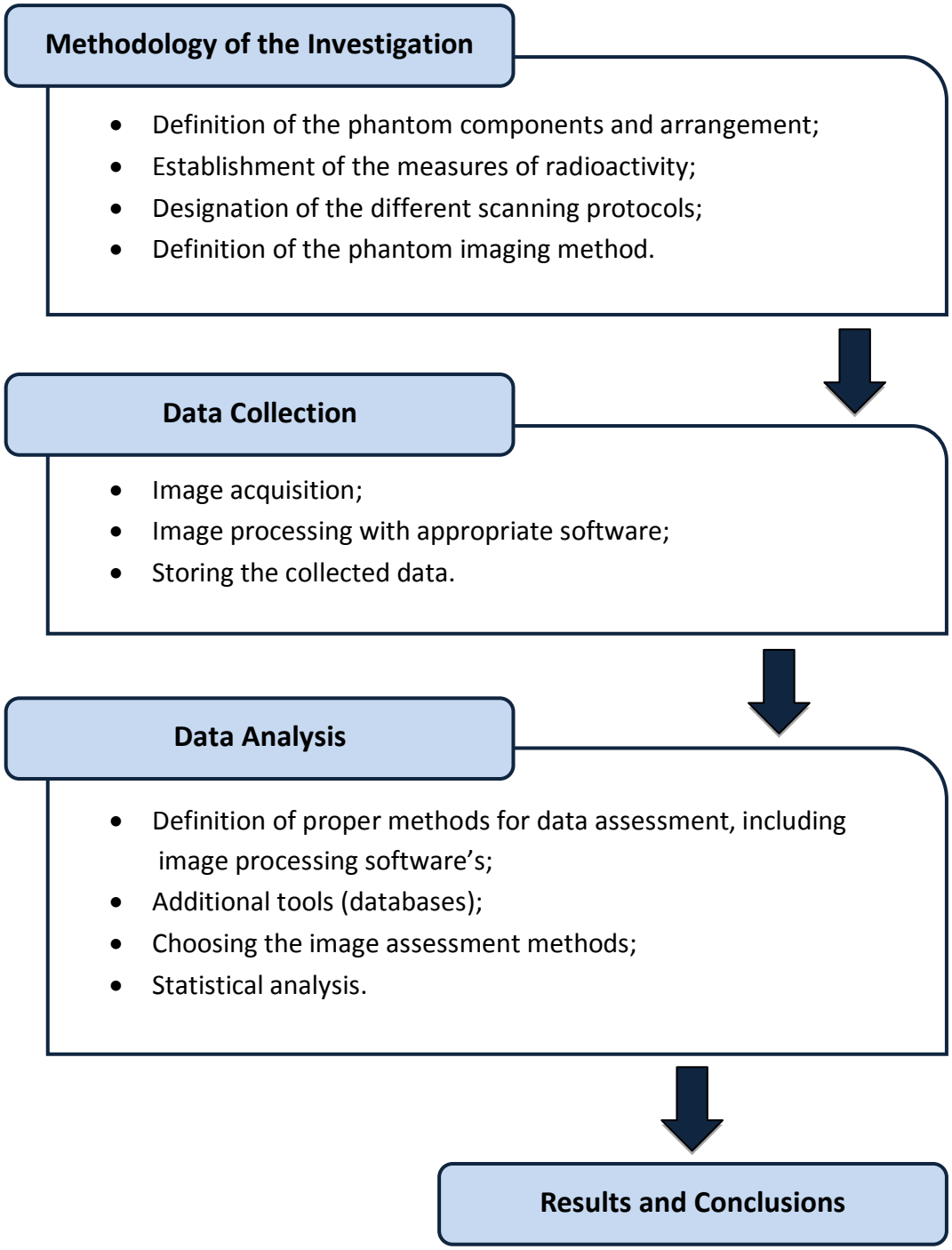

Figure 35 – Diagram of the investigation stages.

1. Phantom

All images were acquired using a SPECT cylinder phantom (Jaszczak phantom, Data Spectrum Corporation). For this study, the cylinder was filled with a ^{99m}Tc water solution. Additionally, the hollow spheres were considered with the purpose of simulating "hot" spherical lesions.

Considering that it was desirable not just to have a short distance between the spheres and the detector (object-to-source distance) but also to avoid unnecessary superimposed structures during planar imaging, a different configuration for the phantom was defined, since the lids on the top would appear as a likely source of data bias (23).

The new arrangement was defined by adopting a different set of hollow spheres: an insert with six spheres with various sizes from the NEMA phantom. The inner diameter of the insert is 11.44 cm. The inner diameters of the spheres are: 10 mm, 13 mm, 17 mm, 22 mm, 28 mm, and 37 mm. The wall thickness of the spheres is approximately 1mm, with polymethylmethacrylate as constituent material (**Figure 36 (A)**).

To facilitate the introduction of the hollow spheres insert in the phantom, a "cold" cylinder with 12 cm height and 5 cm diameter was used. The diameter of the chosen cylinder was lager enough to sustain the mounting plate of the insert, but had also reasonable distance to each element (3.2 cm to the largest sphere) so that no interference from this object could take place during image acquisition (**Figure 36 (B)(C)**).

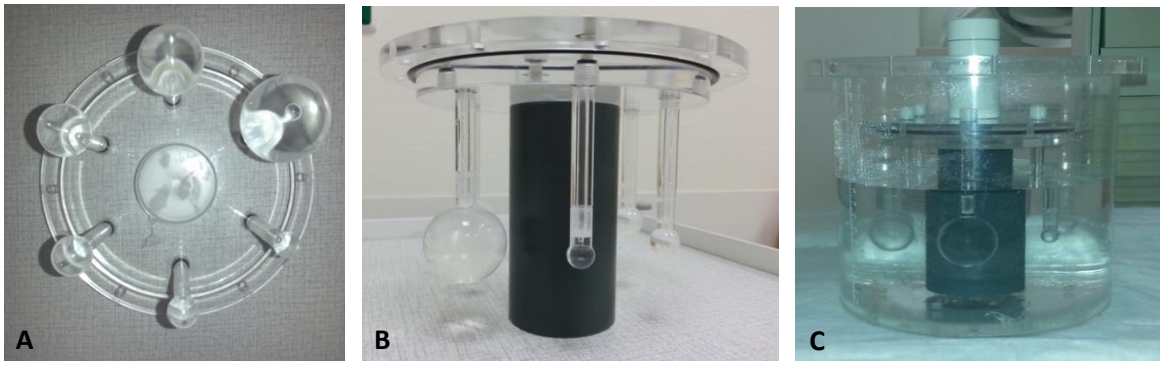

Figure 36 - Hollow spheres insert of the NEMA phantom.
A – Insert with hollow spheres of six different sizes; B - Insert placed in the cylinder support;
C – Insert placed inside the phantom.

2. Scanning Plan and Phantom Filling

In order to fully assess the performance of the EPP algorithm, the phantom was scanned using different scan speeds with different sphere-to-background activity ratios in the spheres (52).

The scan speeds were then defined based on the standard protocol used at this department, with 8 cm per minute scan speed, and were determined as demonstrated on **Figure 37** (37).

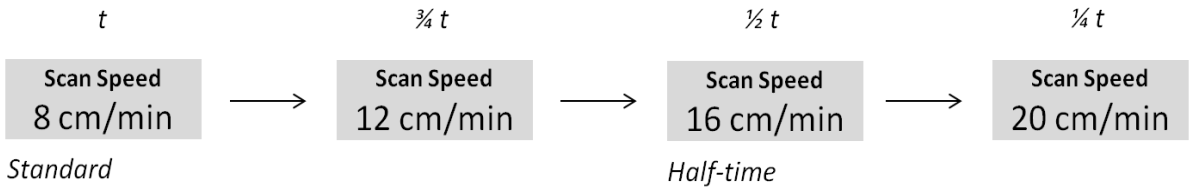

Figure 37 - Definition of the scan speeds according to the standard protocol.

Being t the time of the scan duration for the standard protocol, the subsequent speed scans were selected in order to obtain decreased scan durations according to the following order: $3/4\ t$; $1/2\ t$; and $1/4\ t$. These parameters correspond, respectively, to a scan speed of: 12 cm/min; 16 cm/min; and 20 cm/min.

2.1. Filling up the background

Given that the configuration of the phantom was modified, no standard or pre-established values concerning the supposed background volume were known. Thus, by means of an experimental test approach, that volume was estimated.

Considering that the phantom is supposed to be scanned as illustrated in **Figure 38**, and also that the height of the centre of spheres from the base plate is 5 cm, the cylinder should be filled with twice of that height in order to create an uniform environment in the neighbourhood of the spheres. Thus, given that the phantom must be filled with a solution depth of 10 cm, it resulted in a total volume of 3.28 L, where the displacement of the spheres, its supporting rods and cylinder were taken into account.

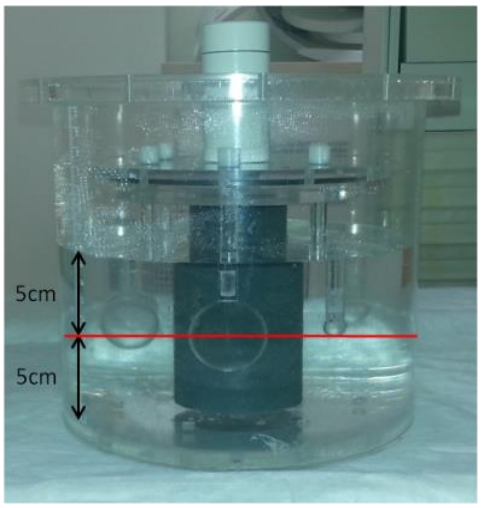

Figure 38 - Illustration of the measurements performed for the calculation of the solution volume in the background.

Since it is quite complex to establish an average count rate for the different patients in the bone at the time of the scan due to the individual physiological processes and clinical conditions, the adopted methodology for choosing the activity for the background was based on the average count rate found in the soft tissue. This value could be more representative and comparable when trying to simulate the conditions in real patients due to the high blood clearance of the radiopharmaceutical: three hours after injection only 3 % of the administered activity remains in the bloodstream. Besides, bone lesions are often located adjacent to soft tissue (33).

With the intention of finding an average value for the count rate in the soft tissue at the time of the scan, 20 patients submitted to whole-body bone scintigraphy were selected. The patients were only included after being kindly requested to provide their data for investigation purposes. All these individuals had an incubation time of 4 hours with no lesions recorded in the anatomical region selected for this estimation. The average age of the patients was 64.7 years old.

The count rate measurements were performed in the soft tissue of the right inner thigh, for being considered a representative region since it is the largest area of the body including soft tissue without overlapping of bones. Rectangular ROIs were drawn, with dimensions of approximately 23x3.5 cm (**Figure 39**) (73).

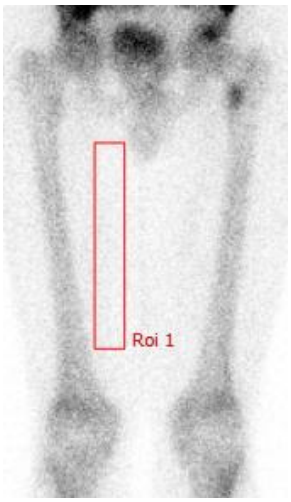

Figure 39 - Section of a whole-body bone scintigraphy illustrating the method used for the ROIs drawing.

With these measurements, it was possible to set up an average count rate with a value of 5.43 counts per second, with a standard deviation of 2.53 (**Table 5**).

Table 5 - Average results of the count rate (cps) measurements. Series acquired in 20 patients submitted to whole-body bone scintigraphy. Incubation time of 4 hours.

Count Rate (cps)				
Mean	**Minimum**	**Maximum**	**Median**	**Standard Deviation**
5.43	0.15	16.1	5.6	2.53

In order to find the amount of activity correspondent to the determined count rate, some experimental tests were performed. The cylinder of the phantom was filled with a volume of 3.28 L containing a water solution and ^{99m}Tc- hydroxymethylene diphosphonate (^{99m}Tc-HDP), with different activity concentrations. The acquisition parameters were the same as the standard whole-body bone scintigraphy protocol (explained further on this chapter). Subsequently, a ROI was drawn in each acquired image in order to observe the achieved count rate.

Two experimental tests were performed: the first with a lower (0.6 MBq) and the second with a higher (2.5 MBq) amount of activity of ^{99m}Tc (**Figure 40**). The radioactive material was mixed thoroughly by several shaking for about 10 minutes. This process was performed by the same person each time, an experienced nuclear medicine technologist.

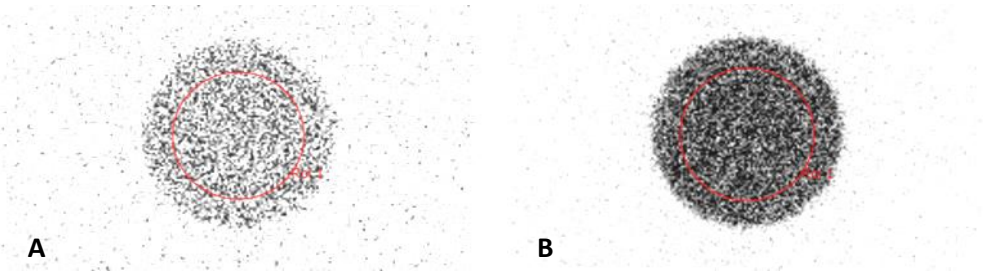

Figure 40 - Images acquired after imaging the phantom cylinder with two different activity concentrations.
A - Total amount of activity of 0.6 MBq; B - Total amount of activity of 2.5 MBq.

The first experimental test revealed an average count rate of 1.25 and the second 4.85 counts per second (**Table 6**).

Table 6 - Results from the measurements performed with ROIs drawn on the acquired images. It includes the total number of counts, mean (count rate), minimum and maximum values, median and deviation. The first experimental test reveals a count rate of 1.25 while the second experimental test resulted in a count rate of 4.85.

Count Rate (cps)					
Experimental test	**Mean**	**Minimum**	**Maximum**	**Median**	**Standard Deviation**
1	1.25	0.00	6.00	1.00	1.13
2	4.85	0.00	14.00	5.00	2.21

Because the last experimental test revealed a count rate extremely close to 5, it was decided that the phantom should be filled with water containing approximately 2.5 MBq of ^{99m}Tc-HDP in the following experimental tests.

2.2. Filling up the spheres

The spheres were filled with different sphere-to-background activity ratios in order to understand the effect of the EPP algorithm across a range of circumstances. Considering 0.762 MBq/L the activity concentration in the background, the planned activity contrast ratios between the concentration in the background and the spheres were then: 4:1, 8:1, 16:1, 24:1, 32:1 and 64:1.

The filling of the spheres was performed using a stock solution of 1 L of water with the estimated amount of radioactivity, so that all the spheres could have exactly the same activity concentration during each experimental test (**Table 7**).

Table 7 - Description of the total activities estimated for the stock solution with 1 L of water for each sphere-to-background activity ratio.

Ratio	Activity (MBq)
4:1	3.048
8:1	6.096
1:16	12.192
1:24	18.288
32:1	24.384
1:64	48.768

For this process, the radioactive material was also mixed thoroughly by several shaking for about 10 minutes. This procedure was performed by the same person each time, an experienced nuclear medicine technologist (**Figure 41**).

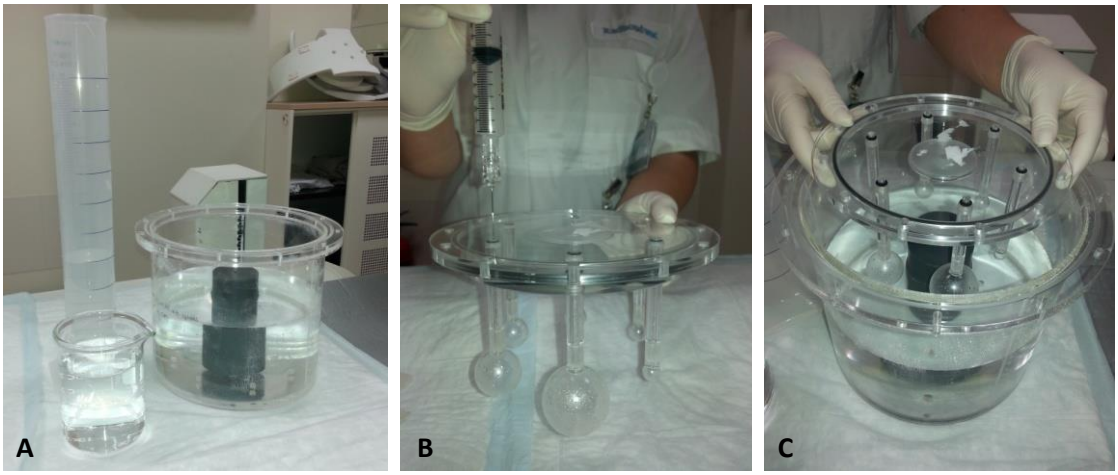

Figure 41 - Method used to fill in the spheres.
A - Production of the stock solution; B - Filling the spheres with a syringe with a long needle; C - Introduction of the spheres set in the phantom.

3. Image Acquisition and Processing

The gamma camera used in this study was the e.cam Signature Dual Detector System (Siemens Medical Solution USA, Inc.), after daily calibration.

After each experimental test, the four acquired series were processed using the whole-body EPP tool, available in the Siemens software package (Siemens Medical Solutions, USA) existing at the department.

3.1. Phantom positioning

The flat surface of the cylinder was positioned on the middle axis of the gamma camera imaging table, with the detector heads in anterior and posterior position (**Figure 42**). The spheres set was carefully positioned inside the cylinder using the same technique each time, in which the largest sphere was required to be aligned with the mid-horizontal long axis of the imaging table. Bed positioning was permanently set for the standard height (13 cm). The phantom positioning and camera manipulation were performed by the same professional during all the experimental tests.

Figure 42 - Demonstration of the phantom positioning in the gamma camera imaging table.

3.2. Acquisition Parameters and Processing Algorithm

The data was acquired with the same camera parameters used for the standard whole-body bone scintigraphy, with a 256x1024 matrix and acquired using low energy high resolution (LEHR) collimators (**Figure 43**).

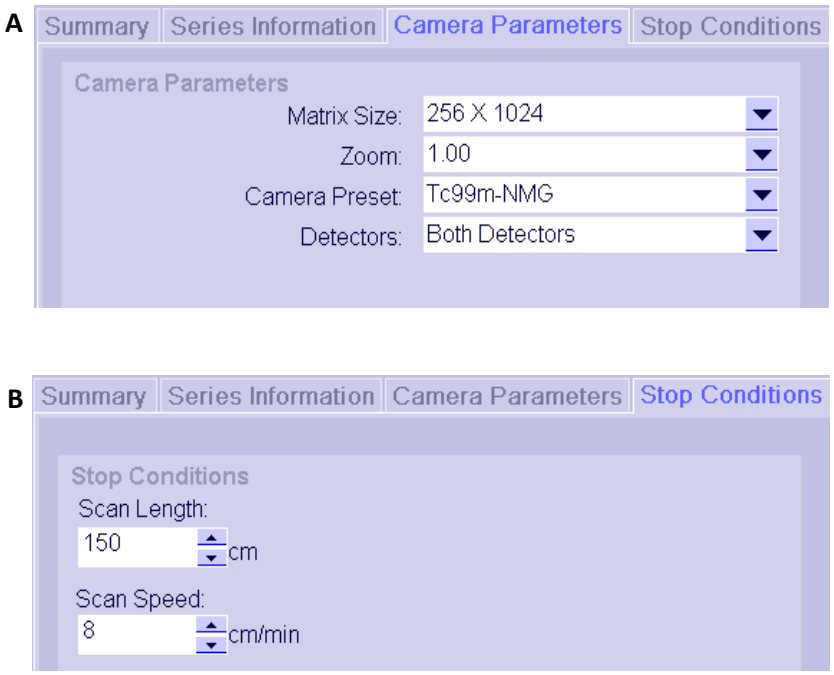

Figure 43 - Acquisition parameters used in the standard whole-body bone scintigraphy protocol. A - Camera parameters; B - Stop conditions.

Experimental tests with six different radioactive concentrations in the spheres were performed. For each experimental test the phantom was imaged four times using fixed acquisition parameters. The only difference in the acquisition was the scan speed: 8 cm/min, 12 cm/min, 16 cm/min and 20 cm/min. A total number of 24 acquired series were included in the study after the completion of the six experimental tests.

With the intention of reducing the effects of radioactivity decay within each experimental test, the scans were performed from the fastest to the slowest protocol as it comes: 20 cm/min, 16 cm/min, 12 cm/min and then 8 cm/min.

Despite the fact that both detectors were selected during image acquisition, only images acquired with detector 2 (posterior view) were used for this purpose due to the appropriate characteristics in relation with the established phantom arrangement. The distance of the detector 2 was constantly set for 14.6 cm.

The parameters for the processing algorithm were kept fixed for all reconstructions, being the reconstruction process set in the automatic mode (**Figure 44**).

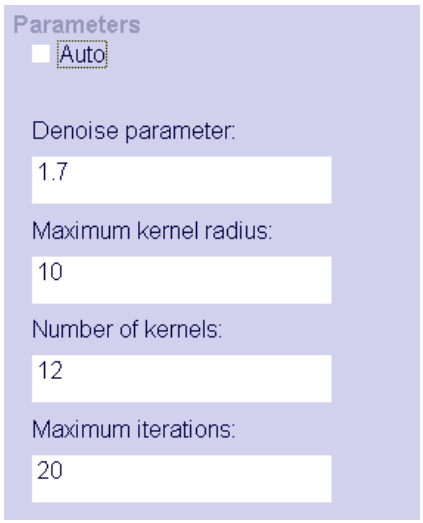

Figure 44 – Reconstruction parameters applied in the whole-body EPP tool. Siemens software (Siemens Medical Solutions, USA).

4. Storing the Collected Data

All the processed and unprocessed series were stored in a specific database created on HERMES version 4.6-A (HERMES Medical Solutions - Stockholm, Sweden). HERMES (Nuclear Diagnostics) is a software package used at the department for processing, archiving and distribution of medical images.

Anonymous data was used with the intention of performing a blind analysis of the images afterward, so that readers could be blinded to image details, including the percentage of counts in the images and the existence of image processing.

5. Images Assessment

The assessment of the images was divided into two different methods: subjective and objective analyses.

5.1. Subjective Analysis

For the subjective analysis, one nuclear medicine physician (2 years' experience) and one senior nuclear medicine technologist (more than 10 years' experience) were selected. They were presented with 48 images (raw and pixon-processed), resulting of the six experimental tests, in a blinded randomized order, for an independent review. The two professionals were requested to individually classify the six spheres in each image into visible or non-visible.

This qualitative evaluation was performed for the different acquisition modes. All images were visualized on HERMES interface, using the same type of workstation and colour LCD monitor, under the same lighting conditions. The scoring form is available in **Appendix 1**.

5.2. Objective Analysis

The set of images resulting from each experimental test, including those submitted to EPP, were also quantitatively analysed.

Since the phantom insert with hollow spheres belongs to the NEMA phantom, which is a suitable phantom for measurements of performance of PET systems, it was recognized that the obtained planar images could be quantitatively analysed using some image quality parameters used in PET studies. In order to implement this methodology, the guidelines of the NEMA phantom for performance of PET measurements of 2001 were used.

Making a measurement usually involves selecting one or numerous ROIs. According to the guidelines, circular ROIs were drawn on each sphere. These ROIs had a diameter as close as possible to the inner diameter of the sphere being measured: 10, 13, 17, 22, 28 and 37 mm. Additionally, six circular ROIs with 37 mm were drawn in the background equally distanced from each pair of spheres, with ROIs of smaller sizes (diameters of 10, 13, 17, 22 and 28 mm) concentric on the inside. On each image, a total of 36 ROIs in the background plus 6 ROIs matching the spheres were drawn (**Figure 45 (A)**) (56).

Since the location of all ROIs must be fixed between successive measurements, which means among all images, a manual ROI drawing was impracticable because manually defined regions are least reproducible, including within operators. Therefore, a movable ROI mask was the best method to be applied on each acquired image. With this purpose, a software package developed by MathWorks (MathWorks Inc., 2009), Matrix Laboratory (Matlab) version 7.12.0, was brought into play. Through Matlab it was possible to generate a semi-automatic approach to perform image measurements (**Figure 45 (B)**) (45).

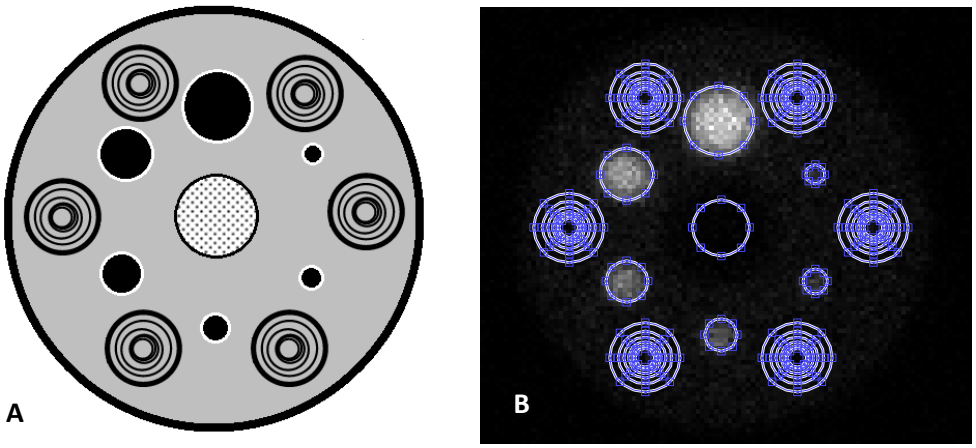

Figure 45 – ROI mask for the subjective analysis in accordance to the guidelines of the NEMA. A - Illustration of the ROIs drawing. One ROI on each sphere (white circles) and six groups of ROIs in the background (black concentric circles), with the cold cylinder represented on the inside (black dot pattern); B - ROI mask executed on Matlab.

In order to obtain the outcome visible in **Figure 45 (B)**, a specific NEMA analysis tool was used. This instrument was generated for PET images analysis, but for this particular investigation it was adapted to load planar scintigraphic images (courtesy of Willem Grootjans, Ph.D. student at the Radboud University Medical Centre).

The Matlab script was used according to the following steps:

1. Specify activity concentrations (Bq/mL) in the background and in the spheres;
2. Select one image of the acquired series for analysis: posterior view;
3. Load and display the image file, using Digital Imaging and Communications in Medicine (DICOM) format;
4. ROI mask is automatically loaded together with the DICOM file;
5. Crop image, specifying the shift form the middle line that needs to be included in the image;
6. Perform the alignment of the ROI mask, specifying the translation and rotation suitable for each image;
7. Load quantitative measurements for each sphere diameter: mean value of ROIs in the spheres, standard deviation of ROIs in the spheres; mean value of ROIs in the background; BV and CRC. Standard deviation in the background and COV were calculated as a general result for each image.

By using this adjusted script, Matlab turned to be a valuable tool regarding the calculations of the image quality parameters for objective analysis, since it also enables visualization and quantitative analysis of nuclear medical images. Given that the activity concentrations in the

spheres and in the background were known for each experimental test and that it was possible to obtain the average counts in the ROIs from the Matlab results, the quantitative parameters were automatically calculated (74).

The CRC, BV and COV were all computed. In addition, with base on the average and standard deviation of counts in the ROIs, it was also possible to calculate the SNR and CNR for each sphere within the images using Microsoft Excel version 2007.

Parameters used to crop the images and align the ROI mask were recorded in case of need to reproduce the measurements. Moreover, these values were kept fixed between raw and processed images from the same scan in order to attain comparable results.

6. Statistical Analysis

The statistical analysis of the data was performed using the software SPSS version 22 for Windows. The significance value was established as $\alpha = 0.05$.

Since reliability of professionals' rating is an important factor in areas such diagnosis and interpretation of examination findings, measures of agreement between professionals during subjective images assessment were estimated. Kappa coefficient was the selected measure for inter-observer variation. Levels of agreement were established according to Landis and Koch (**Figure 46**) (75).

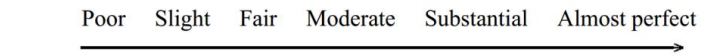

Kappa	Agreement
< 0	Less than chance agreement
0.01–0.20	Slight agreement
0.21– 0.40	Fair agreement
0.41–0.60	Moderate agreement
0.61–0.80	Substantial agreement
0.81–0.99	Almost perfect agreement

(76)

Figure 46 - Scheme for the interpretation of the Kappa value, according to Landis and Koch.

In order to estimate the potential differences between activity concentrations used in each experimental test, an independent samples Kruskal-Wallis test was applied. The aim was to prove that the activity distribution in the background was the same across categories of scan speed for each experimental test and that the activity distribution in the spheres was similar across categories of scan speed for each experimental test.

Wilcoxon matched pairs signed-rank tests were applied to access the distribution of independent samples from multiple measurements of quantitative dimensions, including BV, CRC, CNR and SNR. The parameters were compared within the same scan speed (raw and processed series), with the intention of investigating possible improvements in image quality after images being processed. A comparison between results from the standard protocol and protocols with increased scan speed after processing was also performed. For this analysis, the aim was to determine the limits of increasing the scan speed imaging parameter when the processing algorithm is applied (77).

III. Results

1. Phantom activity measurements

After concluding all the experimental tests, the attained sphere-to-background activity ratios were: 4:1, 8:1, 17:1, 22:1, 32:1 and 71:1.

1.1. Background

On a first evaluation, it was observed that the activity distribution in the background was similar across categories of scan speed for each experimental test, with a p-value of 0.374 $(p > \alpha)$.

The initial and the final activity concentrations in the background for each experimental test were calculated using the exponential activity decay formula and are described in **Table 8**. The minimum activity concentration corresponds to the last acquisition (8 cm/min scan speed); and the maximum to the first acquisition (20 cm/min scan speed). Mean values were also calculated.

Table 8 – Activity concentrations (Bq/mL) in the background calculated for each experimental test.

Activity Concentration (Bq/mL)			
Ratio	**Minimum**	**Maximum**	**Mean**
4:1	621.465	662.043	643.279 (± 17.725)
8:1	638.866	710.163	683.680 (±31.353)
17:1	729.812	770.344	751.684 (± 17.475)
22:1	744.078	783.598	765.044 (± 17.069)
32:1	707.147	744.705	727.072 (± 16.222)
71:1	678.952	713.370	697.672 (± 14.991)

The calculated minimum and maximum activity concentrations for each experimental test can also be analysed using the graph represented on **Figure 47**.

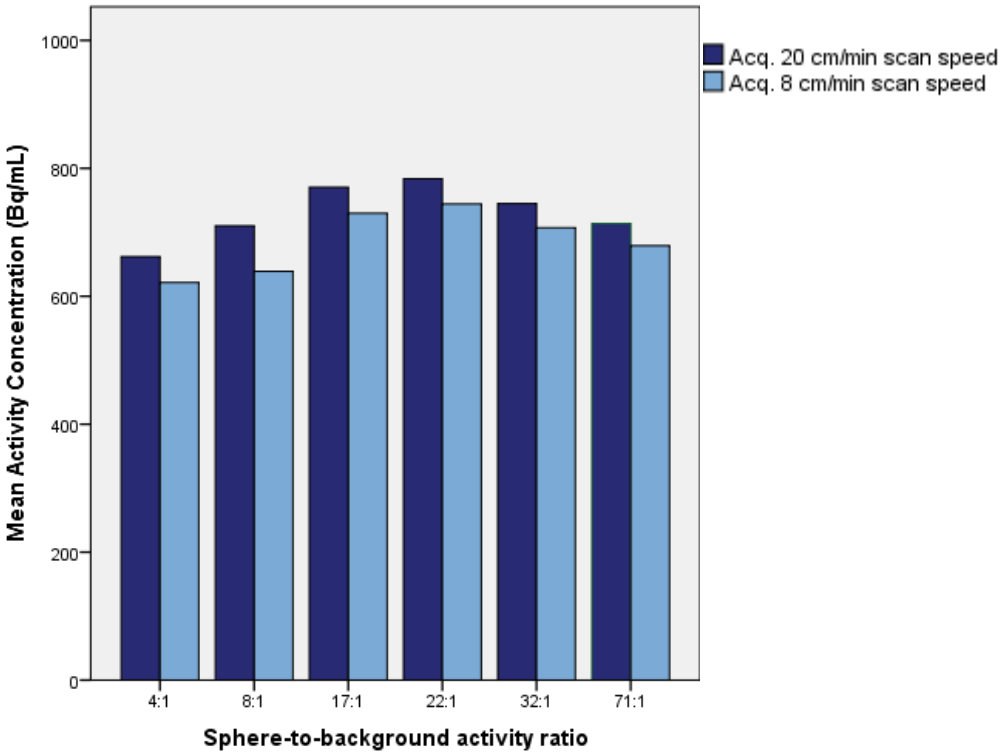

Figure 47 – Graph representing the background activity concentrations (Bq/mL).

The count rate in the background was determined by means drawing of ROIs. When comparing the observed count rate in the background of the phantom images (acquired with 8 cm/min scan speed) with the observed value in the patients' series, no statistical significant differences were recorded (**Table 9**).

Table 9 – Count rate (cps) registered in the background of the images acquired with 8 cm/min scan speed, for the six phantom experimental tests.
No statistically significant differences were found in relation with the count rate established in the patients' series.

Count Rate (cps)				
Ratio	**Minimum**	**Maximum**	**Mean**	**Sig.**
4:1	4.755	4.920	4.794 (± 0.062)	
8:1	4.321	4.664	4.546 (± 0.127)	
17:1	5.521	5.817	5.656 (± 0.111)	
22:1	5.843	6.051	5.936 (± 0.073)	$p > \alpha$
32:1	5.620	6.040	5.792 (± 0.143)	
71:1	6.154	6.397	6.261 (± 0.105)	
Patients' series	3.280	7.710	5.430 (± 1.260)	

From **Table 9**, one can observe that the minimum and the maximum values of the count rates registered in the phantom images are comprehended in the range defined by the results observed in the patients' series.

1.2. Spheres

On a first analysis, it was possible to find that the activity distribution in the spheres was similar across categories of scan speed for each experimental test, with a p-value of 0.896 $(p > \alpha)$.

The activity concentrations (Bq/mL) concerning each experimental test were calculated by means of the exponential activity decay formula and are described in **Table 10**.

Table 10 - Activity concentration (Bq/mL) in the spheres calculated for each experimental test.

Activity Concentration (Bq/mL)			
Ratio	**Minimum**	**Maximum**	**Mean**
4:1	2453.124	2613.296	2539.229 (±69.966)
8:1	5300.976	5892.562	5672.819 (±260.152)
17:1	12530.044	13225.930	12905.554 (±300.029)
22:1	16119.961	16976.132	16574.171 (±369.794)
32:1	22807.731	24019.105	23450.381 (±523.211)
71:1	48599.159	51062.799	49939.136 (±1073.032)

The calculated minimum and maximum activity concentrations on the spheres for each experimental test can also be analysed using the graph represented on **Figure 48**.

With **Figure 48** one can easily observe the activity proportion between the background and the spheres within each experiment. The mean activity concentration in the background remained approximately the same across experiments while the mean activity concentration in the spheres increased each time in order to achieve the desired sphere-to-background activity ratios.

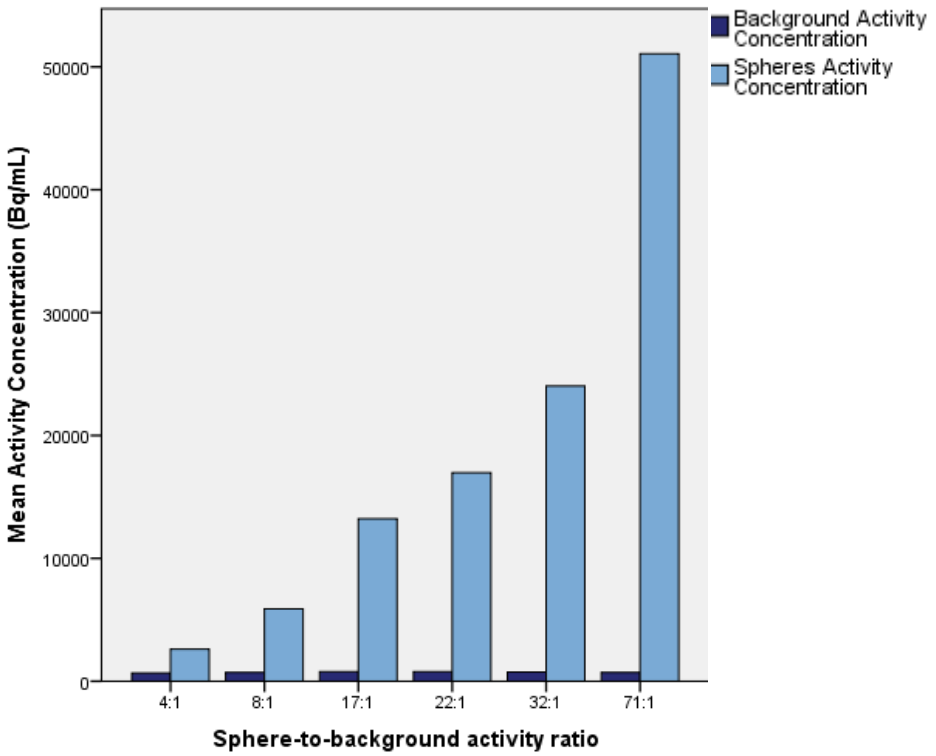

Figure 48 - Graph representative of the activity concentrations (Bq/mL) in the background and spheres during each experimental test.

2. Subjective Assessment

From **Figure 49** to **Figure 54** is possible to observe the acquired image series during each experimental test. The images were individually assessed by two observers, in which the spheres were classified into visible or non-visible. The scores are registered next to each figure, using the sequence of scan speeds, from 8 to 20 cm/min, respectively. Image scores can be fully accessed in **Appendix II**, at the end of the document.

Generalized kappa coefficient (K-value) was estimated in order to quantify the level of inter-observer agreement (**Table 11**).

Table 11 – Estimation of inter-observer generalized kappa coefficients of agreement.

Image type	K-value	Level of agreement
Raw Images	0.765	Substantial
Processed Images	0.652	Substantial

Table 11 shows that the observers have a substantial level of agreement for both image types; however, the kappa value was found to be slightly higher for raw images.

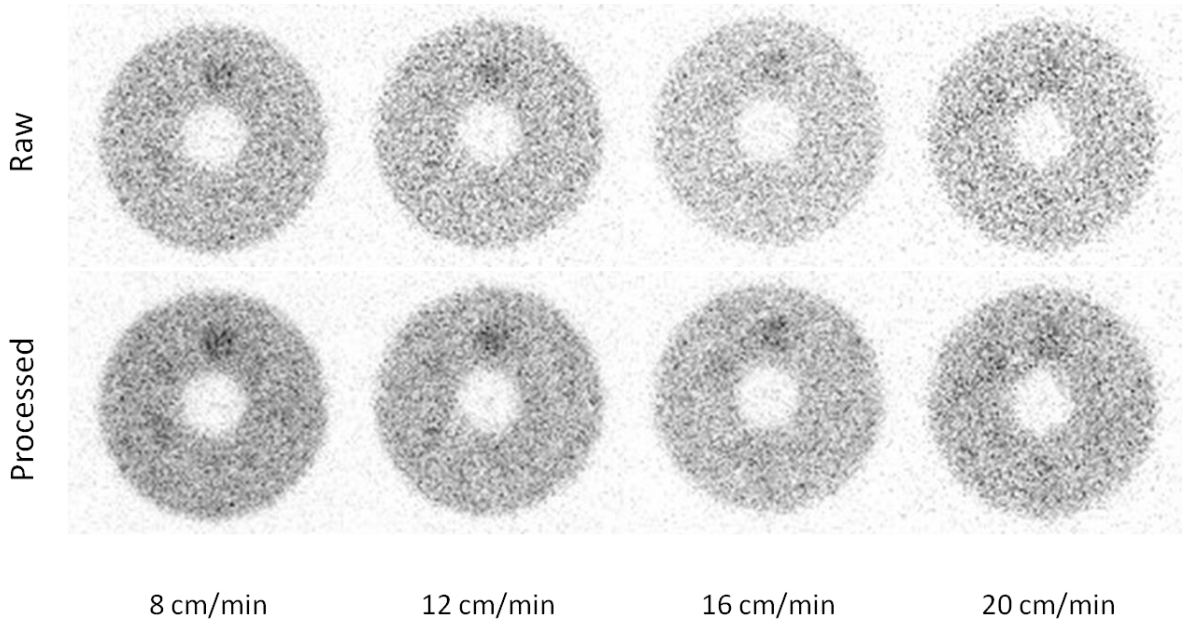

Figure 49 - Image series from experimental test 1. Sphere-to-background activity ratio of 4:1.
Raw images: 1-0-0-0 (Observer 1); 1-1-1-0 (Observer 2);
Processed images: 1-1-0-0 (Observer 1); 3-2-2-1 (Observer 2).

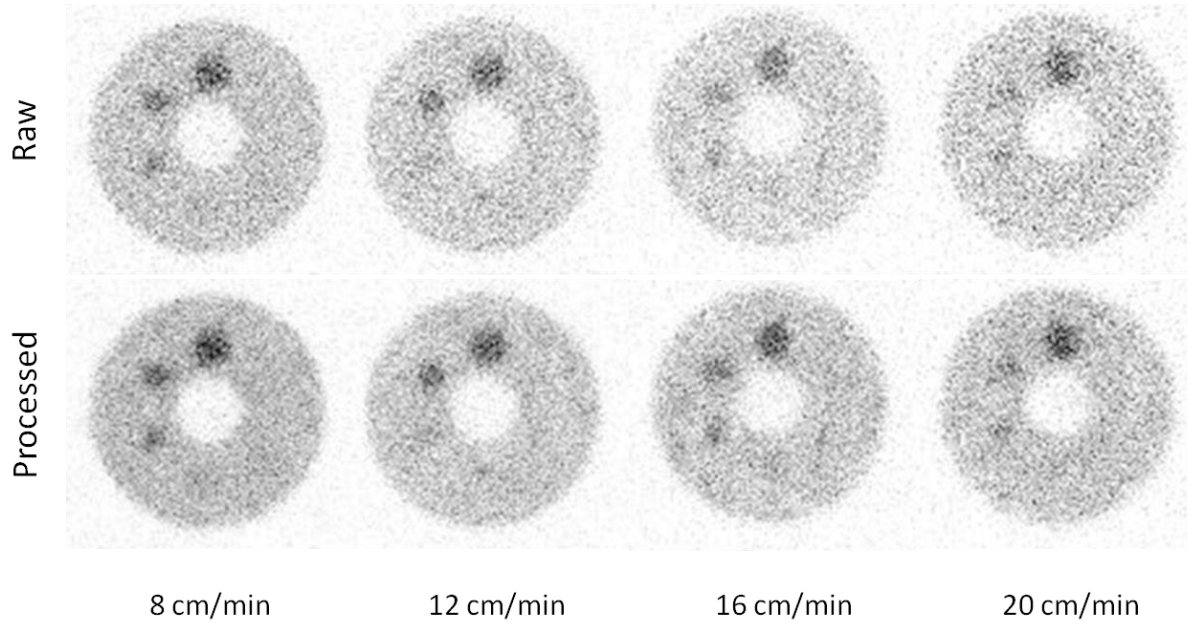

Figure 50 - Image series from experimental test 2. Sphere-to-background activity ratio of 8:1.
Raw images: 3-2-3-1 (Observer 1); 4-3-4-3 (Observer 2);
Processed images: 3-2-3-2 (Observer 1); 4-4-4-3 (Observer 2).

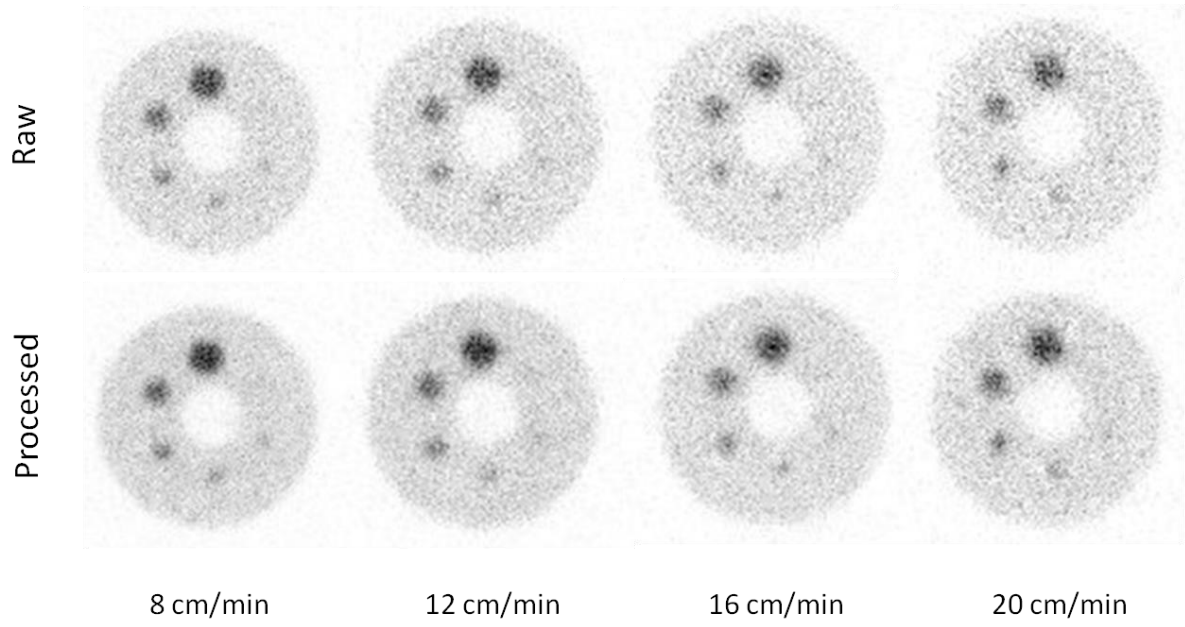

Figure 51 - Image series from experimental test 3. Sphere-to-background activity ratio of 17:1.
Raw images: 5-4-4-3 (Observer 1); 5-5-5-5 (Observer 2);
Processed images: 5-4-4-4 (Observer 1); 5-5-5-5 (Observer 2).

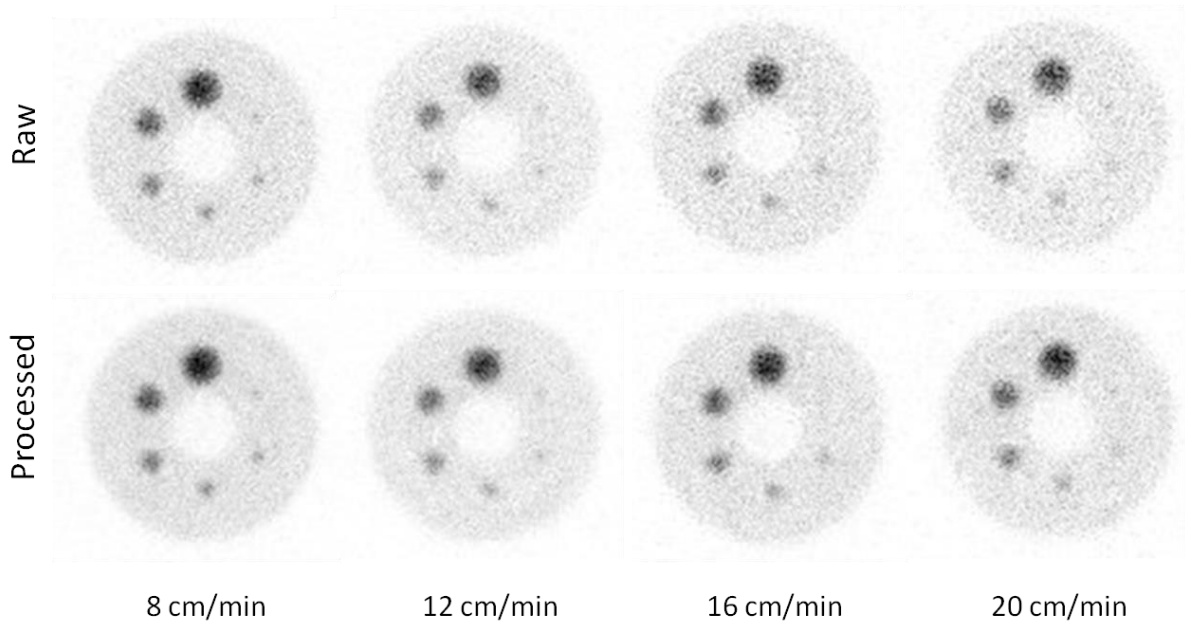

Figure 52 - Image series from experimental test 4. Sphere-to-background activity ratio of 22:1.
Raw images: 6-6-5-5 (Observer 1); 6-6-5-5 (Observer 2);
Processed images: 6-6-5-5 (Observer 1); 6-6-5-6 (Observer 2).

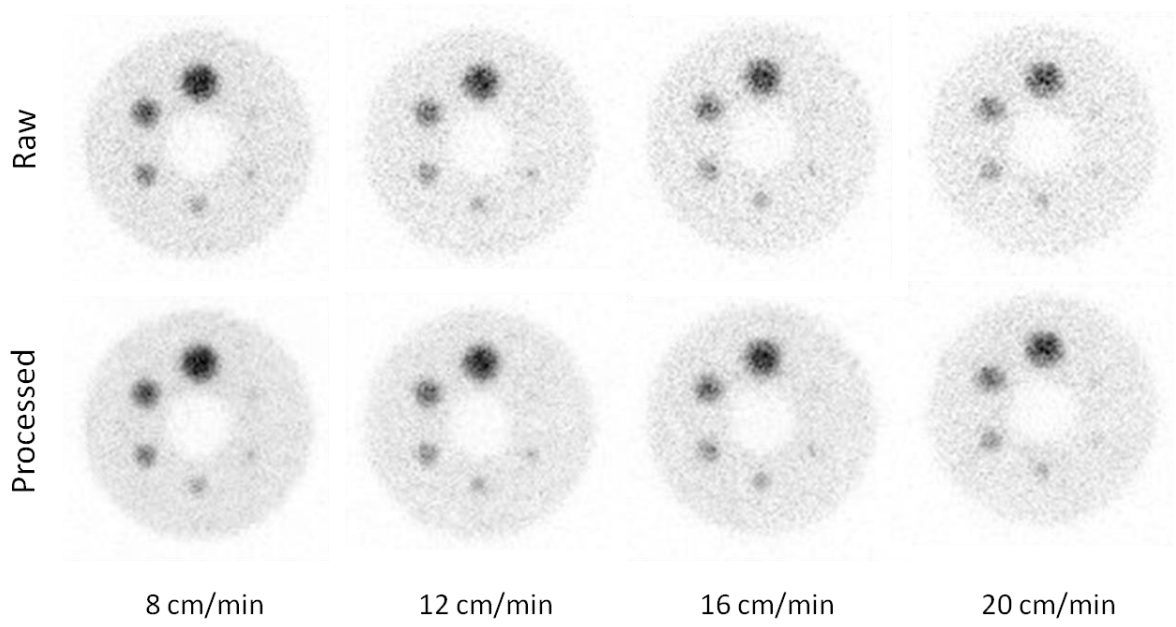

Figure 53 - Image series from experimental test 5. Sphere-to-background activity ratio of 32:1.
Raw images: 5-5-4-4 (Observer 1); 6-5-5-6 (Observer 2);
Processed images: 5-5-5-4 (Observer 1); 6-6-4-6 (Observer 2).

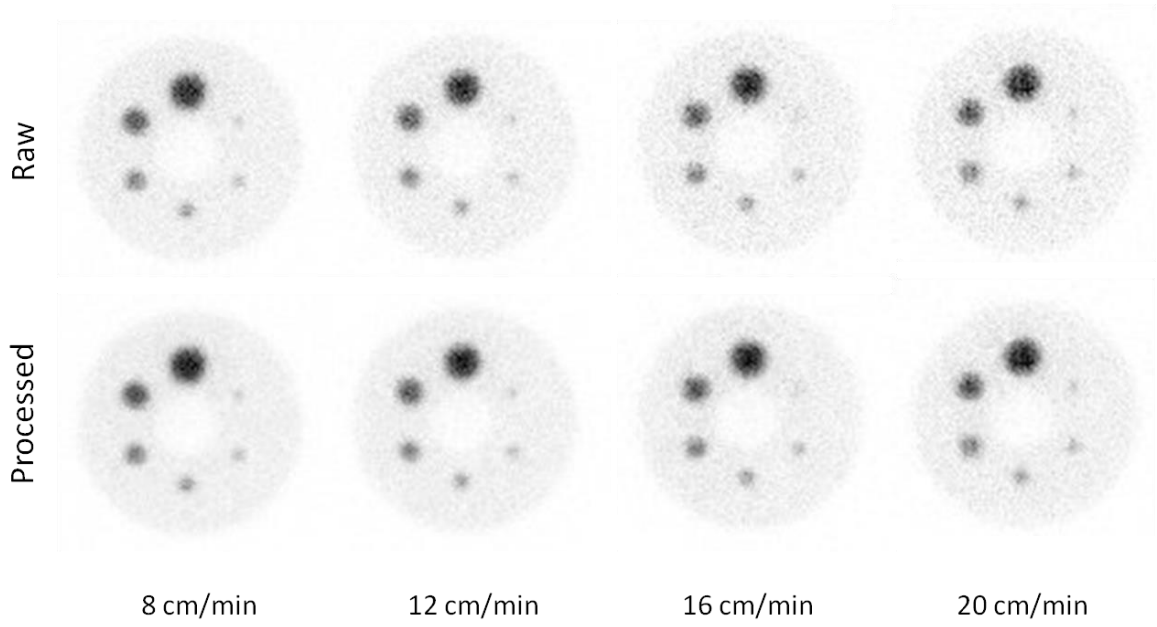

Figure 54 - Image series from experimental test 6. Sphere-to-background activity ratio of 71:1.
Raw images: 6-6-5-6 (Observer 1); 6-6-6-6 (Observer 2);
Processed images: 6-6-5-6 (Observer 1); 6-6-6-6 (Observer 2).

Table 12 gives an overall view of the results demonstrated across the last figures.

Table 12 – Number of visible spheres according to visual analysis of the two observers. The scores are registered using the sequence of scan speeds, from 8 to 20 cm/min, respectively.

Ratio	Raw Images		Processed Images	
	Observer 1	**Observer 2**	**Observer 1**	**Observer 2**
4:1	1-0-0-0	1-1-1-0	1-1-0-0	3-2-2-1
8:1	3-2-3-1	4-3-4-3	3-2-3-2	4-4-4-3
17:1	5-4-4-3	5-5-5-5	5-4-4-4	5-5-5-5
22:1	6-6-5-5	6-6-5-5	6-6-5-5	6-6-5-6
32:1	5-5-4-4	6-5-5-6	5-5-5-4	6-6-4-6
71:1	6-6-5-6	6-6-6-6	6-6-5-6	6-6-6-6

From the analysis of the last set of figures together with **Table 12**, one can notice that: in general, the scores distribution among the six experimental tests revealed that more spheres were identified after processing the images; moreover, the visualization of the spheres generally decreased when increasing the scan speed, as expected.

It is clear that spheres' detectability increases or remains approximately the same after processing the images. The increases are particularly observed in the lowest sphere-to-background activity ratio. At the highest sphere-to-background activity ratio, the activity concentration in the spheres becomes so high that no differences are described from raw to processed images, with the exception of the scan acquired with 16 cm/min in the opinion of observer 1.

There are, however, some other exceptions, particularly regarding detectability between the scans acquired at 16 cm/min and 20 cm/min. This phenomenon can be due to the interference of random Poisson noise, which usually affects scintigraphic images. The existence of this type of noise is responsible for decreasing both quantitative and qualitative aspects of the images. Due to its electronic nature, it results in an unpredictable behaviour that can degrade the imaging results in an arbitrary way. Only several acquisition replications of the series might clarify the incidence of this occurrence.

3. Objective Assessment

The objective assessment was performed with the calculation of several image quality parameters including: BV, CRC, CNR, SNR and COV. The measurements were computed for each set of scan conditions, being determined for each sphere size, with the exception of COV which was calculated as a global measurement with reference to each image.

Since the size and geometry of spheres influences the ROI mask placement and subsequently the error of the acquired results, the data described for BV, CRC, CNR and SNR correspond only to the largest sphere (37 mm diameter), which had higher detectability.

The statistical analysis performed for each image quality parameter (CRC, CNR and SNR) was based on the results calculated for the set of spheres identified by the observers in the standard image, so that the other protocols could be fairly compared. The statistical analysis of the percent BV, however, was based in the results of the entire set of ROIs for each image.

3.1. Experimental Test 1 – Sphere-to-background activity ratio of 4:1

Since the first experimental test corresponded to the poorest sphere-to-background activity ratio, only the largest sphere (37 mm diameter) was visualized by both observers in every image series. For that reason, no statistical analysis could be performed regarding image quality parameters since only one sphere was identified (**Table 13**).

Table 13 - Image quality parameters calculated for raw and processed images acquired during experimental test 1.

Scan Speed	Image type	Image Quality Parameter			
		BV	CRC	CNR	SNR
20 cm/min	**Raw**	4.528	9.286	0.499	2.324
	Processed	5.900	11.200	0.665	2.682
16 cm/min	**Raw**	2.153 $*$	12.259	0.671	2.527
	Processed	4.600 $*$	17.000	1.081	3.237
12 cm/min	**Raw**	2.939	15.417	0.895	2.866
	Processed	3.300	16.900	1.257	3.787
8 cm/min	**Raw**	1.901 $*$	13.342	0.863	3.057
	Processed	1.700 $*$	14.200	1.249	4.224

$* \ p \leq \alpha$

As expected, the mean results of the percent BV increased when increasing the scanning time. Thus, the acquisition protocol with 20 cm/min resulted in a raw image with higher BV (4.528 %) and the one with 8 cm/min in a lower BV (1.901 %).

In general, BV results seemed not to be affected after processing the images, remaining approximately the same or slightly higher. No statistical significant differences were found when comparing raw and processed images acquired with 20 cm/min and 12 cm/min scan speeds. On the contrary, the series acquired using 16 cm/min and 8 cm/min resulted in statistically significant differences between cases.

Despite the fact that some statistically significant differences were observed within BV, no specific pattern among image types could be established. The recorded differences and variations could be related to the placement of the ROIs in the background.

As supposed, CRC, CNR and SNR decreased when increasing the scan speed. Furthermore, a slight increase in all these results was recorded after processing the images. However, since the data was calculated just for one sphere, no statistical tests could be implemented.

The results from the comparison between standard image and processed images resulting from protocols with increased scan speeds are described in **Table 14**.

Table 14 - Assessment of image quality parameters calculated for experimental test 1. The image acquired with the standard acquisition protocol (8 cm/min scan speed) is compared to the processed images acquired with increased scan speeds.

Image Quality Parameter	Standard Image (8 cm/min)	Processed Images		
		12 cm/min	16 cm/min	20 cm/min
BV	1.901	3.300 $*$	4.600 $*$	5.900 $*$
CRC	13.342	16.900	17.000	11.200
CNR	0.863	1.257	1.081	0.665
SNR	3.057	3.787	3.237	2.682

$* \; p \leq \alpha$

Table 14 demonstrates the increase in the percent BV across the scan speed, as well as the variations in relation with the image acquired using the standard protocol. Statistically significant differences were observed within all the cases regarding the percent BV.

However, this seemed not to affect the visualization of the spheres. In fact, it was noticed that more spheres (or the same in the case of 20 cm/min) were scored during the subjective

assessment when comparing the image acquired with the standard protocol with those acquired using higher scan speeds after being processed.

Moreover, when exploring the results regarding CRC, CNR and SNR, it is clear that there were improvements after processing the images; as expected, CNR and SNR decreased with scan speed in such order that slight declines were noticed concerning image quality and object depiction, particularly in the image acquired using the protocol with 20 cm/min scan speed.

3.2. Experimental Test 2 – Sphere-to-background activity ratio of 8:1

Results from the experiments using the sphere-to-background activity ratio of 8:1 are described in **Table 15**, for each scan speed. Spheres included in the statistical tests: 37 mm, 28 mm, 22 mm and 17 mm.

Table 15 – Image quality parameters calculated for raw and processed images acquired during experimental test 2.

Scan Speed	Image type	Image Quality Parameter			
		BV	CRC	CNR	SNR
20 cm/min	Raw	2.704	12.990	1.712	3.518
	Processed	6.400	17.500	2.482	4.422
16 cm/min	Raw	5.698	14.331	1.935	3.786
	Processed	7.500	16.200	2.592	4.785
12 cm/min	Raw	2.837 $*$	15.854	2.369	4.418
	Processed	4.400 $*$	16.800	3.183	5.780
8 cm/min	Raw	3.284	14.334	2.321	4.541
	Processed	3.900	13.700	2.993	5.991

$*$ $p \leq \alpha$

In general, slight increases were noted regarding BV among image types. However, statistically differences were only recorded in the image series resulting from the scan acquired using 12 cm/min scan speed. In this particular test, no specific pattern for BV was established when considering the different scan speeds, meaning that this parameter might had the influence of external effect, including ROI positioning in the background.

On the other hand, CRC, CNR and SNR mean values increased or remained approximately the same from raw to processed images among scan speeds. Nevertheless, no statically significant differences were found for these parameters for all cases.

The results from the comparison between standard image and processed images resulting from protocols with increased scan speeds are described in **Table 16**.

Table 16 - Assessment of image quality parameters calculated for experimental test 2. The image acquired with the standard acquisition protocol (8 cm/min scan speed) is compared to the processed images acquired with increased scan speeds.

Image Quality Parameter	Standard Image (8 cm/min)	Processed Images		
		12 cm/min	16 cm/min	20 cm/min
BV	3.284	4.400	7.500 $*$	6.400 $*$
CRC	14.334	16.800	16.200	17.500
CNR	2.321	3.183	2.592	2.482
SNR	4.541	5.780	4.785	4.422

$* \ p \leq \alpha$

As seen in previous experiments, the percent BV increased when using higher scan speeds. All the results presented statistical significant differences when compared to the standard image, with the exception of the one acquired using the protocol of 12 cm/min scan speed.

As expected, image quality parameters CRC, CNR and SNR decreased with scan speed. Still, these results remained in general approximately the same or even slightly increased when compared with the standard image. For that reason, no statistically significant differences were found between all the scan conditions when compared to the standard protocol.

3.3. Experimental Test 3 – Sphere-to-background activity ratio of 17:1

Results from the experiments using the sphere-to-background activity ratio of 17:1 are described in **Table 17**, for each scan speed. Spheres included in the statistical tests: 37 mm, 28 mm, 22 mm, 17 mm and 13 mm.

Through **Table 17** is possible to observe that the percent BV results remained comparable across the different scan speeds between image types. Statistically significant differences were absent in all the scan conditions.

Table 17 – Image quality parameters calculated for raw and processed images acquired during experimental test 3.

Scan Speed	Image type	Image Quality Parameter			
		BV	CRC	CNR	SNR
20 cm/min	Raw	6.486	14.365 ∗	4.307 ∗	6.161 ∗
	Processed	6.000	16.700 ∗	5.696 ∗	7.806 ∗
16 cm/min	Raw	4.719	14.954 ∗	4.578 ∗	6.471 ∗
	Processed	5.000	16.000 ∗	4.143 ∗	8.466 ∗
12 cm/min	Raw	4.581	17.046 ∗	5.786 ∗	7.940 ∗
	Processed	6.000	17.000 ∗	7.810 ∗	10.685 ∗
8 cm/min	Raw	4.318	16.411	6.138 ∗	8.451 ∗
	Processed	5.000	16.000	8.439 ∗	11.629 ∗

$* \ p \leq \alpha$

When comparing the raw image acquired during this experimental test with the processed ones, is clearly seen that CRC, CNR and SNR increase after processing the images. Still, CRC remained approximately the same in the case of the lower scan speeds (12 cm/min and 8 cm/min). Statistically significant differences in CRC, CNR and SNR were found among all the cases regarding the image type. As regards the percent CRC, the only exception was seen in the series acquired with 8 cm/min scan speed.

The results of the comparison between standard images and processed images resulting from faster protocols are described in **Table 18**.

Table 18 - Assessment of the image quality parameters calculated for experimental test 3. The image acquired with the standard acquisition protocol (8 cm/min scan speed) is compared to the processed images acquired with increased scan speeds.

Image Quality Parameter	Standard Image (8 cm/min)	Processed Images		
		12 cm/min	16 cm/min	20 cm/min
BV	4.318	6.000 ∗	5.000	6.000 ∗
CRC	16.411	17.000	16.000	16.700 ∗
CNR	6.138	7.810 ∗	4.143	5.696
SNR	8.451	10.685 ∗	8.466	7.806 ∗

$* \ p \leq \alpha$

Through **Table 18** one easily concludes that the general tendency of most part of the parameters to decrease with the scan speed remains as expected. Still, the results remain very close to each other. For BV, statistically significant differences were observed when comparing the protocols with 12 cm/min and 20 cm/min scan speeds.

With this specific sphere-to-background activity ratio, some important figures come to play: CNR and SNR increased in such order for 12 cm/min scan speed that statistically significant differences were observed; moreover, CRC, CNR and SNR of the image acquired with 16 cm/min scan speed remained in the order of those regarding the standard protocol, with no statistically significant differences in between; for 20 cm/min scan speed, some decreases were observed, more particularly in SNR, in which statistically significant differences were noticed.

3.4. Experimental Test 4 – Sphere-to-background activity ratio of 22:1

Results from the experiments using the sphere-to-background activity ratio of 22:1 are described in **Table 19**, for each scan speed. All spheres were included in the statistical tests.

Table 19 – Image quality parameters calculated for raw and processed images acquired during experimental test 4.

Scan Speed	Image type	Image Quality Parameter			
		BV	CRC	CNR	SNR
20 cm/min	**Raw**	6.540	19.721	7.7482 ∗	9.650 ∗
	Processed	8.000	21.000	9.911 ∗	12.156 ∗
16 cm/min	**Raw**	11.150	17.278 ∗	7.100 ∗	9.089 ∗
	Processed	6.000	21.000 ∗	10.699 ∗	13.188 ∗
12 cm/min	**Raw**	9.422 ∗	21.299	9.378 ∗	11.508 ∗
	Processed	8.000 ∗	22.000	12.382 ∗	15.113 ∗
8 cm/min	**Raw**	5.047	21.512	11.042 ∗	13.526 ∗
	Processed	6.000	21.000	14.983 ∗	18.377 ∗

$* \ p \leq \alpha$

For this experimental test it was observed that the mean values of percent BV remained approximately the same among image types across the different speed scans. No statistically significant differences were observed for all the scan conditions, with the exception of the acquisition with 12 cm/min scan speed in which BV decreased from 9.422 % to 8.000 %.

Moreover, no specific pattern could be established for this parameter, probably due to the ROI mask positioning in the background.

In general, the mean values of CRC, CNR and SNR increased or remained approximately the same after processing the images. This resulted in consequent significant differences for CNR and SNR across all the scan speeds. However, CRC only demonstrated statistically significant differences for the protocol with a scan speed of 16 cm/min (mean value increased from 17.278 % to 21.000 %).

The results of the comparison between standard image and processed images resulting from faster protocols are described in **Table 20**.

Table 20 - Assessment of the image quality parameters calculated for experimental test 4. The image acquired with the standard acquisition protocol (8 cm/min scan speed) is compared to the processed images acquired with increased scan speeds.

Image Quality Parameter	Standard Image (8 cm/min)	Processed Images		
		12 cm/min	16 cm/min	20 cm/min
BV	5.047	8.000	6.000 $*$	8.000 $*$
CRC	21.512	22.000	21.000	21.000 $*$
CNR	11.042	12.382	10.699	9.911 $*$
SNR	13.526	15.113	13.188	12.156 $*$

$* \ p \leq \alpha$

According to the results of **Table 20**, the percent BV shown increases when increasing the scan speed, registering statistically significant differences when comparing the protocols with 16 and 20 cm/min scan speeds with the standard protocol.

One can also conclude that the mean values of CRC, CNR and SNR for the protocols with 12 cm/min and 16 cm/min scan speeds remained slightly higher or very close to those obtained with the standard image, with absence of statistically significant differences. Though, for the image acquired with 20 cm/min scan speed all these parameters decreased, resulting in significant differences regarding the standard protocol.

3.5. Experimental Test 5 – Sphere-to-background activity ratio of 32:1

Results from the experiments using the sphere-to-background activity ratio of 32:1 are described in **Table 21**, for each scan speed. All spheres were included in the statistical tests.

Table 21 - Image quality parameters calculated for raw and processed images acquired during experimental test 4.

Scan Speed	Image type	Image Quality Parameter			
		BV	CRC	CNR	SNR
20 cm/min	Raw	7.569 ∗	13.422 ∗	7.647 ∗	9.470 ∗
	Processed	12.000 ∗	15.000 ∗	9.949 ∗	12.067 ∗
16 cm/min	Raw	4.985	14.126	8.740 ∗	10.719 ∗
	Processed	5.000	15.000	11.460 ∗	13.968 ∗
12 cm/min	Raw	6.847 ∗	15.641	10.013 ∗	12.061 ∗
	Processed	9.000 ∗	16.000	13.156 ∗	15.789 ∗
8 cm/min	Raw	4.247 ∗	14.816	11.043 ∗	13.428 ∗
	Processed	4.000 ∗	15.000	15.021 ∗	18.310 ∗

$* \ p \leq \alpha$

Percent BV demonstrated once again an undefined pattern, with increases and decreases across the scan conditions. The more pronounced increases were observed in 20 cm/min (7.569 % to 12.000 %) and 12 cm/min (6.847 % to 9.000 %), resulting in statistically significant differences for both cases. On the contrary, images acquired at 8 cm/min scan speed registered statistically significant differences due to the decrease on the percent BV (4.247 % to 4.000 %), however, the absolute results remained relatively comparable.

On the other hand, the percent CRC remained approximately the same between image types within categories of scan speed. Statistically significant differences were only recorded between images types acquired at 20 cm/min due to an improvement on this parameter.

As it happened in the last three experimental tests, the mean values of CNR and SNR increased in the processed images. As a result, these two parameters were statistically significant in all the scan conditions when comparing image types.

The results of the comparison between standard image and processed images resulting from faster protocols are described in **Table 22**.

Table 22 - Assessment of the image quality parameters calculated for experimental test 5. The image acquired with the standard acquisition protocol (8 cm/min scan speed) is compared to the processed images acquired with increased scan speeds.

Image Quality Parameter	Standard Image (8 cm/min)	Processed Images		
		12 cm/min	16 cm/min	20 cm/min
BV	4.247	9.000 $*$	5.000	12.000 $*$
CRC	14.816	16.000	15.000	15.000 $*$
CNR	11.043	13.156 $*$	11.460	9.949 $*$
SNR	13.428	15.789 $*$	13.968	12.067 $*$

$* \ p \leq \alpha$

After the analysis of **Table 22** one can realize that the protocol with 12 cm/min scan speed had the most dramatic improvement in image quality, with increases in CRC, CNR and SNR, having CNR and SNR statistically significant differences when compared with the results of the standard protocol.

When looking at the protocol with 16 cm/min scan speed, a light increase in CRC, CNR and SNR can also be noticed, as well as a slight decrease in percent BV. Since all the results are very close to those achieved with the standard protocol, no statistical significant differences were recorded for all the image quality parameters, even regarding BV.

For the image acquired with 20 cm/min scan speed, CNR and SNR decreased in such order that statistically significant differences were recorded. CRC also recorded significant differences, however, the results remained very close to the standard image. Besides, percent BV showed the most significant increase when compared to the other scan speeds (4.247 % to 12.000 %), registering statistically significant differences.

3.6. Experimental Test 6 – Sphere-to-background activity ratio of 71:1

Results from the experiments using the sphere-to-background activity ratio of 71:1 are described in **Table 23**, for each scan speed. All spheres were included in the statistical tests.

Table 23 – Image quality parameters calculated for raw and processed images acquired during experimental test 6.

Scan Speed	Image type	Image Quality Parameter			
		BV	CRC	CNR	SNR
20 cm/min	**Raw**	7.865 ∗	12.189	15.901 ∗	17.750 ∗
	Processed	10.000 ∗	13.000	20.241 ∗	22.389 ∗
16 cm/min	**Raw**	8.209	12.741	17.191 ∗	19.103 ∗
	Processed	12.000	13.000	22.384 ∗	24.790 ∗
12 cm/min	**Raw**	9.103	12.729	19.405 ∗	21.565 ∗
	Processed	9.100	12.700	25.668 ∗	28.530 ∗
8 cm/min	**Raw**	11.662	12.771	21.174 ∗	23.523 ∗
	Processed	11.900	12.700	27.523 ∗	30.592 ∗

$* \ p \leq \alpha$

The results summarized in the previous table demonstrate that for this experiment the percent BV increased in the highest scan speeds and remained approximately the same in the lowest. However, statistically significant differences were only recorded in the images acquired using a scan speed of 20 cm/min, where the mean values increased from 7.865 % to 10.000 %.

No differences were recorded regarding the percent CRC in all the cases, having both raw and processed images very similar results. On the other hand, CNR and SNR increased after processing the images, having those parameters statistically significant differences within all the scan conditions.

The results from the comparison between standard image and processed images resulting from faster protocols are described in **Table 24**.

Table 24 - Assessment of the image quality parameters calculated for experimental test 5. The image acquired with the standard acquisition protocol (8 cm/min scan speed) is compared to the processed images acquired with increased scan speeds.

Image Quality Parameter	Standard Image (8 cm/min)	Processed Images		
		12 cm/min	16 cm/min	20 cm/min
BV	11.662	9.100 $*$	12.000 $*$	10.000
CRC	12.771	12.700	13.000	13.000
CNR	21.174	25.668 $*$	22.384	20.241
SNR	23.523	28.530 $*$	24.790	22.389

$* \ p \leq \alpha$

From the analysis of **Table 24** is possible to observe that the image obtained with a scan speed of 12 cm/min was statistically superior to the one acquired using the standard protocol in almost every image quality parameter. The only exception was the percent CRC, which remained approximately the same having no statistically significant differences.

On the other hand, images acquired using 16 cm/min and 20 cm/min scan speeds had no statistically significant differences regarding CRC, CNR and SNR, with similar results to the ones obtained with the standard protocol. Still, the values from the protocol with 16 cm/min were higher. In contrast, BV results were more optimistic for the protocol with 20 cm/min scan speed, having the one with 16 cm/min statistically significant differences when compared to the standard protocol due to a slight increase on the range of values.

4. Results Overview

4.1. BV

The percent BV increases with the scan speed. This was observed in most cases, however, some exceptions have occurred. This means that the attained values were highly dependent on the positioning of the ROIs in the background, contributing to the appearance of these results variations.

Despite the fact that some statistically significant differences were observed regarding the percent BV, no specific pattern among image types could be established. This means that in general, BV results seemed not to be affected after processing the images, remaining approximately the same. Although increases in BV suggest noise increases, visual inspection

reveals that the noise increase is homogeneous throughout the image with absence of irregular variations.

4.2. CRC, CNR and SNR

As expected, the image quality parameters CRC, CNR and SNR decreased when increasing the scan speed.

As regards the first two experimental tests (sphere-to-background activity ratios of 4:1 and 8:1) no substantial differences between raw and processed images were recorded. However, the slight increases in these parameters allowed higher detectability when looking to the subjective assessment.

From experimental test 3, the increases in image quality parameters were found to be generalized. CNR and SNR increased values resulted in statistically significant differences every time, however, improvements in the CRC were not permanently significant.

When comparing the standard image with the processed images acquired with faster scan speeds, it was observed that:

- Processed images acquired using a scan speed of 12 cm/min had the most favourable results when compared to the standard images, with improved image quality parameters representing higher detectability. Statistically significant increases were seen more specifically in experimental tests 5 and 6;

- In contrast, processed images acquired with the protocol of 20 cm/min scan speed resulted in decreased image quality results, which were statistically significant in the cases of experimental tests 3, 4 and 5. At some point, the sphere-to-background activity ratio would be so high that the scan speed does not influence the object detectability;

- At last, processed images resulting from the protocol of 16 cm/min had the most comparable results as regards the standard image. No statistically significant differences were recorded within all experimental tests.

4.3. COV

Another important parameter that allows the general evaluation of the effect of the image processing algorithm is the percent COV.

The COV calculated for the performed experimental tests is described in **Table 25**. This parameter registered significant differences within all the cases when comparing raw with processed series. This means that there is a lower dispersion on the counts distribution in processed images.

Table 25 - Percent COV calculated for raw and processed images acquired during the different experimental tests.

Ratio	Image type	Scan Speed			
		20 cm/min	**16 cm/min**	**12 cm/min**	**8 cm/min**
4:1	**Raw**	54.791 ∗	53.876 ∗	50.739 ∗	46.180 ∗
	Processed	49.583 ∗	46.390 ∗	39.513 ∗	33.974 ∗
8:1	**Raw**	55.345 ∗	54.009 ∗	48.823 ∗	45.576 ∗
	Processed	51.561 ∗	45.606 ∗	38.509 ∗	33.875 ∗
17:1	**Raw**	53.947 ∗	52.806 ∗	46.442 ∗	43.219 ∗
	Processed	47.410 ∗	43.017 ∗	34.775 ∗	31.341 ∗
22:1	**Raw**	52.570 ∗	55.407 ∗	46.962 ∗	40.254 ∗
	Processed	44.549 ∗	40.172 ∗	36.619 ∗	29.461 ∗
32:1	**Raw**	54.746 ∗	50.511 ∗	48.791 ∗	41.941 ∗
	Processed	47.253 ∗	39.861 ∗	37.979 ∗	30.407 ∗
71:1	**Raw**	54.037 ∗	52.254 ∗	46.311 ∗	42.564 ∗
	Processed	46.517 ∗	41.580 ∗	34.959 ∗	32.596 ∗

$* \; p \leq \alpha$

It was also observed in **Table 25** that the processed image with the most similar results as regards standard image was the one acquired using 16 cm/min scan speed among all the experimental tests.

IV. Discussion

1. Phantom study

Sometimes, is difficult to simulate clinical imaging conditions when a phantom is used. In this particular work, some decisions were made in order to keep the results as realistic as possible. Performing this investigation by means of a phantom was a significant challenge; however, it plays an extremely important role as regards the optimization of the imaging technique before being tested in patients and subsequently applied to clinical practice (56).

During the investigation planning, the phantom was thought to have the most suitable arrangement for planar imaging. At the end, the final configuration acquired an extremely valuable piece - the set of hollow spheres from the NEMA phantom - that simplified the calculation of the image quality parameters.

Other investigations related to this topic, however, have chosen different approaches: Vija, *et al.* (2005) performed a similar investigation, using the Jaszczak phantom together its own accessories (set of rods and hollow spheres); Alternatively, Corné Snoijs developed a similar investigation in 2013 at the Amphia Hospital in Breda (Netherlands) using a planar phantom (52, 78).

2. Scanning plan

The scanning arrangement was planned to be as simple as possible. The scan speeds ranged from 8, 12, 16 to 20 cm/min with the intention of achieving, respectively, 100, 75, 50 and 25 % of the standard acquisition time. Instead, in a previous study developed at the same department by Jerry Rahawadan (2013), several scan speeds were selected to complete a similar investigation: 8, 10, 12, 14, 16, 18, 20, 22 and 24 cm/min. However, an excessive quantity of parameters might provide results extremely difficult to interpret (79).

On the work developed by Vija, *et al.* (2005) the scans were planed based on specific acquisition times during a static acquisition, using: 1, 2, 4, 8 and 15 minutes. The same scanning method was used in the investigation carried out at the Amphia Hospital, but the scans were acquired in a different range of acquisition times: 1, 2, 3 and 4 minutes (52, 78).

3. Radioactivity management

The amounts of radioactivity used during the experimental tests were thought to be as representative as possible. It is known that the precise mechanism of bone uptake of the radiopharmaceutical varies dramatically with the individualities of each patient, and

different normal or expected patterns of uptake and distribution can arise depending on: age and constitution of the patient, intake of drugs, degree of hydration and renal function. On the other hand, in the case of the soft tissue, increased or decreased activities in scintigraphy imaging are merely related to pathological features (80, 81).

Several methods for quantitative bone uptake measurements have been suggested. However, many of them present practical limitations in the clinical setting due to the limited resources to perform such studies. A practical method for quantification was suggested by Brenner, *et al.* in 1997. This method was described as a simple ROI technique applied to a conventional three-phase bone scanning to calculate bone uptake and soft-tissue retention. The referred ROI should include the adductor areas of both thighs. These areas were considered as representative of soft tissue since they are the largest areas of the body including soft tissue without overlapping of bones (73).

From the results of the study performed by Brenner, *et al.* (1997) it was concluded that patients with metabolic bone disease have a residual soft tissue activity of approximately 26.6 %, a percentage of injected activity calculated for 3 hours post-injection. The calculated time-activity curves fitted a monoexponential curve asymptotically reaching a plateau, with bone uptake having an increasing curve and the soft tissue retention a decreasing curve (73).

Since bone uptake of the radiopharmaceutical diverges intensely even in non-pathological patients, as explained before, in this investigation the activity concentration on the background of the phantom was based on the ROI measurements observed in the soft tissue. Considering 500 MBq the average amount of radioactivity injected to the patients, according to Brenner, *et al.*, the a residual soft tissue activity at 4 hours post-injection should be less than 5.320 MBq. The experimental method used to accomplish this result was performed using similar ROI measurements in images resulting from whole-body bone scintigraphic examinations. However, only the adductor area of right thigh was included in the ROI in order to use a quadrilateral configuration with a constant area and to avoid uncertainties arising from the void area between lower limbs (73).

The ROI measurements in the patient series allowed the establishment of an average count rate of 5.430 cps. In order to set an average amount of activity with a similar count rate that could be used in the solution to fill the background of the phantom, more experimental tests were performed. The cylinder phantom was imaged with different radioactive solutions on the inside. Through ROI measurements, it was possible to conclude that a solution containing 2.500 MBq resulted in a count rate of 4.850 cps. This result was in accordance with the exponential decreasing curve determined by Brenner, *et al.* (1997).

At the end of the experiments it was demonstrated that the activity concentrations in the background between trials was consistent, even when compared to the ROI measurements performed in the patients images.

If the uptake in the bone was chosen instead of soft tissue for setting the amount of activity for the background solution, a completely different approach should be made. From this point of view, more than one single activity in the background must be used to represent different groups of patients due to the variations in the uptake of the radiopharmaceutical in the bone. This method, however, could be extremely complex and, therefore, with more difficulties when accessing the results. Nevertheless, this might be a suggestion for further investigations.

Regarding the set of hollow spheres, each radioactive sphere was thought to simulate a bone containing metastatic lesions. Across the diverse experimental tests performed during the investigation, different sphere-to-background activity ratios were established: 4:1, 8:1, 17:1, 22:1, 32:1 and 71:1. The aim was to fully access the performance of the processing algorithm among different scenarios. It is important to note that the experimental tests are referred as volume concentration ratios, not the projected contrasts, which are reasonably inferior. Besides, thanks to the adaptation of the NEMA set of hollow spheres in the phantom, it was possible to calculate physical image quality parameters which are not usually computed for planar scintigraphic images.

The advantage of the phantom used in the investigation developed in the Amphia Hospital in 2013 was the fact that it was composed of four groups of round cylinders, each with four different depths: 2.5, 5, 10 and 20 mm. Each group had four cylinders with different diameters (5, 10, 15 and 20 mm) and the background had a constant depth of 2.5 mm. This means that different activity concentrations could be evaluated after a single scan (78).

An alternative imaging method was set by Vija, *et al*. (2005). Instead of varying the sphere-to-background activity ratio using different activity concentrations in the spheres, the researchers chosen to change the background activity concentration among experimental tests. The achieved activity contrast ratios were: 3:1, 4:1, 8:1 and 45:1. The selected amounts of activity were considerably higher when compared to the present work (between 45 MBq and 200 MBq in the background, and 0,2 MBq/cm^3 in the spheres), however, these should be provably too high for realistic connotations (52).

4. Experimental tests

With regard to the results of the performed experiments, two types of image assessment were performed: subjective and objective.

4.1. Subjective assessment

The images obtained during this investigation were subjectively evaluated by means of human observer performance. Due to several influencing factors, including the complexity of the human vision as well as observer experience and occupation, this method can be uncertain in terms of it objectivity. Though, in most cases, detectability is determined more accurately by direct evaluation of human observers (39).

The results can also be influenced by expectation, i.e. the configuration of the spheres within the images was unchanged and easy to recognise, being the spots detected sooner than in an unknown scenario.

From the subjective analysis of the acquired images it was possible to observe that in most cases, the scores distribution among the six experimental tests revealed that more spheres were identified after processing the images. As expected, the visualization of the spheres decreased when increasing the scan speed (34).

In general, the levels of detectability registered in the image acquired using the standard protocol were similar to those achieved in processed images acquired using scan speeds of 12 cm/min and 16 cm/min. Some discrepancies were observed regarding the 10 mm diameter sphere between images acquired with 16 cm/min and 20 cm/min. However, this might be due to the Poisson noise statistics, which results in an unpredictable behaviour that can degrade the imaging features. Only several acquisition replications of the series might clarify the incidence of this occurrence.

Analogous results were registered in the investigation developed by Corné Snoijs at the Amphia Hospital: the standard image acquired during 4 minutes had equivalent detectability when compared to processed images acquired with 3 (75 % of the standard acquisition time) and 2 minutes (50 % of the standard acquisition time) (78).

Vija *et al.* (2005) also concluded in their experiments that spheres that are barely seen in the raw counts were clearly seen in processed images, having improved detectability «with matched images somewhere in between» (52).

4.2. Objective assessment

Besides qualitative methods, a quantitative evaluation was performed using ROI measurements and calculation of physical image quality parameters. The ROI measurements were performed based on the guidelines of the NEMA body phantom for PET measurements, adapted for planar scintigraphic imaging. The same methodology was used in the study developed at the Amphia Hospital (56).

It is known that the image SNR is proportional to the square root of the total number of detected gamma rays. For that reason, this parameter is affected by factors such the amount of administered radiotracer, the incubation time and the duration of the scan. The CNR, on the other hand, is mainly influenced by the scatter effects and the non-specific uptake of radiotracer in healthy tissue surrounding the lesion being studied. Still, image post-processing plays a very important role in determining either SNR or CNR (82).

Both SNR and CNR improved when using the Pixon processing algorithm. However, statistically significant differences between image types were only recorded from sphere-to-background activity ratio of 17:1. Moreover, images acquired with the standard protocol registered comparable results regarding processed images with reduced acquisition times. The processed series with more similar results to those acquired using the standard protocol were the ones acquired with 16 cm/min scan speed.

In the investigation performed by Corné Snoijs, increases in CNR were recorded in the order of 25 %. Besides, it was noticed that the same results regarding this parameter could be achieved with processed images acquired with half the acquisition time (78).

Even using different activity levels and image quality parameters, Vija, *et al*. also demonstrated that noise was reduced after processing the acquired images, while maintaining resolution and avoiding the introduction of artefacts (52).

Still, Vija, *et al*. developed an additional study in which SPECT projection data was processed using the same processing algorithm. They concluded that the noise reduction resulted in significant improvements in detectability based on SNR measures, however, only a minor gain was recorder when testing with human observers (83).

The percent CRC observed across experimental tests was found to be approximately the same when comparing raw with the corresponding processed images. The processed series with more similar results to those acquired using the standard protocol were the ones acquired with 16 cm/min scan speed. In the study developed at the Amphia Hospital, CRC denoted a general decrease of 3 % when comparing raw with processed images (78).

With regard to the percent COV, there was a consistent behaviour across the different experimental tests. In general, decreases of 10 % were registered between raw and processed images within all scan speeds. The same kind of performance was registered in the study of Corné Snoijs, however, the decreases were in the order of 40 %. In addition, it was seen in every trial that the processed image acquired with 16 cm/min scan speed achieved the most comparable results with reference to the standard image (78).

There are many external factors that can influence quantitative results, including calibration and error of the dose calibrator in the hot lab, manipulation of the phantom and respective filling. In addition, since planar images are characterized by random Poisson noise, it can be an additional factor that may have an unpredictable influence on the results since it is mainly

associated to electronic noise. Therefore, only several repetitions of the experimental tests can reduce the inherent likely error that can arise from countless sources (42, 45).

The images were quantitatively analysed by means of a ROI technique. Since a semiautomatic method was used, there was a chance of inducing error in the results due to the placement of the ROI mask. Furthermore, minor inaccuracies during the ROI mask alignment might subsequently affect calculations of the image quality parameters.

5. Limitations of the study

If the results from a phantom study are provided just from a single set of experimental tests, the outcome can occasionally give indications of one particular imaging situation. This is for sure one of the limitations of the study. Due to the limited period of time, and also because of the need to create a suitable methodology for the investigation which took a considerable amount of time, the experimental tests were only performed once (56).

The present work was only based on the description of hot lesions. The influence of the investigated processing algorithm in cold lesions was not considered, but it can be a good purpose for further investigation.

One final observation must be made to mention that there are just a few studies performed in this field of investigation, and only one used similar methods. Thus, it was extremely difficult to find comparable results to fully discuss the achieved conclusions.

6. Clinical applicability

For sure, these results also need to be established in clinical investigations. For that reason, a parallel study took place in the same department during the time of this investigation. The final goal was to understand the clinical impact of this method. Fifty one patients with indications of prostate and breast carcinoma referred for whole-body bone scintigraphy were included. The patients were submitted to the standard protocol and then to an additional acquisition with 16 cm/min scan speed. Images acquired using with 16 cm/min scan speed were processed using the Pixon algorithm. The series were blindly assessed by three physicians and also by means of a quantitative analysis.

From the clinical study it was possible to conclude that the physicians didn't find any differences in lesion detection between raw images from standard protocol and those acquired with half the scanning time, even when not processed. Besides, image quality parameters of the image acquired using the standard protocol were similar when compared to the one acquired with 16 cm/min scan speed after processing. Thus, the results provided either by the phantom or the clinical investigation shown that, at least in cases of breast and

prostate cancer, the scanning time can be reduced by doubling the scan speed because the outcome will be analogous after processing the images.

Despite the fact that subjective analysis didn't show differences regarding diagnostic quality between raw and processed series with reduced acquisition time, it was shown that objective measurements significantly improve after processing the images, having comparable results to those achieved with the standard protocol. The same conclusion was reached in the work of Vija *et al.* dedicated for SPECT data: although noise reduction resulted in significant improvements in detectability based on quantitative measures, only a minor gain was recorder when testing with human observers. However, improving physical image quality parameters is a valuable argument to process the images.

The same results were found in a clinical investigation performed in Naestved, Denmark, by Abdiwahab Hassan (2014). Images acquired using the routine protocol (20 minutes scan duration) were compared to those acquired using a faster protocol (10 minutes scan duration) and subsequently processed using the same processing tool. Only four healthy patients were included. No quantitative parameters were computed due to the insufficient data for statistics. However, qualitative measurements revealed that no differences were found between image types, with no interference on diagnosis (84).

According to the work developed by Wesolowski *et al.* (2004), patient images with poor contrast get improved visualization after being Pixon processed. The referred investigation proven that the processing algorithm improves image contrast by reducing noise by an order of magnitude in planar scintigraphic images. During this study the observers (three specialists) preferred processed images instead of raw series in 81.5 % of the cases, with good agreement (87 %). Moreover, processed images had superior lesion detectability and reduced noise levels with no statistically significant changes in artifacts (63).

7. Direction for future work

The application of the present work was just limited to whole-body bone scintigraphy with ^{99m}Tc-HDP. Future work may include the applicability of the Pixon processing algorithm in several procedures of planar nuclear imaging using different radiopharmaceuticals.

There is also a possibility of reducing the activity dose when using the EPP software. This means that the processing algorithm could also be very useful in maintaining image quality when a minimum radioactive dosage is administrated. This was an additional goal of the investigation performed by of Vija, *et al.*, however, these results need to be further investigated, particularly in the clinical area. Still, this could be an interesting starting point for additional research, especially in paediatric imaging.

Additionally, some research could be performed in order to understand the influence of the reconstruction parameters in the imaging results. At the time of this investigation it was not possible to modify those parameters because it was not allowed by the software, being difficult to understand if the default parameters were optimal for image processing. However, the possibility of setting different parameters should be considered in the future.

8. Final remarks

Despite the fact that the results from different investigations seem to support the application of this image processing algorithm, it is important to mention that the implementation of such an instrument should depend on the goals of each department. This also means if there are enough profits to be invested, because if the software is not available yet it will cost around 9 000 €. Still, if those goals include improving patient care and the department's workflow by reducing the scanning time, this can be an extremely valuable tool.

The investigated algorithm shown to have its advantages, allowing the reduction of the acquisition time in 50 %. This is not just an important factor concerning patient care, but also as regards the department’s workflow. In this perspective, physicians and nuclear medicine technologists could have more time to perform additional examinations to the patients (such SPECT scans) when it is necessary to identify light changes in bone uptake that need further clarification, increasing the diagnostic and treatment effectiveness.

V. Conclusion

The results explained during the present work show, without a doubt, that the Pixon algorithm incorporated on the EPP software significantly improves the quality of the scintigraphic images. Besides, it was shown that the results obtained with some protocols using increased scan speed can have comparable results to those of the standard protocol.

The aim of this investigation was not just to demonstrate the improvements in the images when using different protocols, but also to investigate how much the scan speed could be increased without having losses in image quality and, of course, object detectability.

It was shown that if acquisition time was reduced in 25 %, which means applying a scan speed of 12 cm/min, and the resulting image subsequently submitted to the processing algorithm, the image quality and the detectability itself could be even better than using the standard protocol.

On the contrary, when looking to the opposite limit, which is reducing the acquisition time in 75 % using a scan speed of 20 cm/min, after processing, the images turn to be worse regarding detectability and image quality when compared with the standard protocol.

However, when the acquisition time was reduced just in 50 % (by applying a scan speed of 16 cm/min) and the image submitted to the same processing tool, image quality and detectability found to be comparable to the results obtained with the standard protocol.

At last, this means that if the aim is to reduce the scanning duration and, at the same time, to maintain the physical parameters and other factors that define the routine standard protocol, 16 cm/min is the most adequate scan speed to be used if the acquired image is meant to be processed with the investigated algorithm.

Even with the evidences provided by this study and the parallel clinical investigation, the validation of the protocol will only be performed after the deliberation of the managers of the department. This decision should also be made with an agreement of the staff, including technologists and physicians. However, after the demonstration of the achieved results in the hospital, the feedback was generally positive.

Furthermore, there is a massive interest in publishing and spreading the achieved results, complemented by further investigation if required. It was proven that the standard protocol can be modified, at least for conditions related to breast and prostate carcinomas, in those departments in which this processing software is available, or even those who intend to acquire it. These conclusions might also indicate that the existing guidelines for the whole-body bone scintigraphy may be re-evaluated in order to include this new possibility.

Bibliographic References

1. *Skeletal Complications of Malignancy.* **Coleman, Robert E.** s.l. : American Cancer Society, 1997, Cancer, Vol. 80, pp. 1588-94. Available from: http://onlinelibrary.wiley.com/doi/10.1002/(SICI)1097-0142(19971015)80:8%2B%3C1588::AID-CNCR9%3E3.0.CO;2-G/pdf.

2. **International Atomic Energy Agency (IAEA).** *Criteria for Palliation of Bone Metastases - Clinical Applications.* Nuclear Medicine Section. 2007. Available from: http://www-pub.iaea.org/MTCD/publications/PDF/te_1549_web.pdf. IAEA-TECDOC-1549.

3. *Clinical Features of Metastatic Bone Disease and Risk of Skeletal Morbidity.* **Coleman, Robert E.** s.l. : American Association for Cancer Research, 2006, Clinical Cancer Research, Vol. 12.

4. *The Science and Practice of Bone Health in Oncology: Managing Bone Loss and Metastasis in Patients With Solid Tumors.* **Lipton, Allan, et al., et al.** 2009, Journal of the National Comprehensive Cancer Network.

5. *Bone Imaging in Metastatic Breast Cancer.* **Hamaoka, Tsuyoshi, et al., et al.** s.l. : American Society of Clinical Oncology, 2004, Journal of Clinical Oncology, Vol. 22, pp. 2942-2953.

6. *Comparison of Image Enhancement Methods for the Effective Diagnosis in Successive Whole-Body Bone Scans.* **Jeong, Chang Bu, et al., et al.** 2011, Journal of Digital Imaging, Vol. 24, pp. 424-436.

7. **Krom, Aaron J., et al., et al.** Evaluation of Image Enhancement Software as a Method of Performing Half-count Scans. *Nuclear Medicine Communications.* 2012, Vol. 34, pp. 78-85.

8. *Tumor metastasis to bone.* **Virk, Mandeep S. and Lieberman, Jay R.** 2007, Arthritis Reasearch & Therapy, Vol. 9.

9. *Pathophysiology of Bone Metastases: How This Knowledge May Lead to Therapeutic Intervention.* **Lipton, Allan.** 2004, The Journal of Supportive Oncology, Vol. 2, pp. 205-220.

10. **Kini, Usha and Nandeesh, B. N.** Physiology of Bone Formation, Remodeling, and Metabolism. [book auth.] Ignac Fogelman, Gopinath Gnanasegaran and Hans Wall. *Radionuclide and Hybrid Bone Imaging.* s.l. : Springer, 2013, pp. 29-55. Available from: http://www.springer.com/cda/content/document/cda_downloaddocument/9783642023996-c1.pdf?SGWID=0-0-45-1356540-p173959977.

11. **Jacofsky, David J., Frassica, Deborah A. and Frassica, Frank J.** Metastatic Disease to Bone. *Hospital Physician.* 2004, Vol. 39, pp. 21-28.

12. **Torbert, Jesse T. and Lackman, Richard D.** Pathological Fractures. [book auth.] R. J. Pignolo, M. A. Keenan and N. M. Hebela. *Fractures in the Elderly.* s.l. : Springer, 2011, 2, pp. 43-54. Available from: https://www.google.pt/url?sa=t&rct=j&q=&esrc=s&source=web&cd=1&cad=rja&uact=8&ved=0CCYQFjAA&url=http%3A%2F%2Fwww.springer.com%2Fcda%2Fcontent%2Fdocument%2Fcda_downloaddocument%2F9781603274661-c1.pdf%3FSGWID%3D0-0-45-1061070-p173799842&ei=f.

13. *Imaging bone metastases in breast cancer: techniques and recommendations for diagnosis.* **Costelloe, Coleen M., et al., et al.** 2009, The Lancet Oncology, Vol. 10, pp. 606-614.

14. *Radiological imaging for the diagnosis of bone metastases.* **Rybak, L. D. and Rosenthal, D. I.** 2001, The Quarterly Journal of Nuclear Medicine, Vol. 45, pp. 53-64.

15. *Diagnostic imaging methods in metastatic disease.* **Milosevic, Zorica, Gajic-Dobrosavljevic, Marija and Stevanovic, Jasna.** s.l. : Institute of Oncology Sremska Kamenica, 2006. Vol. 14, pp. 73-74. Available from: http://www.onk.ns.ac.rs/archive/Vol14/PDFVol14/V14s1p73.pdf.

16. *FDG PET and PET/CT: EANM procedure guidelines for tumor PET imaging: version 1.0.* **Boellaard, Ronald, et al., et al.** s.l. : Springer, 2010, Journal of Nuclear Medicine Molecular Imaging, Vol. 37, pp. 181-200.

17. *Detection of Bone Metastases: Assessent of Integrated FDG PET/CT Imaging.* **Taira, Al V., et al., et al.** s.l. : RSNA, 2007, Radiology, Vol. 243, pp. 204-211.

18. *The Detection of Bone Metastases in Patients with High-risk Prostate Cancer: 99mTc-MDP Planar Bone Scintigraphy, Single- and Multi-Field-of-View SPECT, 18F-Fluoride PET, and 18F-Fluoride PET/CT.* **Even-Sapir, Einat, et al., et al.** 2006, Journal of Nuclear Medicine, Vol. 47, pp. 287-297.

19. *Basic science: nuclear medicine in skeletal imaging.* **Calleja, Michele, et al., et al.** s.l. : Elsevier, 2005. Current Orthopaedics. Vol. 19, pp. 34-39. Available from: http://www.sciencedirect.com/science/article/pii/S0268089005000101.

20. **Madsen, Mark T.** Nuclear Medicine Imaging Instrumentation. [book auth.] Myer Kutz. *Standard Handbook of Biomedical Engineering and Desing.* s.l. : McGraw-Hill, 2009. Available from: http://www.slideshare.net/abccrcfge28/biomedical-engineering-and-design-handbook.

21. **Lee, Jae Sung.** Basic Nuclear Physics and Instrumentation. [book auth.] Edmund E. Kim, et al., et al. *Handbook of Nuclear Medicine and Molecular Imaging.* s.l. : World Scientific, 2012, 1, pp. 3-19. Available from: http://www.worldscientific.com/doi/suppl/10.1142/8245/suppl_file/8245_chap01.pdf.

22. **Mettler, Fred A. and Guiberteau, Milton J.** *Essentials of Nuclear Medicine Imaging.* 5th. s.l. : Elsevier, 2006.

23. **Bushberg, Jerrold T., et al., et al.** *The Essential Physics of Medical Imaging.* 3rd. s.l. : Lippincot Williams & Wilkins, 2012.

24. **Maher, Kieran.** *Basic Physics of Nuclear Medicine.* s.l. : Libronomia Company, 2006. Available from: https://archive.org/details/BasicPhysicsOfNuclearMedicinek.MaherWikibooks2006.pdf.

25. **Ziegler, Sibylle I. and Dahlbom, Magnus.** Instrumentation and Data Acquisition. [book auth.] A. L. Baert and K. Sartor. *Diagnostic Nuclear Medicine.* 2nd. s.l. : Springer, 2006, 16, pp. 275-290. Available from: http://mariorad.com/books/General%20radiology/036%20Diagnostic%20Nuclear%20Medicine%20-%20A.L.%20Baert,%20Christiaan%20Schiepers.pdf.

26. **Christian, Paul E. and Waterstram-Rich, Kristen M.** *Nuclear Medicine and PET/CT.* 6th. s.l. : Elsevier, 2007.

27. **Health Protection Agency for the Administration of Radioactive Substances Advisory Committee.** A Review of the Supply of Molybdenum-99, the Impact of Recent Shortages and the Implications for Nuclear Medicine Services in the UK. 2010.

28. **Pedroso de Lima, J. J.** *Nuclear Medicine Physics.* s.l. : Coimbra University Press, 2011.

29. **Cherry, Simon R., Sorenson, James A. and Phelps, Michael E.** *Physics in Nuclear Medicine.* 4th. s.l. : Elsevier, 2012.

30. **Prekeges, Jennifer.** *Nuclear Medicine Instrumentation.* s.l. : Jones and Bartlett, 2012.

31. **Schiepers, Christiaan.** Skeletal Scintigraphy. [book auth.] A. L. Baert and K. Sartor. *Diagnostic Nuclear Medicine.* s.l. : Springer, 2006. Available from: http://mariorad.com/books/General%20radiology/036%20Diagnostic%20Nuclear%20Medicine%20-%20A.L.%20Baert,%20Christiaan%20Schiepers.pdf.

32. **Society of Nuclear Medicine.** *Procedure Guideline for Bone Scinitgraphy.* 2003. pp. 205-209, Guidelines. Available from: http://snmmi.files.cms-plus.com/docs/pg_ch34_0403.pdf. v. 3.0.

33. **European Association of Nuclear Medicine (EANM).** *Bone scintigraphy: procedure guidelines for tumour imaging.* 2003. Guidelines. Available from: http://www.eanm.org/publications/guidelines/gl_onco_bone.pdf.

34. Introduction to Medical Imaging. [book auth.] Hodder Arnold. *Imaging for Students.* s.l. : David A Lisle, 2012, 1. Available from: http://cw.tandf.co.uk/imagingforstudents/sample-material/Chapter-1-Introduction-to-Medical-Imaging.pdf.

35. **Britton, K. E.** Nuclear Medicine Imaging in Bone Metastases. *Cancer Imaging.* 2002, Vol. 2, pp. 84-86.

36. **Brenner, Arnold I., et al., et al.** *The Bone Scan.* s.l. : Elsevier, 2012. pp. 11-26, Seminars in Nuclear Medicine. Available from: http://www.seminarsinnuclearmedicine.com/article/S0001-2998(11)00096-1/pdf.

37. **American College of Radiology (ACR) and Society for Pediatric Radiology (SPR).** *ACR - SPR Practice Parameter for the Performance of Skeletal Scintigraphy (Bone Scan).* 2014. Practice Parameter. Available from: http://www.acr.org/~/media/839771405B9A43F7AF2D2A9982D81083.pdf.

38. *Patterns, Variants, Artifacs, and Pitfalls in Conventional Radionuclide Bone Imaging and SPECT/CT.* **Gnanasegaran, Gopinath, et al., et al.** s.l. : Elsevier, 2009. Seminars in Nuclear Medicine. pp. 380-393. Available from: http://www.seminarsinnuclearmedicine.com/article/S0001-2998(09)00057-9/pdf.

39. **Tapiovaara, M.** *Relationships between physical measurements and user evaluation of image quality in medical radiology - A review.* Finland : s.n., 2006. Available from: http://www.stuk.fi/julkaisut/stuk-a/stuk-a219.pdf. STUK-A219.

40. **Smith, Steven W.** *The Scientist and Engineer's Guide to Digital Signal Processing.* 1997. Available from: http://www.analog.com/en/content/scientist_engineers_guide/fca.html.

41. **Puetter, R. C., Gosnell, T. R. and Yahil, Amos.** Digital Image Reconstruction: Debluring and Denoising. *Annual Review of Astronomy and Astrophysics.* 2005, Vol. 43, pp. 139-194.

42. **Thie, Joseph A.** *Nuclear Medicine Imaging: An Encyclopedic Dictionary.* s.l. : Springer, 2012.

43. *A Review of Image Denoising Algorithms, with a new one.* **Buades, A., Coll, B. and Morel, J. M.** 2005, SIAM Journal on Multiscale Modeling and Simulation 4, Vol. 2, pp. 490-530.

44. **Maintz, Twan.** *Digital and Medical Image Processing.* 2005.

45. **International Atomic Energy Agency (IAEA).** *Quantitative Nuclear Medicine Imaging: Concepts, Requirements and Methods.* Vienna : s.n., 2014. IAEA Human Health Reports. Available from: http://www-pub.iaea.org/MTCD/Publications/PDF/Pub1605_web.pdf. No. 9.

46. **Abdi, Hervé.** Coefficient of Variation. [book auth.] Neil Salkind. *Encyclopedia of Research Design.* s.l. : SAGE, 2010. Available from: https://www.utdallas.edu/~herve/abdi-cv2010-pretty.pdf.

47. **Pratt, William K., [ed.].** *Digital Image Processing.* 4th. s.l. : Wiley, 2007. Available from: http://onlinelibrary.wiley.com/doi/10.1002/9780470097434.fmatter/pdf.

48. **Motwani, Mukesh C., Gadiya, Mukesh C. and Motwani, Rakhi C.** *Survey of Image Denoising Techniques.* s.l. : Proceedings of GSPx, 2004. Available from: http://citeseerx.ist.psu.edu/viewdoc/download;jsessionid=04E04D1B127AD2D33B80158FFAC9961E?doi=10.1.1.107.1823&rep=rep1&type=pdf.

49. *An Intelligent Approach to Image Denoising.* **Saba, Tanzila, Rehman, Amjad and Sulong, Ghazali.** s.l. : JATIT & LLS, 2010, Journal of Theoretical and Applied Information Technology.

50. **Zaidi, Habib.** *Quantitative Analysis in Nuclear Medicine Imaging.* s.l. : Springer, 2006.

51. Pixon Applications in Medical Imaging. *Pixon Revealing Reality.* [Online] Pixon, LLC, 2004. [Cited: 26 June 2014.] http://pixon.com/solutions.html.

52. **Vija, A. Hans, et al., et al.** *Statistically Based, Spatially Adaptive Noise Reduction of Planar Nuclear Studies.* 2005. Available from: https://www.google.pt/url?sa=t&rct=j&q=&esrc=s&source=web&cd=2&cad=rja&uact=8&ved=0CCkQFjAB&url=http%3A%2F%2Fwww.researchgate.net%2Fpublication%2F228363512_Statistically_based_spatially_adaptive_noise_reduction_of_planar_nuclear_studies%2F.

53. **Puetter, Richard C. and Yahil, Amos.** *The Pixon Method of Image Reconstruction.* Cornell University Library. 1999. Available from: http://www.adass.org/adass/proceedings/adass98/reprints/puetterrc.pdf.

54. **International Atomic Energy Agency (IAEA).** Assessment of image quality with phantoms. *IAEA | Human Health Campus.* [Online] 2010-2013. [Cited: 07 10 2014.] http://nucleus.iaea.org/HHW/MedicalPhysics/DiagnosticRadiology/ImageQualityAssessment/Assessmentofimagequalitywithphantoms/index.html.

55. **Data Spectrum Corporation.** Product Line: SPECT QC Phantoms. [Online] 17 03 2007. [Cited: 10 10 2014.] http://www.spect.com/products-spect.html.

56. **National Electrical Manufacturers Association.** *Performance Measurements of Positron Emission Tomographs.* 2001. NEMA Standards Publication NU 2. Available from: http://dea.unsj.edu.ar/mednuclear/PET-NEMA-NU2-2001.pdf.

57. *PET/CT Performance Evaluation Techniques and Quality Assurance.* **Kemp, Brad.** s.l. : The American Association of Physics in Medicine. Department of Radiology, Mayo Clinic. Available from: http://www.aapm.org/meetings/amos2/pdf/29-7921-47101-434.pdf.

58. *Reduction in Radiation Dose in Mercaptoacetyltriglycerine Renography with Enhanced Planar Processing.* **Hsiao, Edward M., et al., et al.** s.l. : RSNA, 2011, Radiology, Vol. 261, pp. 907-915.

59. **Lorimer, Lisa, et al., et al.** Improvement in DMSA Imaging Using Adaptive Noise Reduction: an ROC Analysis. *Nuclear Medicine Communications.* 2012.

60. The Pixon Method. *Pixon Revealing Reality.* [Online] Pixon LLC, 12 September 2002. [Cited: 28 May 2014.] http://www.pixon.com/brochure.html.

61. **Hassanpour, Hamid, Yousefian, Hadi and Zehtabian, Amin.** Pixon-Based Image Segmentation. [ed.] Pei-Gee Ho. *Image Segmentation.* s.l. : InTech, 2011, 26. Available from: http://cdn.intechopen.com/pdfs-wm/15396.pdf.

62. *A novel pixon-representation for image segmentation based on Markov random field.* **Lin, Lei, et al., et al.** s.l. : Elsevier, 2008, Image and Vision Computing, Vol. 26, pp. 1507-1514.

63. *Improved lesion detection from spatially adaptive, minimally complex, Pixon reconstruction of planar scintigraphic images.* **Wesolowski, Carl A., et al., et al.** s.l. : Elsevier, 2005, Computerized Medical Imaging and Graphics, Vol. 29, pp. 65-81.

64. **Lin, Robert P., Dennis, Brian R. and Benz, Arnold O.** *The Reuven Ramaty High-Energy Solar Spectroscopic Imager - Mission Description and Early Results.* s.l. : Kluwer Academic Publishers, 2003.

65. *Pixon-based Miltiresolution Image Reconstruction for Yohkoh's Hard X-ray Telescope.* **Metcalf, Thomas R., et al., et al.** s.l. : The American Astronomical Society, 1996, The Astrophysical Journal, Vol. 466, pp. 585-594.

66. **Gregory, Phil.** *Bayesian Logical Data Analysis for the Physical Sciences.* Cambridge : Cambridge University Press, 2005.

67. *The Information Content of Redshift and Velocity Surveys.* **Yahil, A.** New York : s.n., 1995. XXXth Moriond Meeting "Clustering in the Universe". Available from: http://www.pixon.com/publications/Yahil_96_Moriond.pdf.

68. RESSI - Reuven Ramaty High Energy Solar Spectroscopic Imager. *HESSI Pixon Tutorial.* [Online] NASA, 16 March 2004. [Cited: 26 June 2014.] http://hesperia.gsfc.nasa.gov/rhessidatacenter/imaging/pixon/pixon_tutorial.html.

69. **Espinosa, J M Rodriguez, Herrero, A and Sanchez, F.** *Instrumentation for Large Telescopes.* Cambrigde : Cambridge University Press, 1997.

70. *Pixon-Based Multiresolution Image Reconstruction and the Quantification of Picture Information Content.* **Puetter, R. C.** 1995, The International Journal of Image Systems and Technology. Available from: http://www.pixon.com/publications/Puetter_95_MaxEnt.pdf.

71. **Heidbreder, Glenn R.** *Maximum Entropy and Bayesian Methods.* California : Kluwer Academic Publishers, 1993.

72. **Puetter, Richard and Yahil, Amos.** *Accelerated Signal Encoding and Reconstruction Using Pixon Methods. US 6,353,688 B1* United States of America, 05 March 2002. Available from: http://www.google.com.ar/patents/US6353688.

73. *Quantification of diphosphonate uptake based on conventional bone scanning.* **Brenner, Winfried , et al., et al.** 10, s.l. : Springer-Verlag, 1997, European Journal of Nuclear Medicine, Vol. 24, pp. 1284–1290.

74. **Lyra, Maria, Ploussi, Agapi and Georgantzoglou, Antonios.** MATLAB as a Tool in Nuclear Medicine Image Processing. [book auth.] Clara M. Ionescu. *MATLAB - A Ubiquitous Tool for the Practical Engineer.* s.l. : InTech, 2011, 23. Available from: http://cdn.intechopen.com/pdfs-wm/21962.pdf.

75. *The Kappa Statistic in Reliability Studies: Use, Interpretation, and Sample Size Requirements.* **Sim, Julius and Wright, Chris C.** 2005, Journal of the American Physical Therapy Association, Vol. 85, pp. 257-268. Available from: http://ptjournal.apta.org/content/85/3/257.full.pdf+html. 3.

76. *The measurement of observer agreement for categorical data.* **Landis, J. R. and Koch, G. G.** 1977, Biometrics, Vol. 33, pp. 159-79.

77. Nonparametric Tests. [book auth.] David S. Moore. *The Basic Practice of Statistics.* 4th. s.l. : W. H. Freeman and Company, 2006, 26. Available from: http://www2.uncp.edu/home/marson/syllabi/36006thChapter26_NonparametricTests.pdf.

78. *Planar Processing.* **Snoijs, Corné.** Breda : s.n., 2013. Amphia Hospital, Breda - The Netherlands. Courtesy of the author.

79. **Rahawadan, Jerry.** *Enhanced Planar Processing.* UMC St Radboud Nijmegen : s.n., 2013. Investigation project for Fontys Paramedische Hogeschool.

80. **Medina-Gálvez, Noelia and Pedraz, Teresa.** Nuclear Medicine in Musculoskeletal Disorders: Clinical Approach. [ed.] Ali Gholamrezanezhad. *12 Chapters on Nuclear Medicine.* s.l. : InTech, 2011, 5. Available from: http://cdn.intechopen.com/pdfs-wm/25569.pdf.

81. Skeletal Scintigraphy. [book auth.] Harvey A. Ziessman, et al., et al. *Nuclear Medicine: The Requisites.* 4th. s.l. : Elsevier, 2014, 7. Available from: https://www.inkling.com/read/nuclear-medicine-ziessman-4th/chapter-7/bone-scan.

82. Nuclear medicine: Planar scintigraphy, SPECT and PET/CT. [book auth.] Nadine Barrie Smith and Andrew Webb. *Introduction to Medical Imaging.* s.l. : Cambridge University Press, 2010, pp. 89-139. Available from: https://www.google.pt/url?sa=t&rct=j&q=&esrc=s&source=web&cd=1&cad=rja&uact=8&ved=0CCU

QFjAA&url=http%3A%2F%2Ffreerecipesforyou.com%2Fraja%2Fto%2520Raja%2F2014%2F09_September%2F20140913%2FIntroduction%2520to%2520Medical%2520Imaging%2520%259.

83. *Preprocessing of SPECT Projection Data: Benefits and Pitfalls.* **Vija, A. Hans, Yahil, Amos and Hawman, Eric G.** 2005. IEEE Nuclear Science Symposium Conference Record. Available from: http://citeseerx.ist.psu.edu/viewdoc/download;jsessionid=E1BAF9AB2E96FCC69F8C63BD701E7996?doi=10.1.1.140.8048&rep=rep1&type=pdf.

84. **Hasssan, Abdiwahab.** *Implementering af Pixon-software til knogleskintigrafi, som reducerer undersøgelsestiden uden at forringe billedkvaliteten.* University College Sjaelland Naestved. Naestved : s.n., 2014. Investigation project for Bachelor Degree. Available from: https://www.ucviden.dk/student-portal/files/22169546/bachelorprojekt.pdf.

Appendix I

Scoring form used for the subjective assessment.

Spheres	Diameter	1	2	3	4	5	6	7	8	9	10	11	12	13	14	15	16
1	37																
2	28																
3	22																
4	17																
5	13																
6	10																

Spheres	Diameter	17	18	19	20	21	22	23	24	25	26	27	28	29	30	31	32
1	37																
2	28																
3	22																
4	17																
5	13																
6	10																

Spheres	Diameter	33	34	35	36	37	38	39	40	41	42	43	44	45	46	47	48
1	37																
2	28																
3	22																
4	17																
5	13																
6	10																

✔ Visible

✖ Not Visible

Appendix II

Activity Ratio	Speed / mm	Raw Images												Processed Images											
		Observer 1						Observer 2						Observer 1						Observer 2					
		37	28	22	17	13	10	37	28	22	17	13	10	37	28	22	17	13	10	37	28	22	17	13	10
4:1	8	✓	–	–	–	–	–	✓	–	–	–	–	–	✓	✓	–	–	–	–	✓	✓	✓	–	–	–
	12	–	–	–	–	–	–	✓	–	–	–	–	–	–	–	–	–	–	–	✓	–	✓	–	–	–
	16	–	–	–	–	–	–	✓	–	–	–	–	–	–	–	–	–	–	–	✓	✓	–	–	–	–
	20	–	–	–	–	–	–	–	–	–	–	–	–	–	–	–	–	–	–	✓	–	–	–	–	–
8:1	8	✓	✓	✓	–	–	–	✓	✓	✓	✓	–	–	✓	✓	✓	–	–	–	✓	✓	✓	✓	–	–
	12	✓	✓	–	–	–	–	✓	✓	–	✓	–	–	✓	✓	–	–	–	–	✓	✓	✓	✓	–	–
	16	✓	✓	✓	–	–	–	✓	✓	✓	–	✓	–	✓	✓	✓	–	–	–	✓	✓	✓	✓	–	–
	20	✓	–	–	–	–	–	✓	✓	✓	–	–	–	✓	✓	–	–	–	–	✓	✓	✓	–	–	–
17:1	8	✓	✓	✓	✓	✓	–	✓	✓	✓	✓	✓	–	✓	✓	✓	✓	✓	–	✓	✓	✓	✓	✓	–
	12	✓	✓	✓	✓	–	–	✓	✓	✓	✓	✓	–	✓	✓	✓	✓	–	–	✓	✓	✓	✓	✓	–
	16	✓	✓	✓	✓	–	–	✓	✓	✓	✓	✓	–	✓	✓	✓	✓	–	–	✓	✓	✓	✓	✓	–
	20	✓	✓	✓	–	–	–	✓	✓	✓	✓	✓	–	✓	✓	✓	✓	–	–	✓	✓	✓	✓	✓	–
22:1	8	✓	✓	✓	✓	✓	✓	✓	✓	✓	✓	✓	✓	✓	✓	✓	✓	✓	✓	✓	✓	✓	✓	✓	✓
	12	✓	✓	✓	✓	✓	✓	✓	✓	✓	✓	✓	✓	✓	✓	✓	✓	✓	✓	✓	✓	✓	✓	✓	✓
	16	✓	✓	✓	✓	✓	–	✓	✓	✓	✓	✓	–	✓	✓	✓	✓	✓	–	✓	✓	✓	✓	✓	–
	20	✓	✓	✓	✓	✓	–	✓	✓	✓	✓	✓	–	✓	✓	✓	✓	✓	–	✓	✓	✓	✓	✓	✓
32:1	8	✓	✓	✓	✓	✓	–	✓	✓	✓	✓	✓	✓	✓	✓	✓	✓	✓	–	✓	✓	✓	✓	✓	✓
	12	✓	✓	✓	✓	✓	–	✓	✓	✓	✓	✓	–	✓	✓	✓	✓	✓	–	✓	✓	✓	✓	✓	✓
	16	✓	✓	✓	✓	–	–	✓	✓	✓	✓	✓	–	✓	✓	✓	✓	✓	–	✓	✓	✓	✓	–	–
	20	✓	✓	✓	✓	–	–	✓	✓	✓	✓	✓	✓	✓	✓	✓	✓	–	–	✓	✓	✓	✓	✓	✓
71:1	8	✓	✓	✓	✓	✓	✓	✓	✓	✓	✓	✓	✓	✓	✓	✓	✓	✓	✓	✓	✓	✓	✓	✓	✓
	12	✓	✓	✓	✓	✓	✓	✓	✓	✓	✓	✓	✓	✓	✓	✓	✓	✓	✓	✓	✓	✓	✓	✓	✓
	16	✓	✓	✓	✓	✓	–	✓	✓	✓	✓	✓	✓	✓	✓	✓	✓	✓	–	✓	✓	✓	✓	✓	✓
	20	✓	✓	✓	✓	✓	✓	✓	✓	✓	✓	✓	✓	✓	✓	✓	✓	✓	✓	✓	✓	✓	✓	✓	✓

This page intentionally left blank